Electronic Supplementary Material (ESI) for Chemical Science.

Electronic Supporting Information

Mechanochemical reactivity inhibited, prohibited and reversed by liquid additives: Examples from crystal-form screens

Mihails Arhangelskis, Dejan-Krešimir Bučar, Simone Bordignon, Michele R. Chierotti, Samuel A. Stratford, Dario Voinovich, William Jones and Dritan Hasa

Table of contents

1. Materials

Vinpoxetine (**vin**) (99%) was purchased from *Linnea SA Riazzino-Locarno*, CH. Anthranylic acid (**ana**) (≥98%), caffeine (**caf**) (*ReagentPlus*®), 2,3-difluorobenzoic acid (**23diFBA**) (98%), ibuprofen (≥98%), nicotinamide (≥99.5%), oxalix acid (H_2**oxa**) (99%), paracetamol (**par**) (98%), theophylline (**thp**) (99%) and all solvents (≥99%) were obtained from *Sigma Aldrich*, Ltd. (Gillingham, UK), while 2,6-difluorobenzoic acid (**26diFBA**) (97%) was purchased from *Maybridge*.

2. Mechanochemical experiments

2.1 Experimental Section

2.1.1 Milling Experiments involving vin and H_2oxa

Neat- and liquid-assisted grinding (LAG) experiments were performed using a *Retsch MM200* mixer mill. In a typical experiment, 200 mg of equimolar physical mixture of **vin** and H_2**oxa** (approximately 159 mg of **vin** and 41 mg of H_2**oxa**) were added to a 15 mL steel milling jar containing two milling balls (7 mm diameter). Different amounts of liquid additives (η value in the 0.05-0.30 µL mg^{-1} range) were also added prior to miling. The mixture was subsequently milled for 60 min at a frequency of 25 Hz. Snap-closed milling jars (*FormTech Scientific*) were used to minimise liquid evaporation.

In the case of the interconversion experiments, amorphous (H**vin**$^+$)·(H**oxa**$^-$) was prepared by neat grinding of a 1:1 molar mixture of **vin** and H_2**oxa** for 60 minutes at 25 Hz, while the (H**vin**$^+$)·(H**oxa**$^-$) Forms I and II were prepared by LAG using ethyl acetate and hexane as liquid additives (η=0.30 µL mg^{-1}), respectively. The purity of the preformed products was verified by PXRD. Approximately 150 mg of preformed (H**vin**$^+$)·(H**oxa**$^-$) (either as crystalline Form I, Form II, or amorphous salt) were separately treated for other 60 min at 25 Hz under four different conditions: (i) neat grinding, (ii) LAG with dimethyl sulfoxide, nitromethane and 2-pyrrolidone (η=0.15 µL mg^{-1}), (iii) LAG using ethyl acetate (η=0.15 µL mg^{-1}) and LAG using hexane (η=0.30 µL mg^{-1}). The final products were characterised using PXRD.

In a typical *ex situ* experiment, 200 mg of an equimolar physical mixture of **vin** and H_2**oxa** (approximately 159 mg of **vin** and 41 mg of H_2**oxa**), together with a specific liquid (in the η range of 0.05−0.30 µL mg^{-1}) were processed for either 20, 40 or 60 min.

2.1.2 Milling experiments involving theophylline and fluorobenzoic acids

The mechanochemical cocrystal syntheses were attempted by LAG using either a *Retsch MM200* or a *FormTech Scientific FTS1000* mill. In a typical milling experiment, 200 mg of a physical mixture of equimolar amounts of thp and a FBA were added to a 15 mL stainless steel grinding jar, along with 50 µL of nitromethane (η = 0.25 µL mg^{-1}) and two 7 mm stainless steel milling balls. The mixer mill was operated at 30 Hz for 30 min. The obtained solids were subsequently analysed by powder X-ray diffraction.

2.1.3 Powder X-ray diffraction analyses

Unless indicated otherwise, the mechanochemically prepared solids were characterised by powder X-ray diffraction (PXRD) using a *Panalytical X'Pert Pro* diffractometer with Ni-filtered CuK_α radiation at a wavelength of 1.5418 Å equipped with an RTMS X'celerator detector. For each experiment,

approximately 20-25 mg of mechanochemical product was gently pressed on a glass slide to give a flat surface. The data were collected in the 3−40° 2θ range using a step size of 0.0334° and a scan speed of 0.142° s^{-1}.

2.2 Results

2.2.1 PXRD Results of LAG experiments performed at different η values

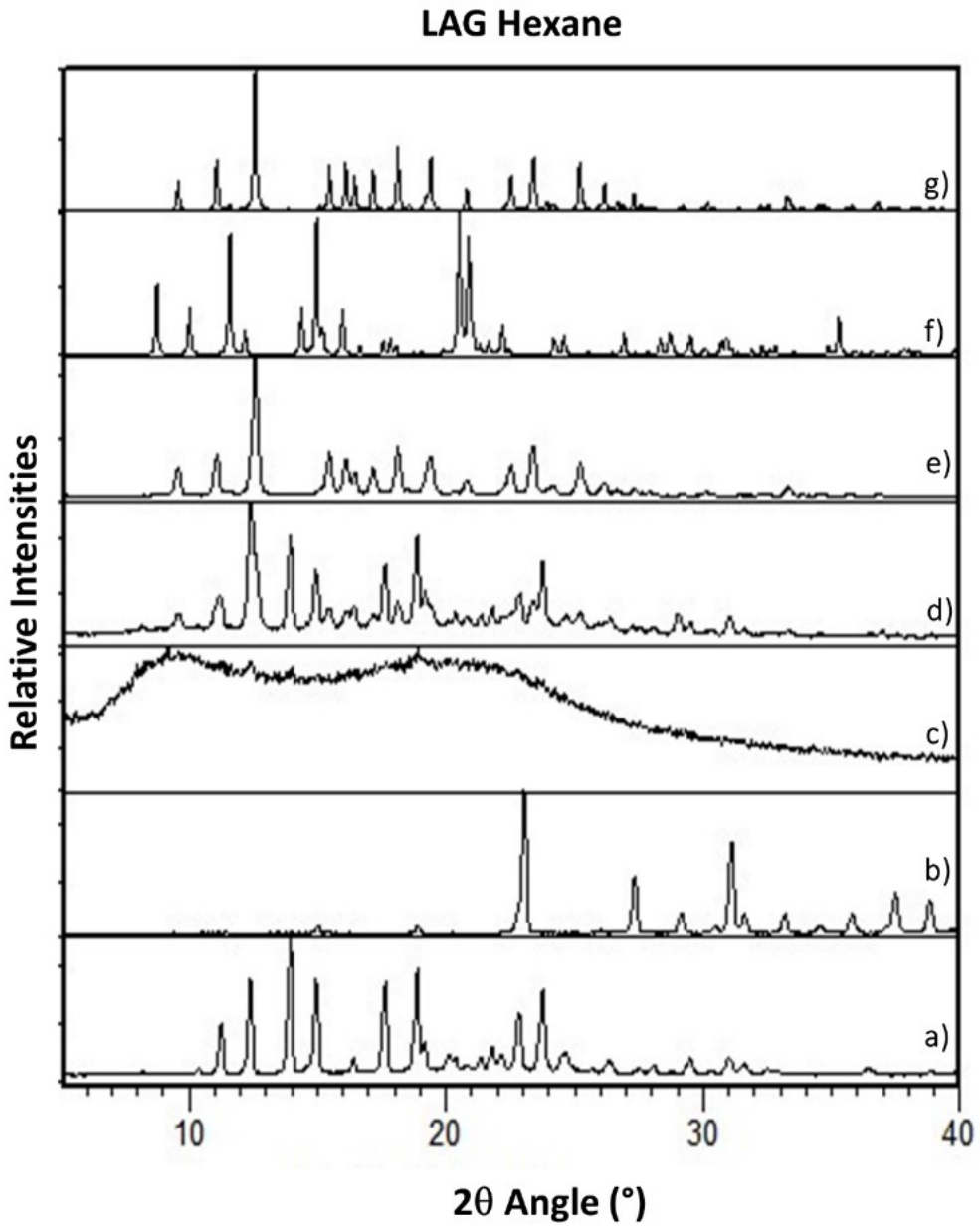

Figure S1. PXRD patterns of: (a) pure **vin**, (b) pure H_2**oxa**, (c), (d) and (e) the solid obtained through LAG of **vin** and H_2**oxa** using hexane as liquid additive at η values of 0.05 µL mg^{-1}, 0.15 µL mg^{-1} and 0.30 µL mg^{-1}, respectively, (f) calculated pattern of Form II, (g) calculated pattern of Form I.

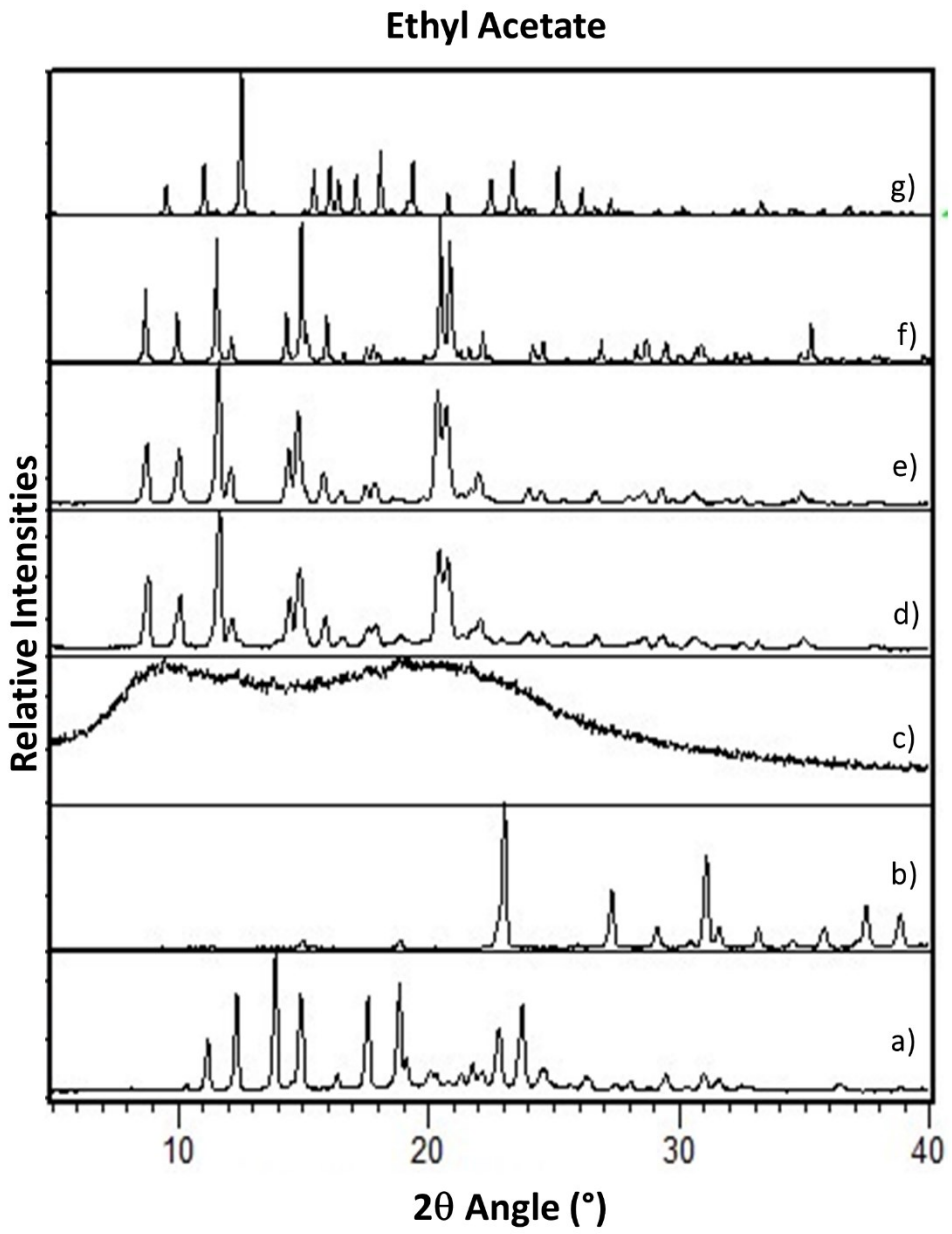

Figure S2. PXRD patterns of: (a) pure **vin**, (b) pure H_2**oxa**, (c), (d) and (e) the solid obtained through LAG of **vin** and H_2**oxa** using ethyl acetate as liquid additive at η values of 0.05 µL mg^{-1}, 0.15 µL mg^{-1} and 0.30 µL mg^{-1}, respectively, (f) calculated pattern of Form II, (g) calculated pattern of Form I.

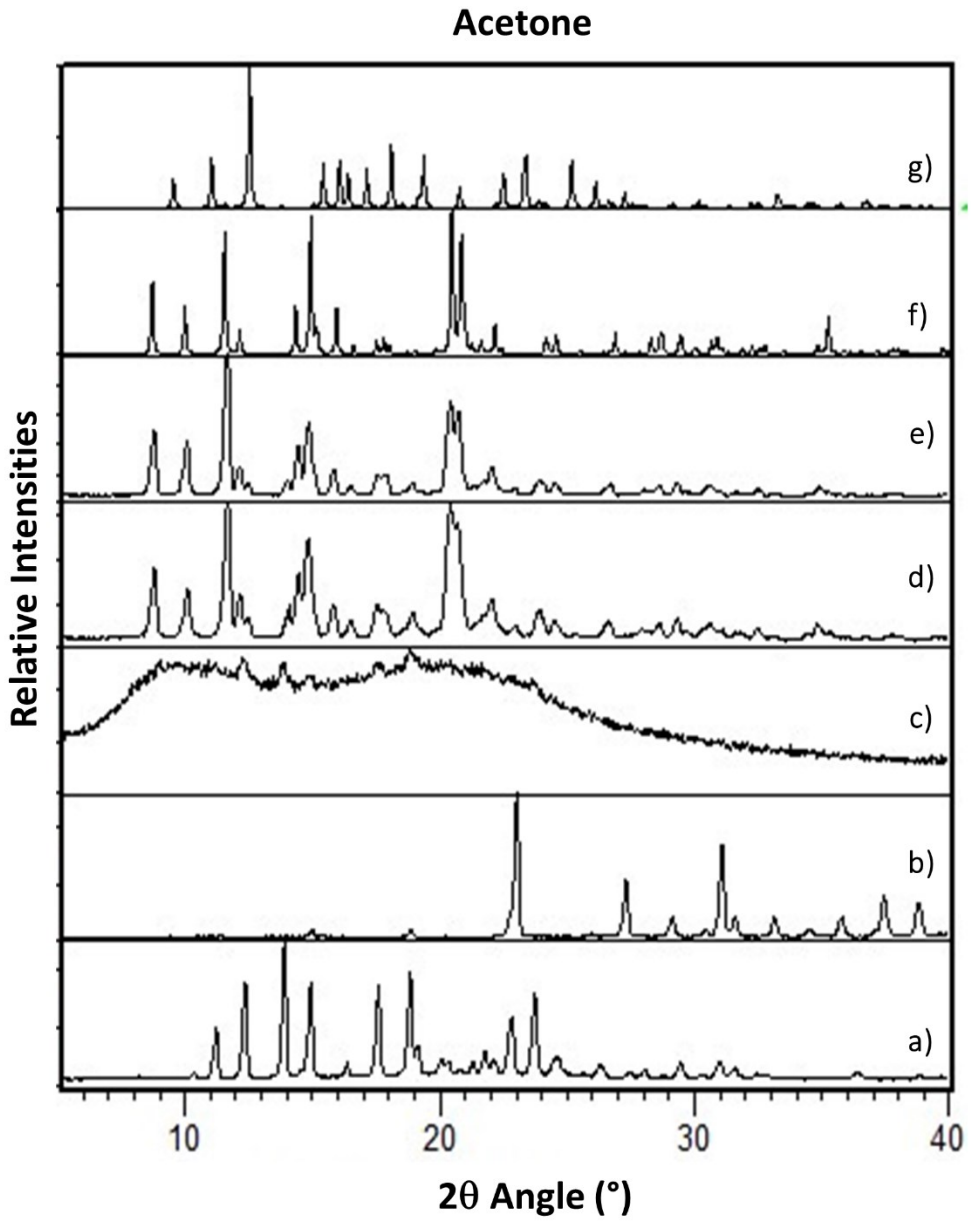

Figure S3. PXRD patterns of: (a) pure **vin**, (b) pure H_2**oxa**, (c), (d) and (e) the solid obtained through LAG of **vin** and H_2**oxa** using acetone as liquid additive at η values of 0.05 µL mg^{-1}, 0.15 µL mg^{-1} and 0.30 µL mg^{-1}, respectively, (f) calculated pattern of Form II, (g) calculated pattern of Form I.

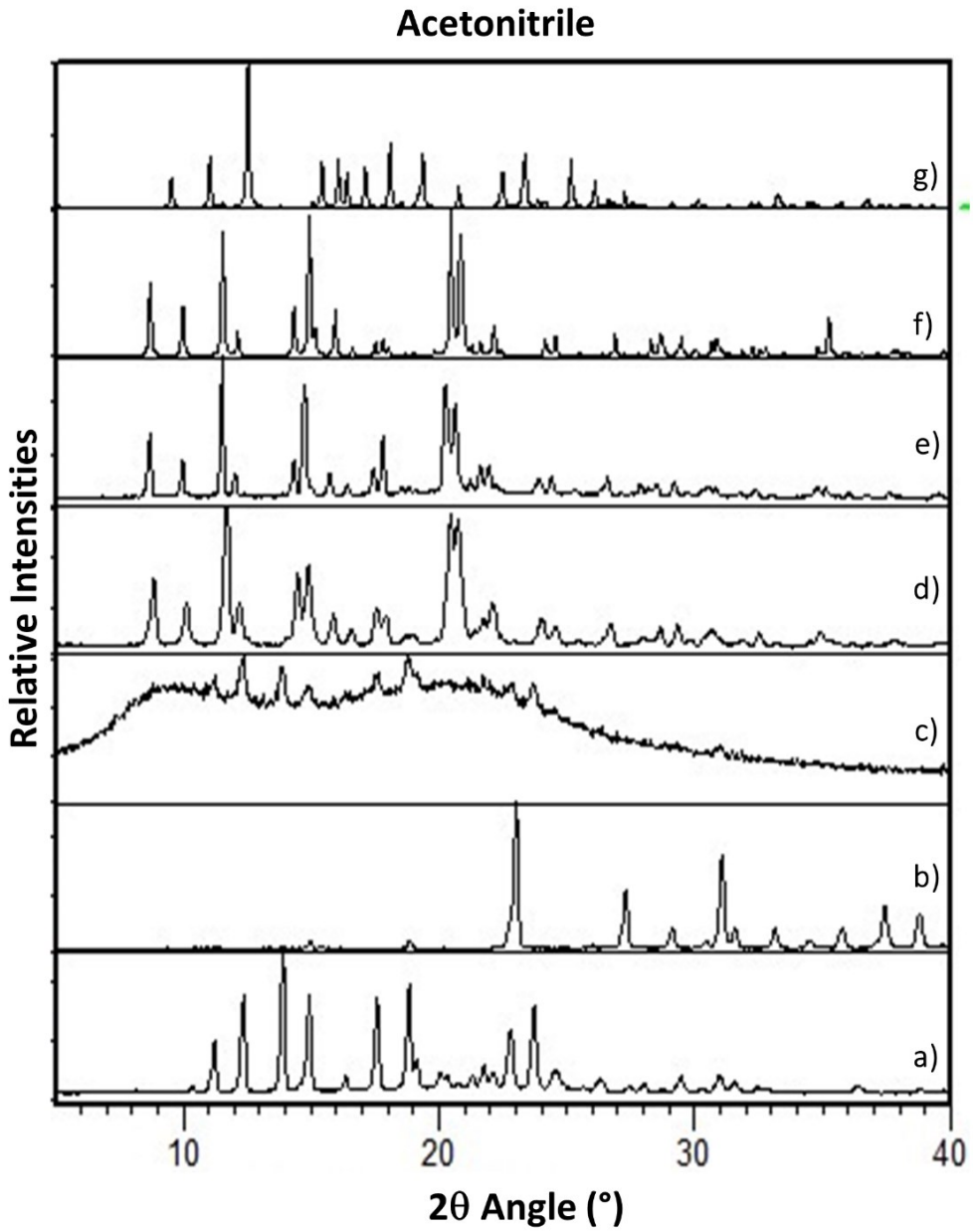

Figure S4. PXRD patterns of: (a) pure **vin**, (b) pure H_2**oxa**, (c), (d) and (e) the solid obtained through LAG of **vin** and H_2**oxa** using acetonitrile as liquid additive at η values of 0.05 µL mg^{-1}, 0.15 µL mg^{-1} and 0.30 µL mg^{-1}, respectively, (f) calculated pattern of Form II, (g) calculated pattern of Form I.

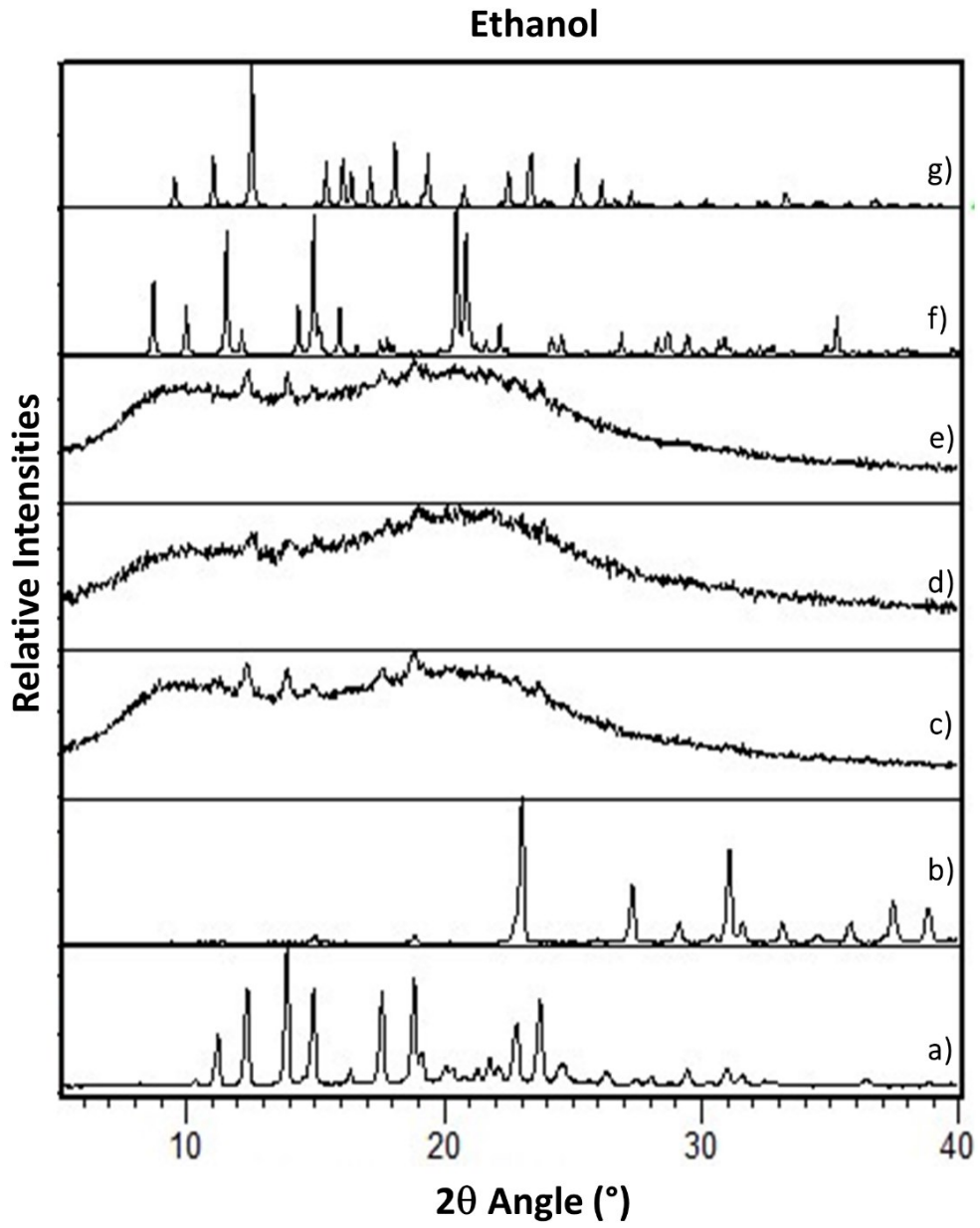

Figure S5. PXRD patterns of: (a) pure vin, (b) pure H_2**oxa**, (c), (d) and (e) the solid obtained through LAG of **vin** and H_2**oxa** using ethanol as liquid additive at η values of 0.05 µL mg^{-1}, 0.15 µL mg^{-1} and 0.30 µL mg^{-1}, respectively, (f) calculated pattern of Form II, (g) calculated pattern of Form I.

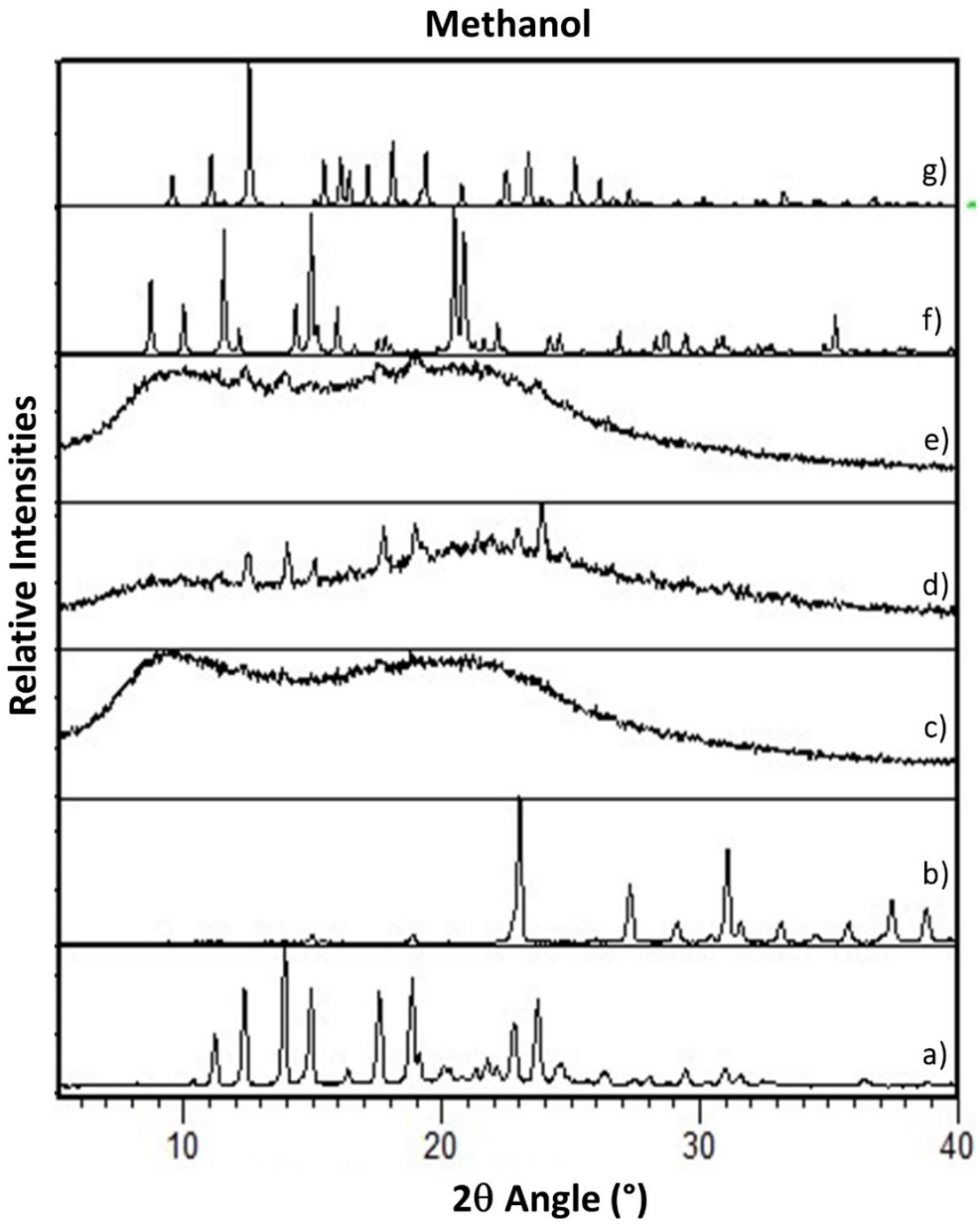

Figure S6. PXRD patterns of: (a) pure **vin**, (b) pure H_2**oxa**, (c), (d) and (e) the solid obtained through LAG of **vin** and H_2**oxa** using methanol as liquid additive at η values of 0.05 µL mg^{-1}, 0.15 µL mg^{-1} and 0.30 µL mg^{-1}, respectively, (f) calculated pattern of Form II, (g) calculated pattern of Form I.

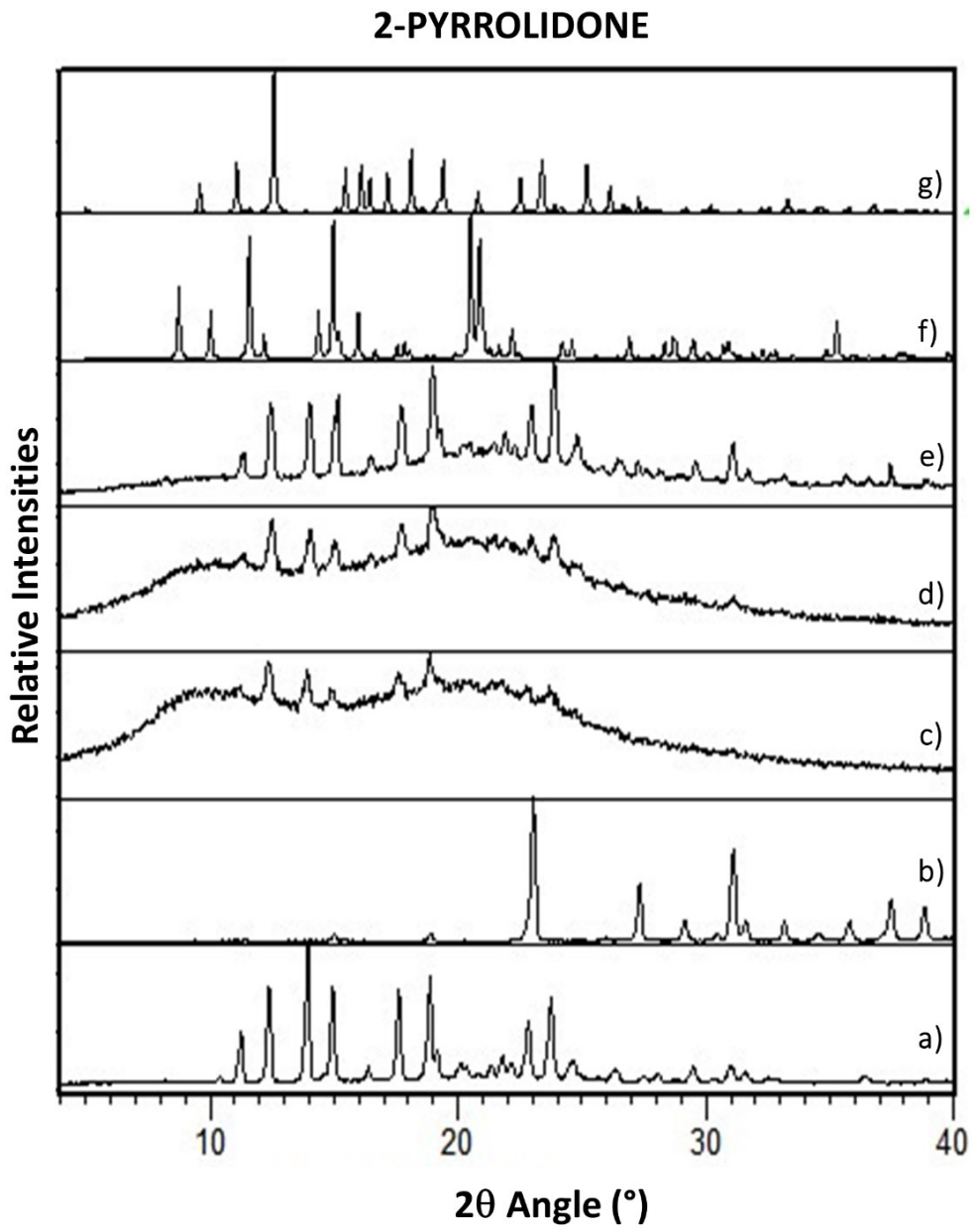

Figure S7. PXRD patterns of: (a) pure **vin**, (b) pure H_2**oxa**, (c), (d) and (e) the solid obtained through LAG of **vin** and H_2**oxa** using 2-pyrrolidone as liquid additive at η values of 0.05 µL mg^{-1}, 0.15 µL mg^{-1} and 0.30 µL mg^{-1}, respectively, (f) calculated pattern Form II, (g) calculated pattern of Form I.

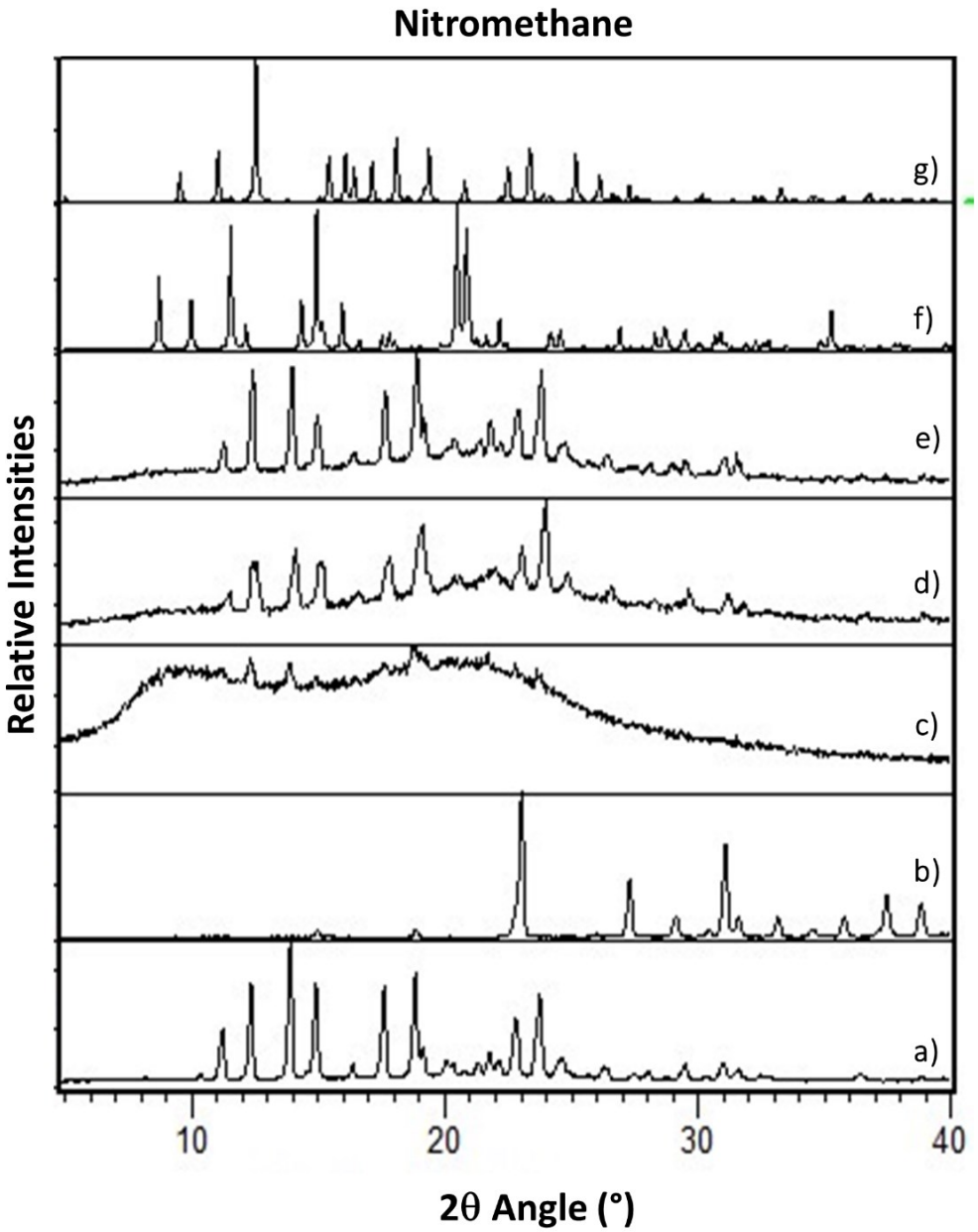

Figure S8. PXRD patterns of: (a) pure vin, (b) pure H_2**oxa**, (c), (d) and (e) the solid obtained through LAG of **vin** and H_2**oxa** using nitromethane as liquid additive at η values of 0.05 µL mg^{-1}, 0.15 µL mg^{-1} and 0.30 µL mg^{-1}, respectively, (f) calculated pattern of Form II, (g) calculated pattern of Form I.

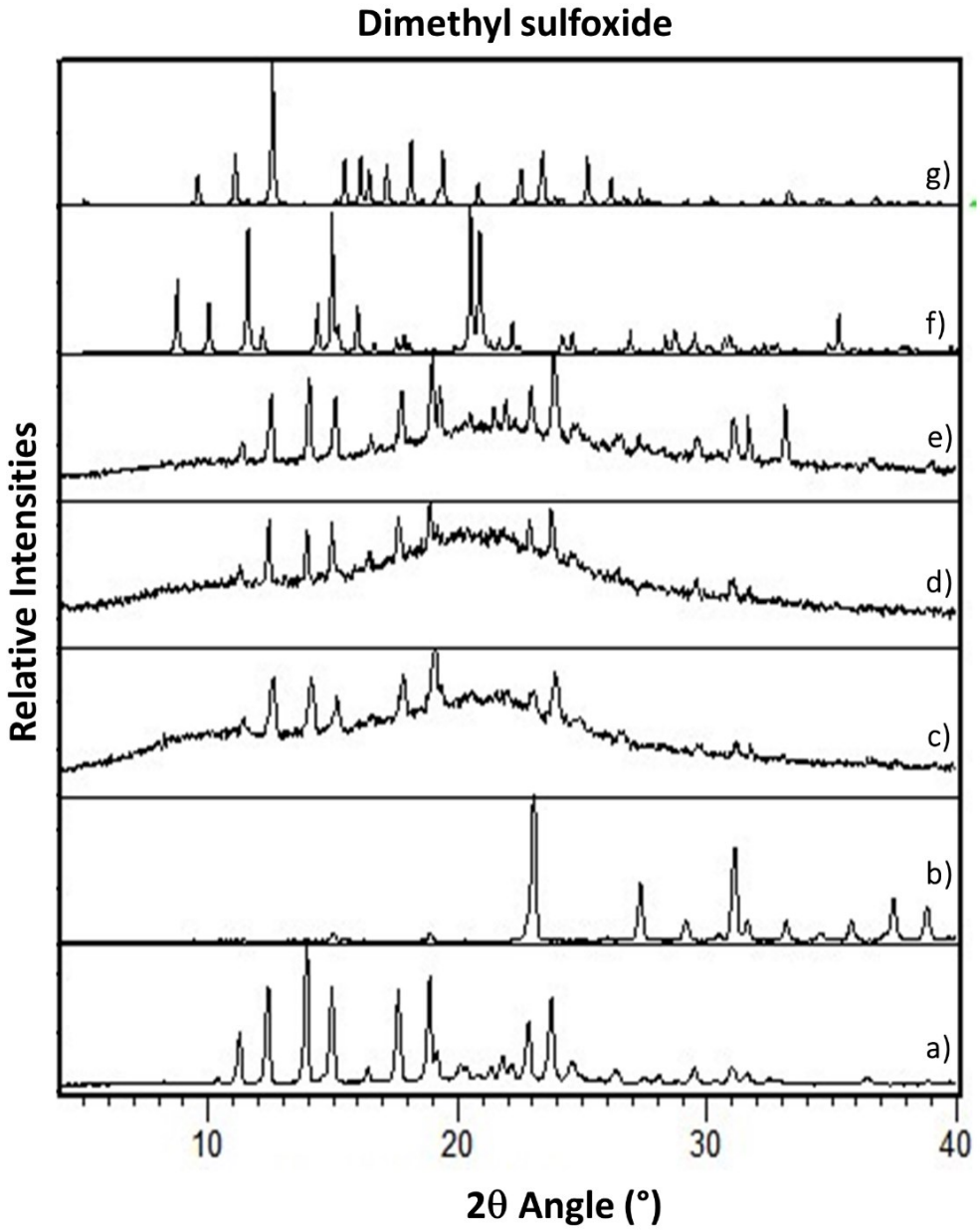

Figure S9. PXRD patterns of: (a) pure **vin**, (b) pure H_2**oxa**, (c), (d) and (e) the solid obtained through LAG of **vin** and H_2**oxa** using dimethyl sulfoxide as liquid additive at η values of 0.05 µL mg^{-1}, 0.15 µL mg^{-1} and 0.30 µL mg^{-1}, respectively, (f) calculated pattern of Form II, (g) calculated pattern of Form I.

2.2.2 Interconversion experiments

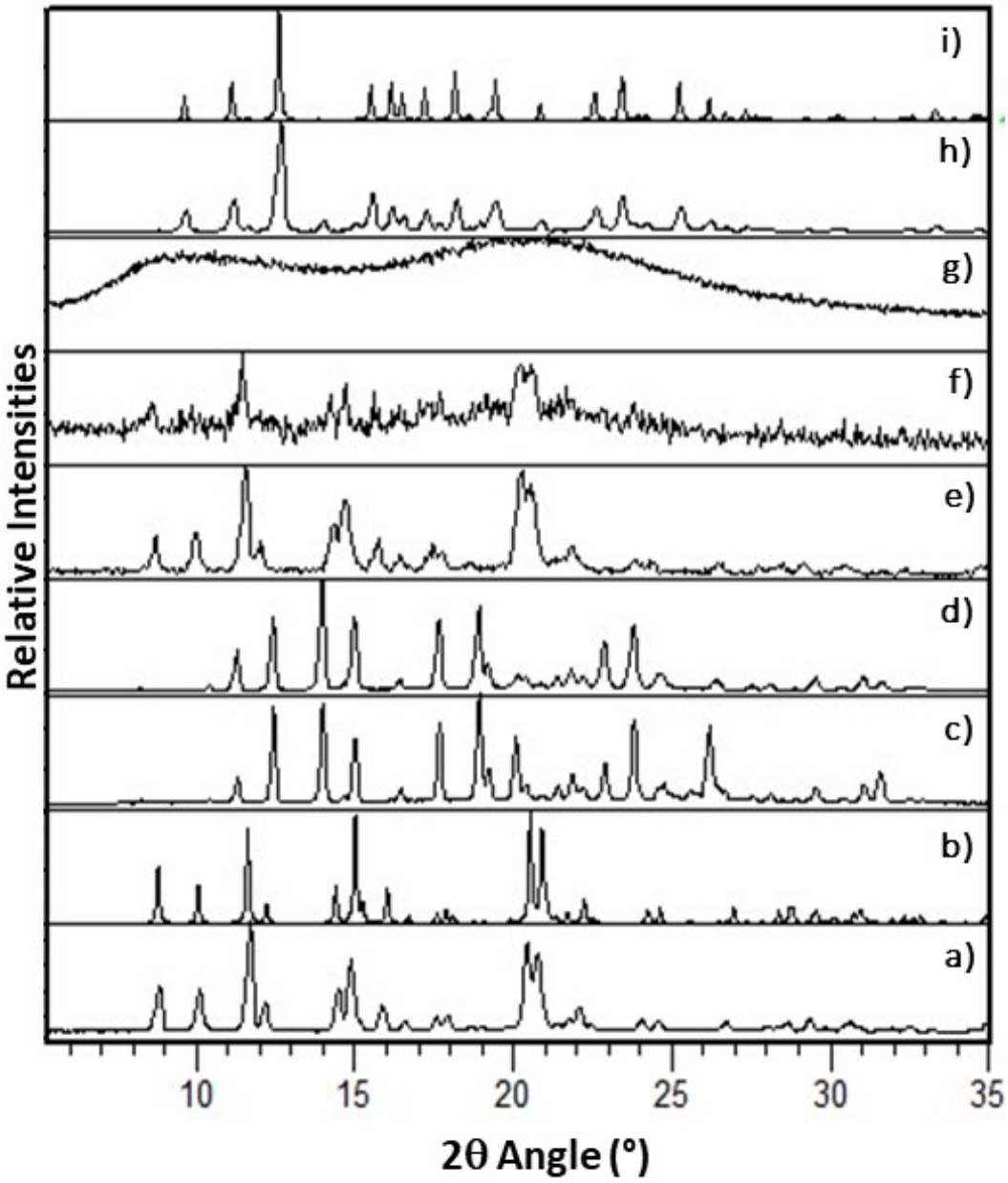

Figure S10. PXRD patterns of: (a) Form II prepared by LAG with ethyl acetate (η=0.30 µL mg^{-1}), (b) calculated Form II, (c), (d) pure **vin**, (e), (f) solid product obtained by LAG (η=0.15 µL mg^{-1}) of Form II in the presence of nitromethane, 2-pyrrolidone, respectively, (g) solid product obtained by neat grinding of Form II, (g) solid product obtained after LAG Form II with hexane (η=0.30 µL mg^{-1}) and (h) calculated pattern of Form I.

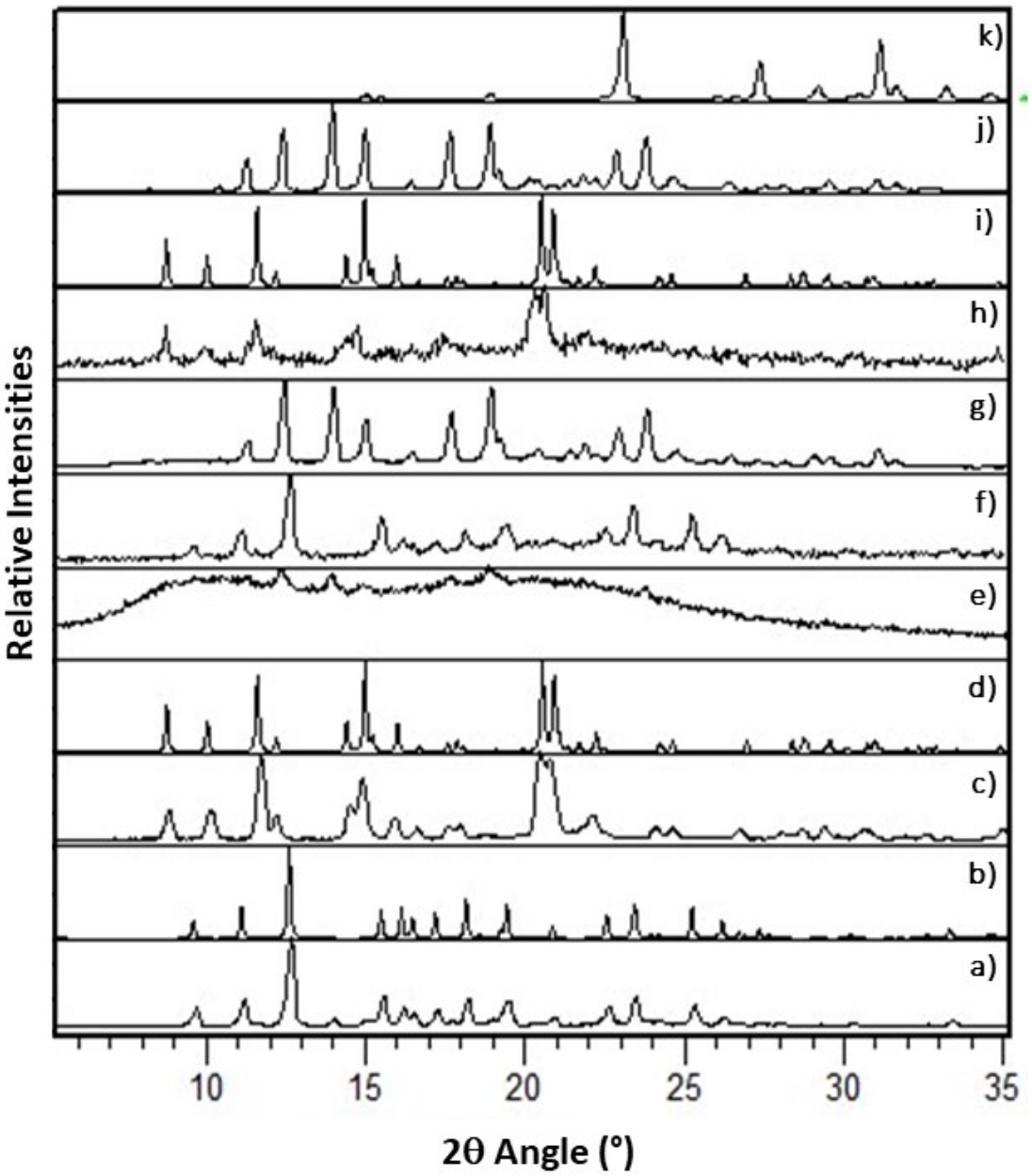

Figure S11. PXRD patterns of: (a) Form I prepared by LAG with hexane (η=0.30 μL mg^{-1}), (b) calculated Form I, (c) solid product obtained by LAG of Form I in the presence of ethyl acetate (η=0.15 μL mg^{-1}), (d) calculated Form I, (e) solid product obtained by neat grinding of Form I, (f), (g), (h) solid product obtained by LAG (η=0.30 μL mg^{-1}) of Form I in the presence of 2-pyrrolidone, dimethyl sulfoxide and nitromethane, respectively, (i) calculated Form II (j) pure **vin** and (k) pure H_2**oxa**.

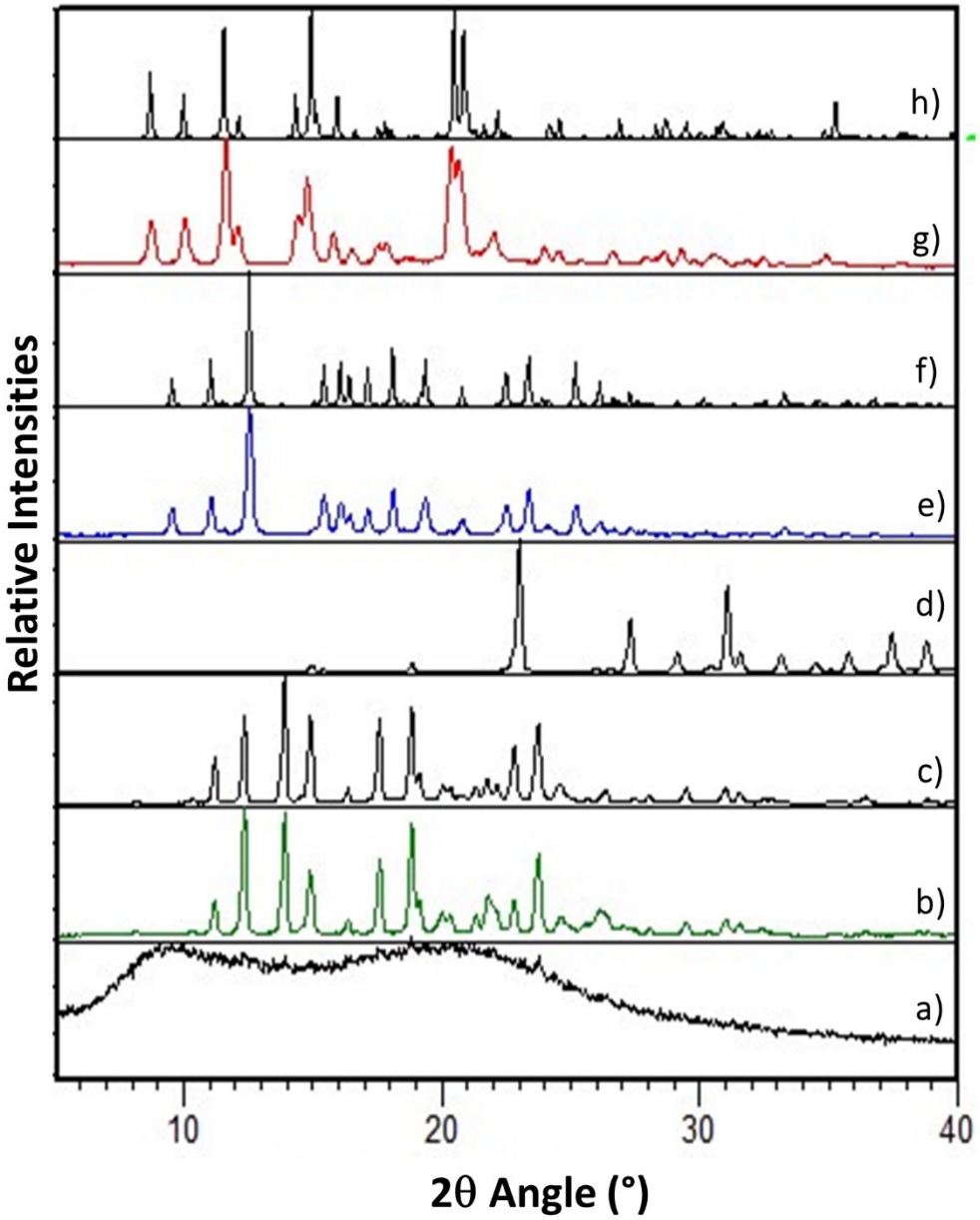

Figure S12. PXRD patterns of: (a) amorphous (H**vin**$^{+}$)·(H**oxa**$^{-}$) prepared by neat grinding, (b) product obtained through LAG of amorphous **vin**:**oxa** in the presence of dimethyl sulfoxide (η=0.15 µL mg^{-1}), (c) pure **vin**, (d) pure H_2**oxa**, (e) product of LAG of amorphous (H**vin**$^{+}$)·(H**oxa**$^{-}$) with hexane (η=0.30 µL mg^{-1}), (f) calculated Form I, (g) product of LAG of amorphous (H**vin**$^{+}$)·(H**oxa**$^{-}$) with ethyl acetate (η=0.15 µL mg^{-1}) and (h) calculated pattern of Form II.

2.2.3 Effects of milling time

To investigate the effect of milling time on the mechanochemical formation of (H**vin**$^+$)·(H**oxa**$^-$), **vin** and H_2**oxa** were milled for 20, 40 and 60 min in neat or LAG conditions with ethyl acetate, hexane and methanol. The results, shown in Figures S13-S22, suggest the following:

1) A progressive loss of crystallinity with increasing milling times in cases where **vin** and H_2**oxa** were milled under neat or LAG conditions with an inhibitor liquid (*e.g.* methanol).
2) The formation of Form I appears to be more dependent on the η value than Form II.
3) The formation of (H**vin**$^+$)·(H**oxa**$^-$) was not observed after 20 or 40 min of milling ethyl acetate and hexane at η=0.05 µL mg^{-1}, thus implying that the mechanochemical formation of crystalline (H**vin**$^+$)·(H**oxa**$^-$) dependent of the amount of (catalytic) liquid used.

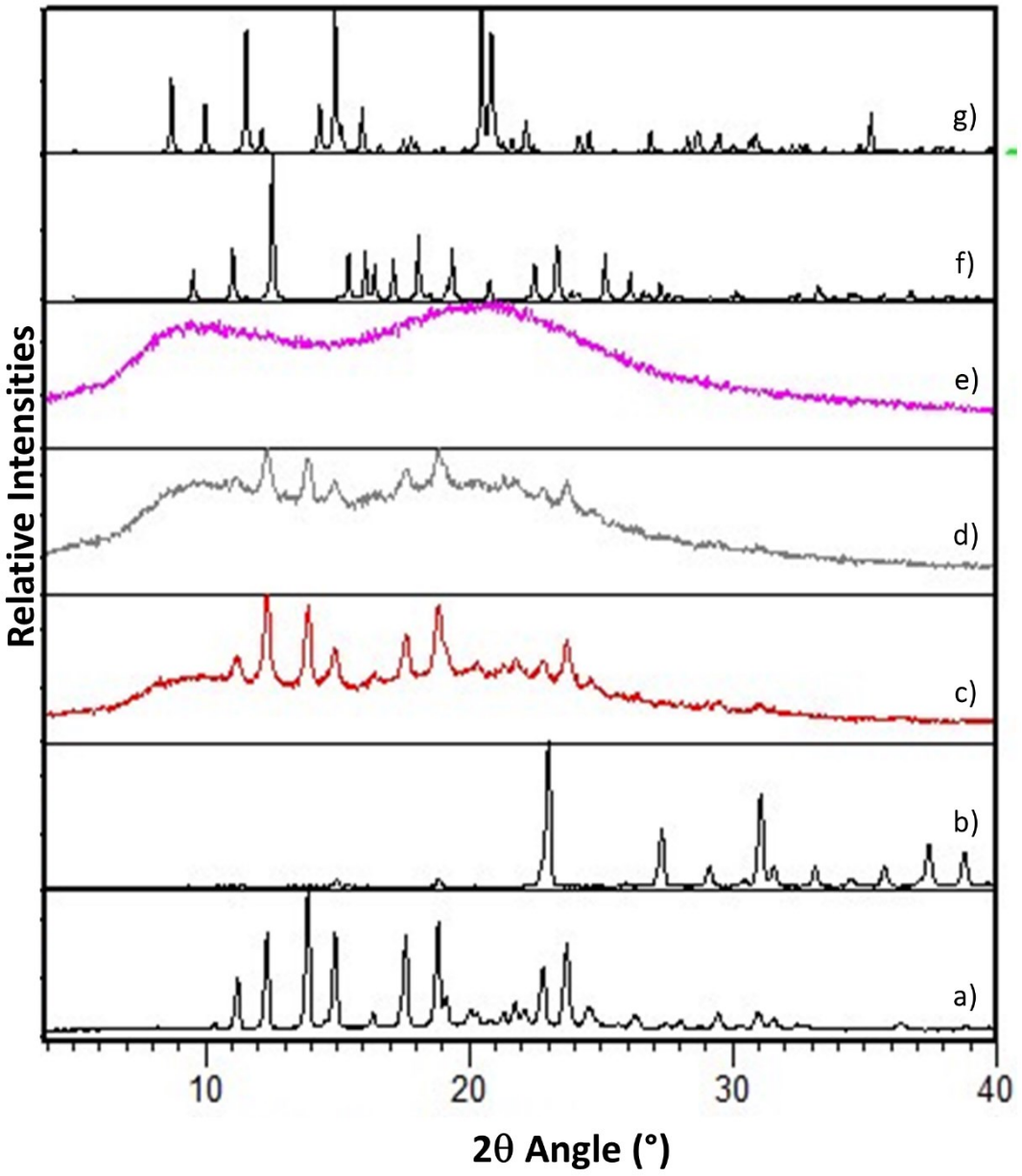

Figure S13. PXRD patterns of: (a) pure **vin**, (b) pure H_2**oxa**, (c), (d), (e) solids obtained through neat grinding of **vin** and H_2**oxa** for 20, 40 and 60 minutes respectively, (f) calculated pattern of Form I, (g) calculated pattern of Form II.

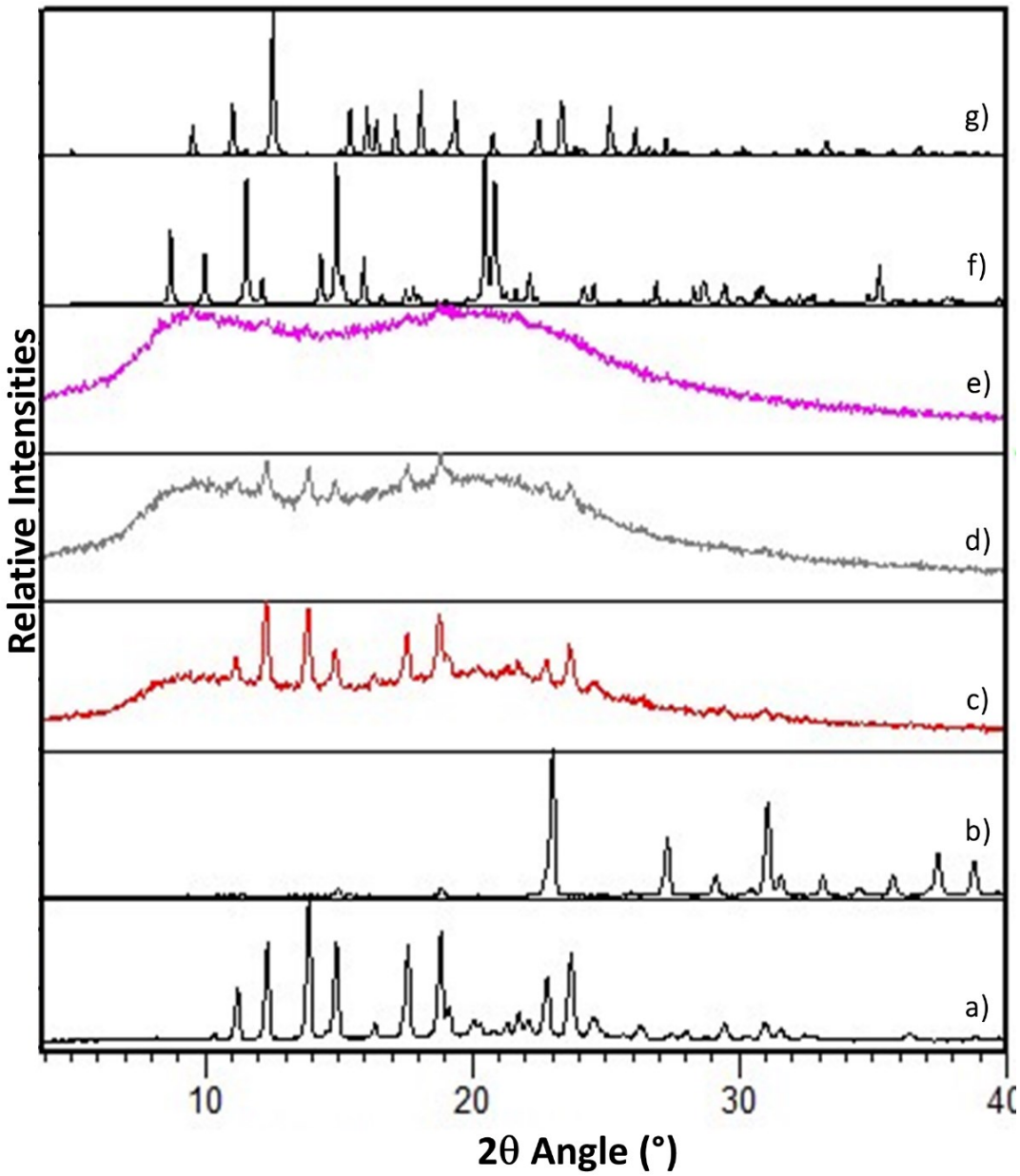

Figure S14. PXRD patterns of: (a) pure **vin**, (b) pure H_2**oxa**, (c), (d), (e) solids obtained through LAG of **vin** and H_2**oxa** in the presence of ethyl acetate (η=0.05 μL mg^{-1}) for 20, 40 and 60 minutes respectively, (f) calculated pattern of Form II, (g) calculated pattern of Form I.

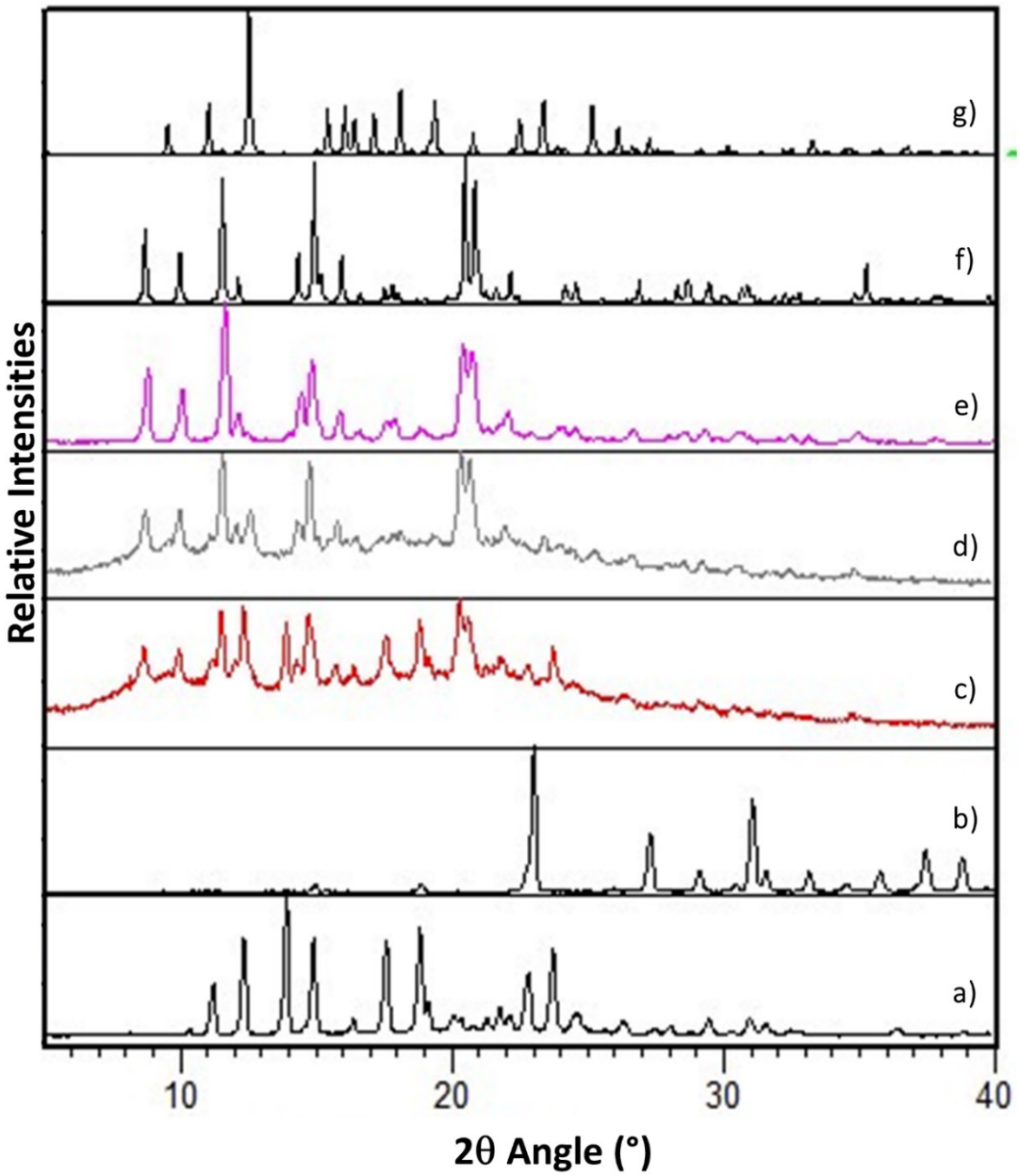

Figure S15. PXRD patterns of: (a) pure **vin**, (b) pure H_2**oxa**, (c), (d), (e) solids obtained through LAG of **vin** and H_2**oxa** in the presence of ethyl acetate (η=0.15 μL mg^{-1}) for 20, 40 and 60 minutes respectively, (f) calculated pattern of Form II, (g) calculated pattern of Form I.

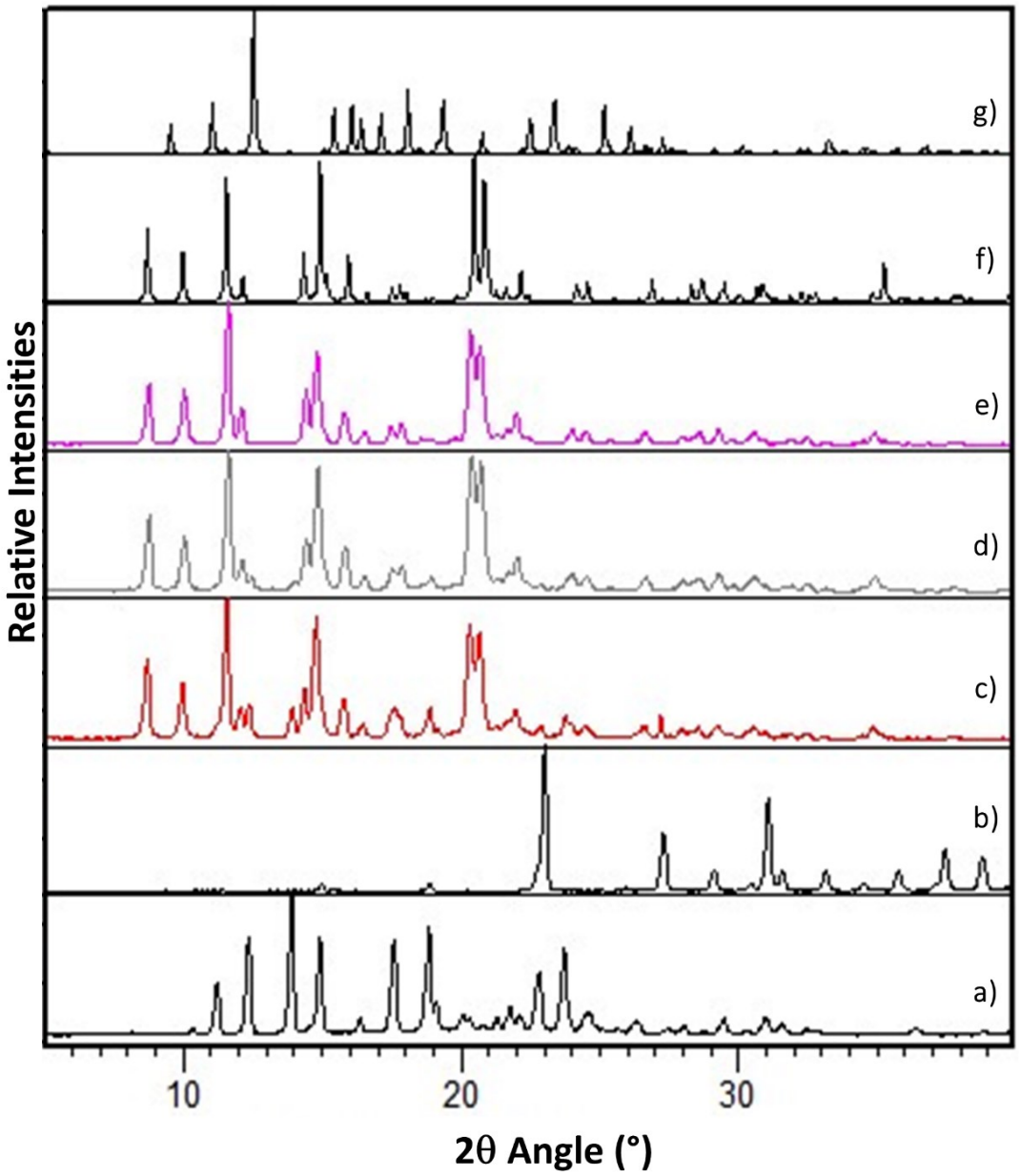

Figure S16. PXRD patterns of: (a) pure **vin**, (b) pure H_2**oxa**, (c), (d), (e) solids obtained through LAG of **vin** and H_2**oxa** in the presence of ethyl acetate (η=0.30 μL mg^{-1}) for 20, 40 and 60 minutes respectively, (f) calculated pattern of Form II, (g) calculated pattern of Form I.

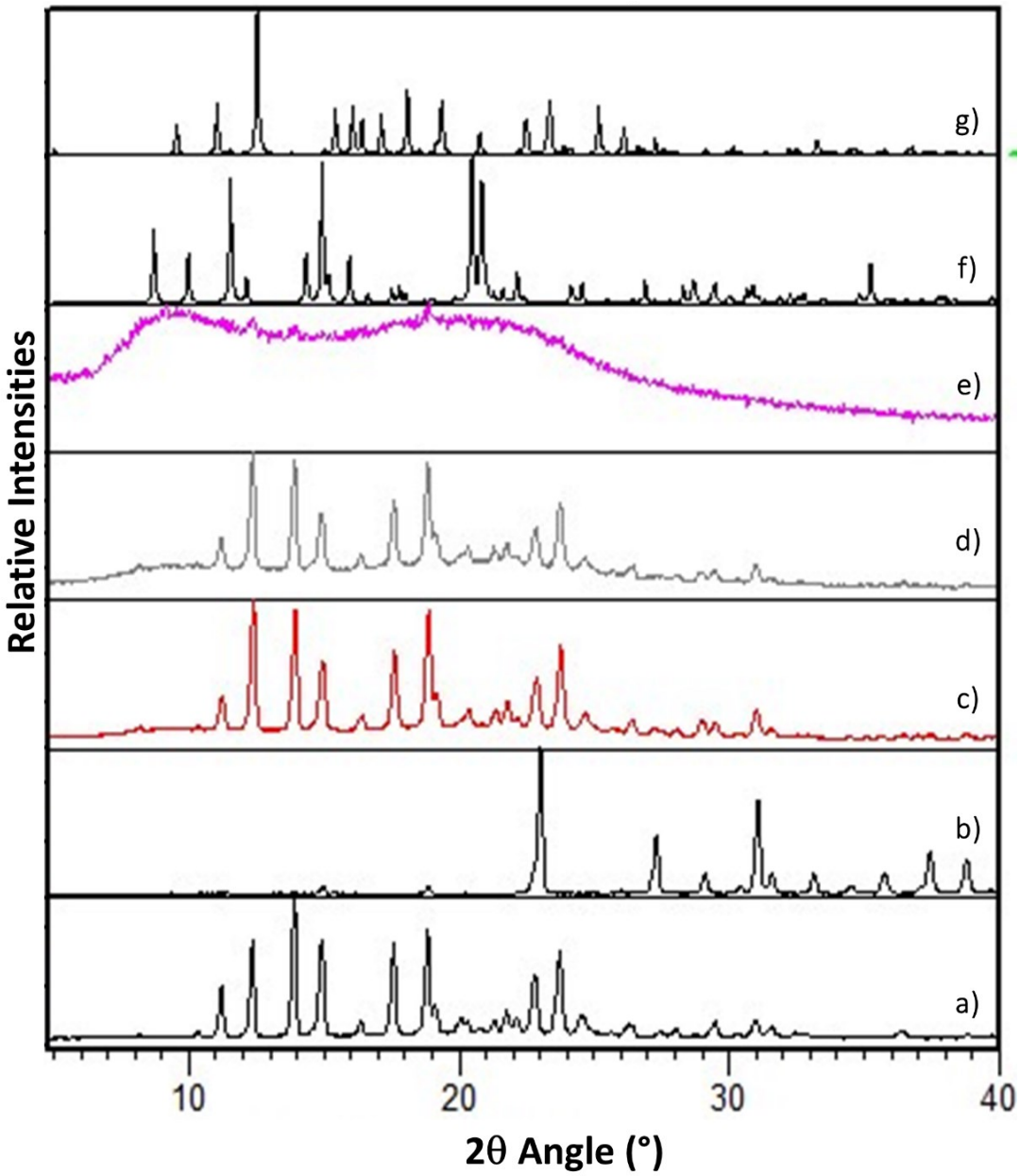

Figure S17. PXRD patterns of: (a) pure **vin**, (b) pure H_2**oxa**, (c), (d), (e) solids obtained through LAG of **vin** and H_2**oxa** in the presence of hexane (η=0.05 μL mg^{-1}) for 20, 40 and 60 minutes respectively, (f) calculated pattern of Form II, (g) calculated pattern of Form I.

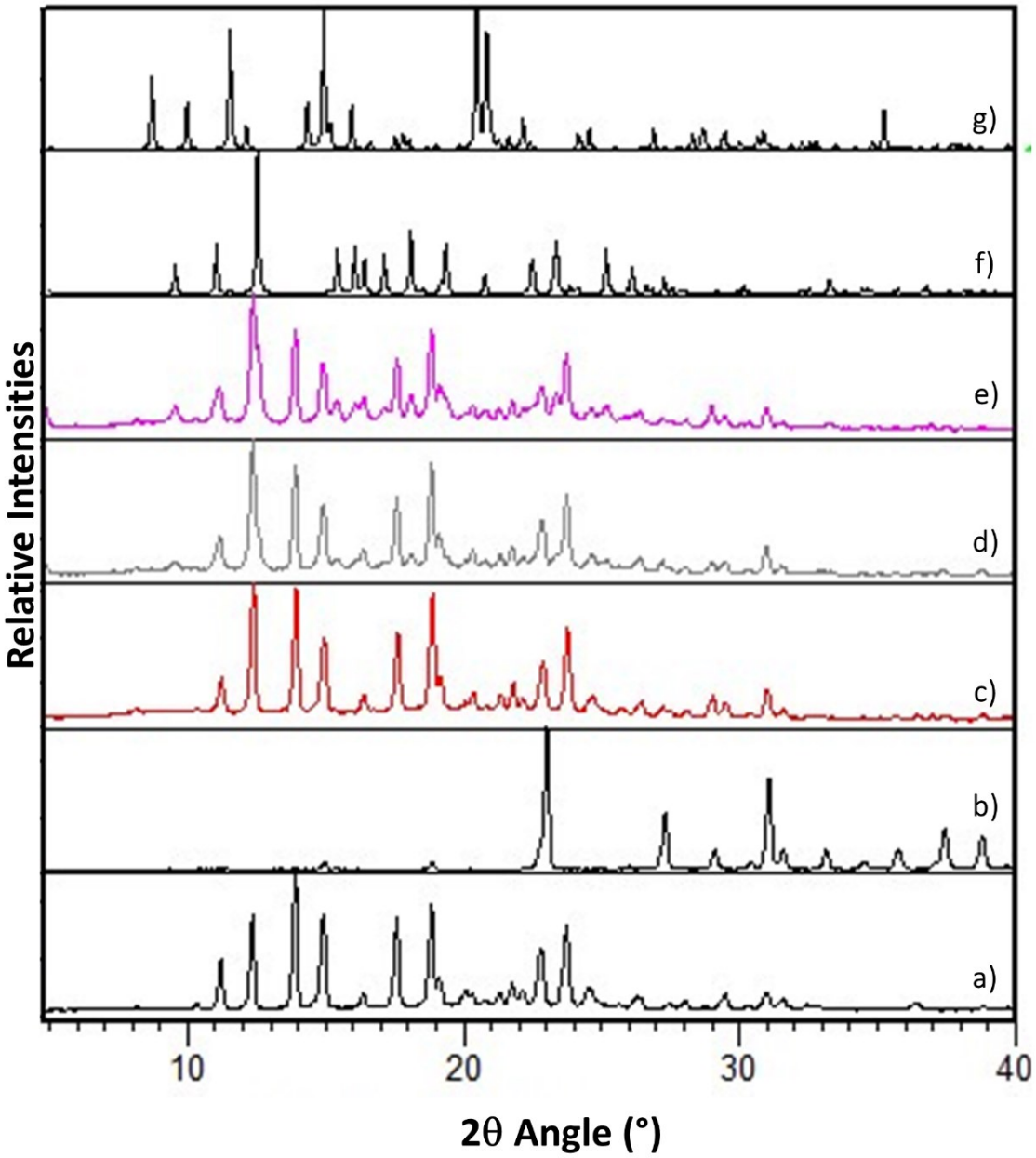

Figure S18. PXRD patterns of: (a) pure **vin**, (b) pure H_2**oxa**, (c), (d), (e) solids obtained through LAG of **vin** and H_2**oxa** in the presence of hexane (η=0.15 µL mg^{-1}) for 20, 40 and 60 minutes respectively, (f) calculated pattern of Form I, (g) calculated pattern of Form II.

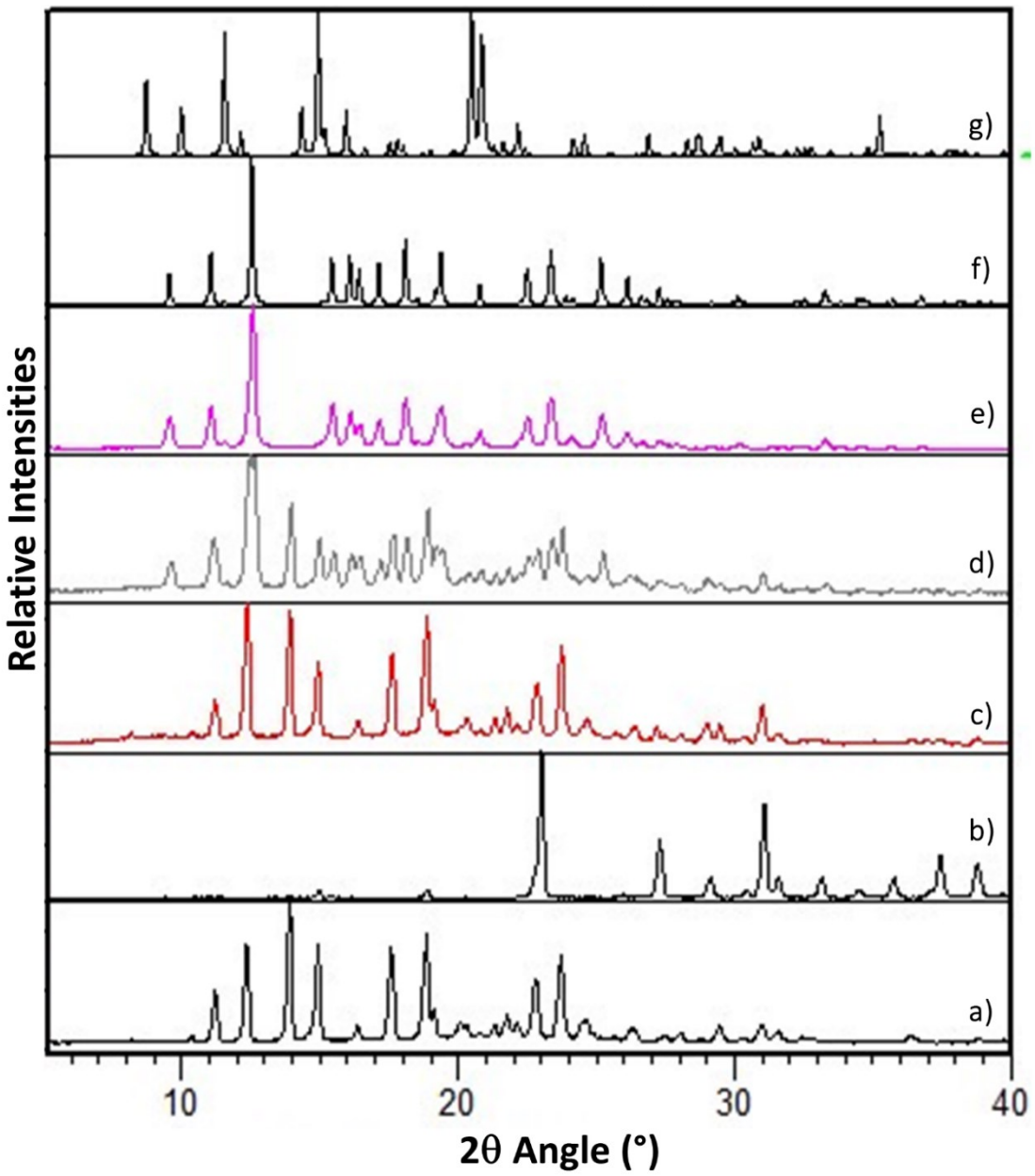

Figure S19. PXRD patterns of: (a) pure **vin**, (b) pure H_2**oxa**, (c), (d), (e) solids obtained through LAG of **vin** and H_2**oxa** in the presence of hexane (η=0.30 μL mg^{-1}) for 20, 40 and 60 minutes respectively, (f) calculated pattern of Form I, (g) calculated pattern of Form II.

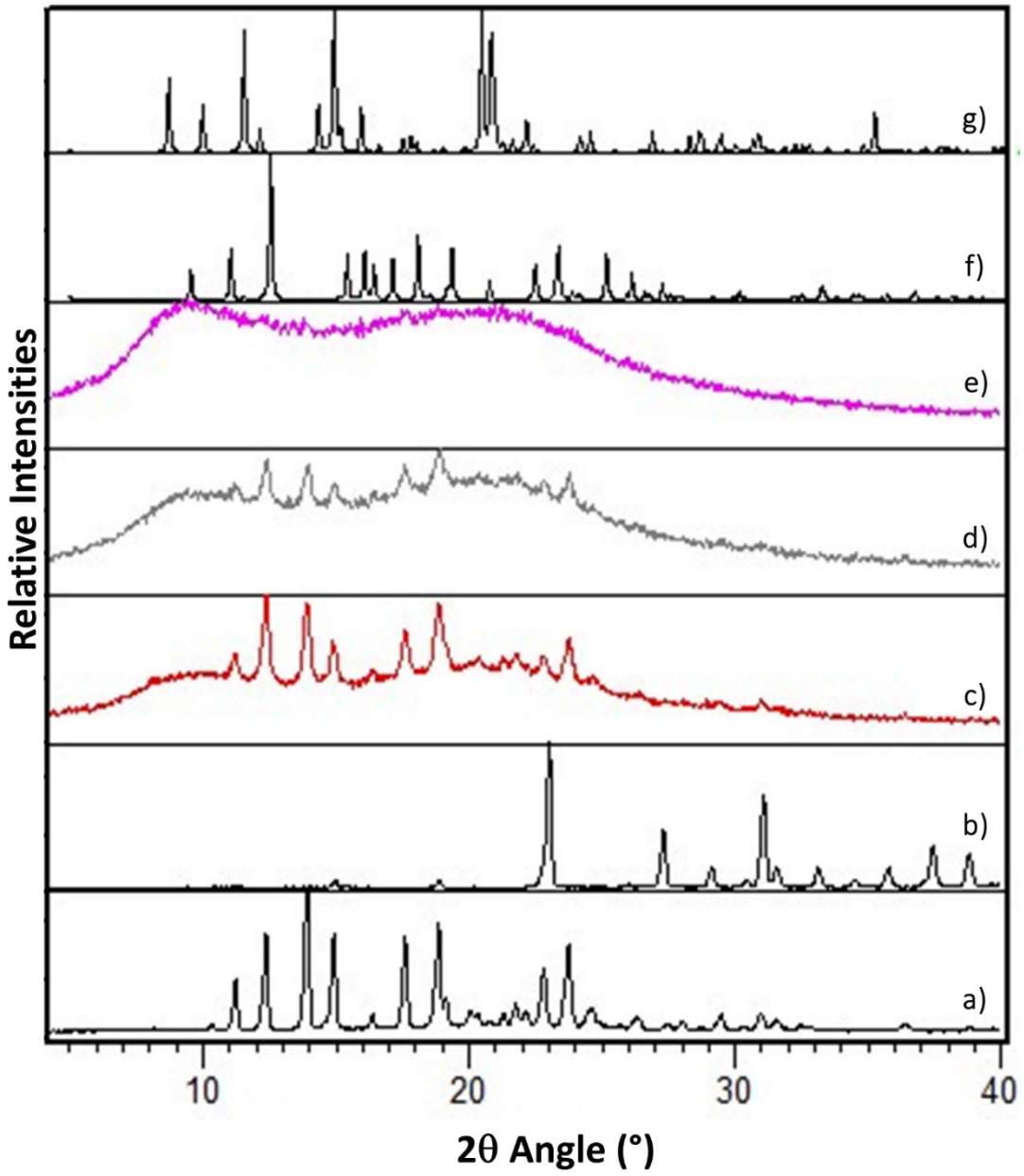

Figure S20. PXRD patterns of: (a) pure **vin**, (b) pure H_2**oxa**, (c), (d), (e) solids obtained through LAG of **vin** and H_2**oxa** in the presence of methanol (η=0.05 μL mg^{-1}) for 20, 40 and 60 minutes respectively, (f) calculated pattern of Form I, (g) calculated pattern of Form II.

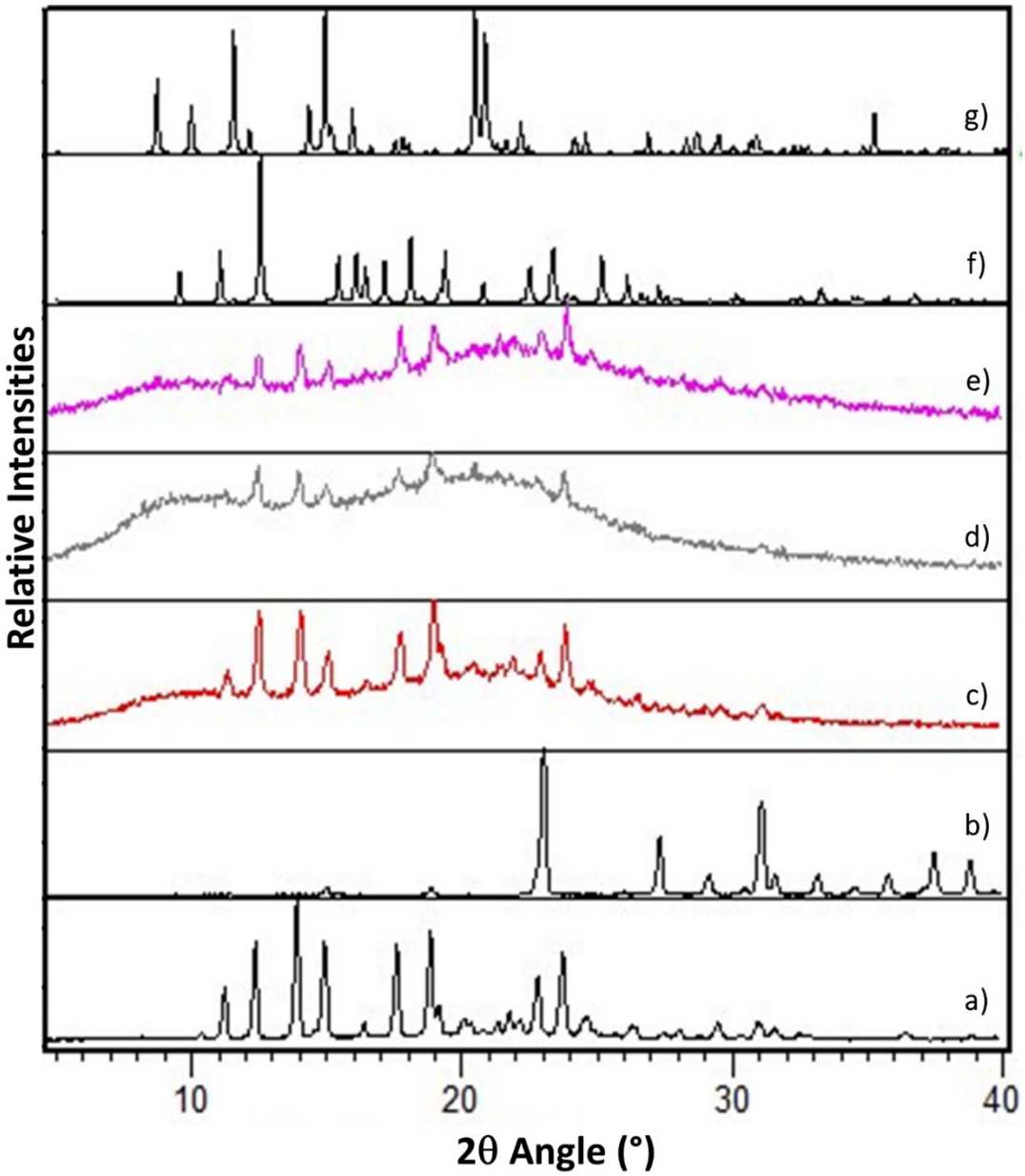

Figure S21. PXRD patterns of: (a) pure **vin**, (b) pure H_2**oxa**, (c), (d), (e) solids obtained through LAG of **vin** and H_2**oxa** in the presence of methanol (η=0.15 μL mg^{-1}) for 20, 40 and 60 minutes respectively, (f) calculated pattern of Form I, (g) calculated pattern of Form II.

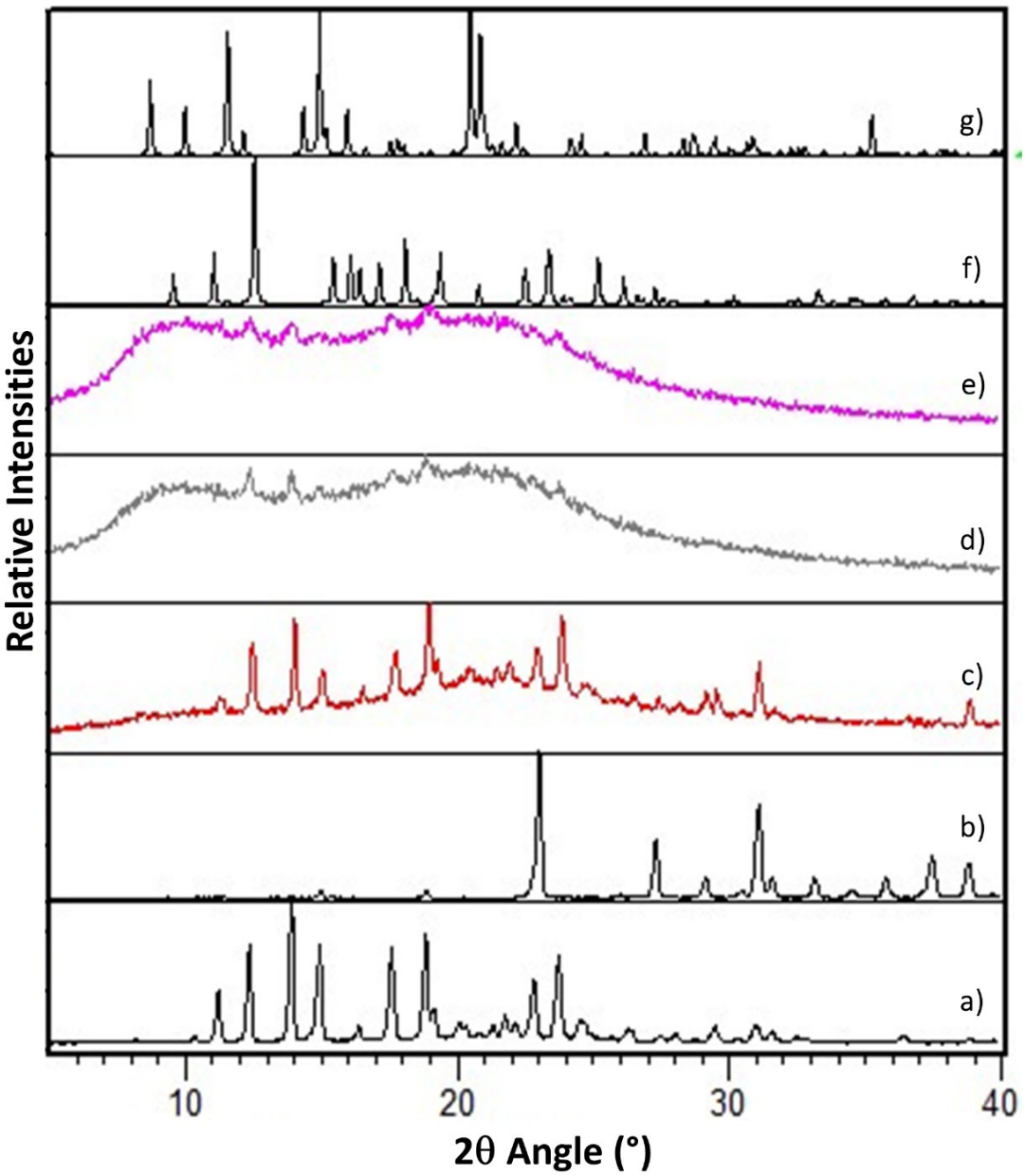

Figure S22. PXRD patterns of: (a) pure **vin**, (b) pure H_2**oxa**, (c), (d), (e) solids obtained through LAG of **vin** and H_2**oxa** in the presence of methanol (η=0.30 μL mg^{-1}) for 20, 40 and 60 minutes respectively, (f) calculated pattern of Form I, (g) calculated pattern of Form II.

2.2.4 Theophylline:fluorobenzoic acid cocrystals

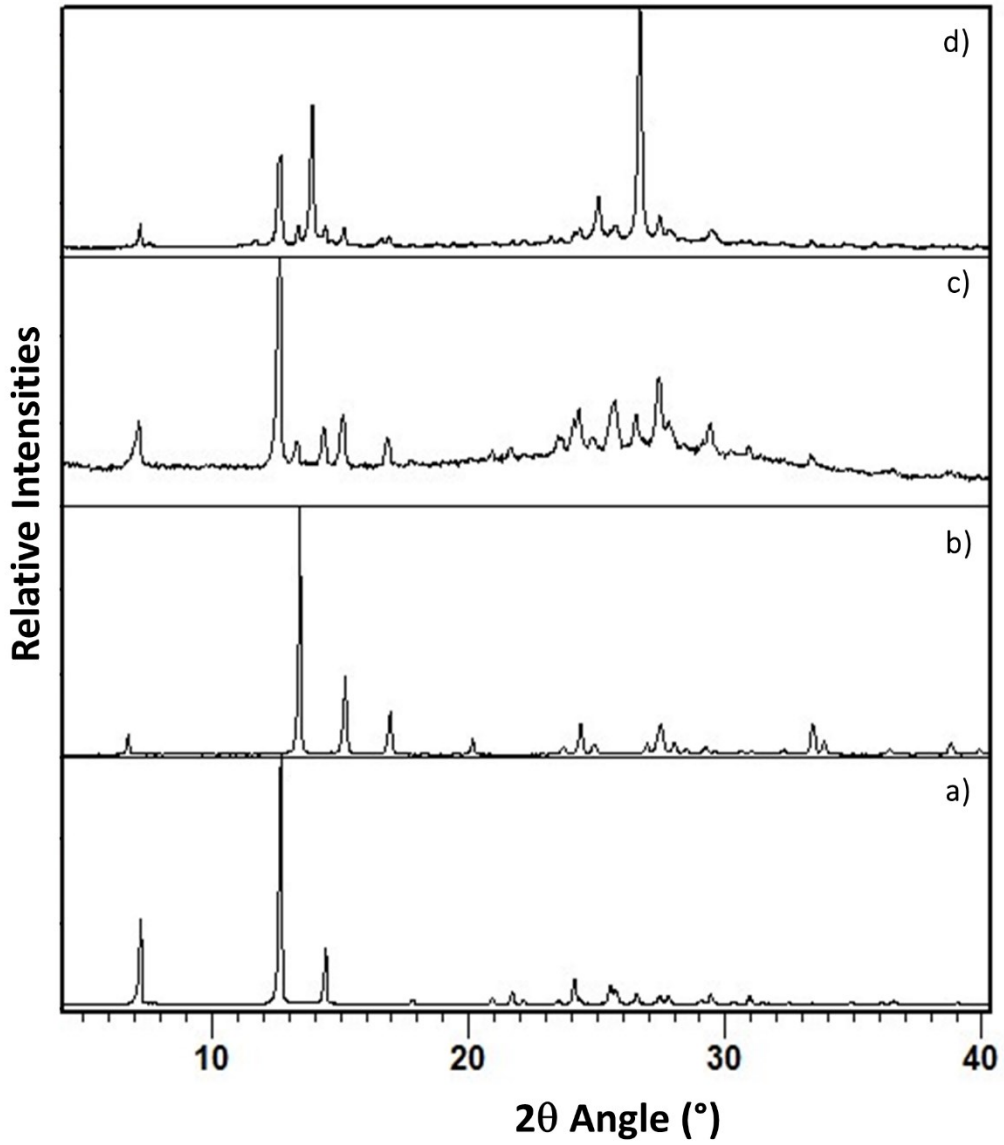

Figure S23. PXRD patterns of: (a) pure **thp**, (b) pure **23diFBA**, (c) solid product obtained after LAG of **thp** and **23diFBA** in the presence of nitromethane (η=0.25 µL mg^{-1}) (d) solid product obtained after LAG of **thp** and **23diFBA** acid in the presence of ethanol (η=0.25 µL mg^{-1}).

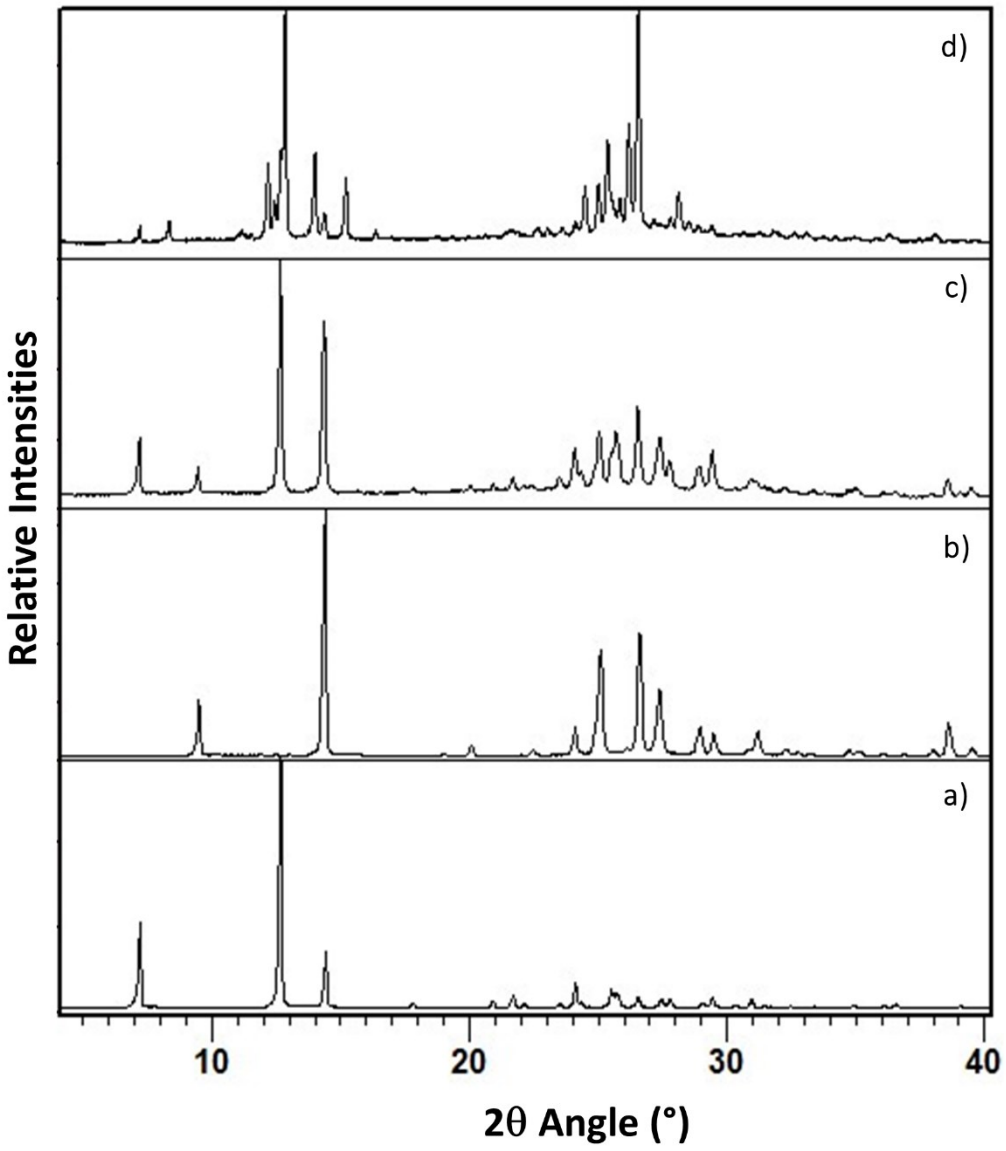

Figure S24. PXRD pattern of: (a) pure **thp**, (b) pure **26diFBA**, (c) solid product obtained through LAG of **thp** and **26diFBA** in the presence of nitromethane (η=0.25 µL mg^{-1}) (d) solid product obtained through LAG of **thp** and **26diFBA** in the presence of ethanol (η=0.25 µL mg^{-1}).

3. Probing the effect of presence of water/humidity during the grinding experiments

3.1 Experimental Section

3.1.1 LAG experiments

A series of additional milling experiments were performed to investigate the effects of trace amounts of water on the outcome of LAG reactions**.** Before each experiment, H_2**oxa** was stored in the oven at 140 °C to dehydrate H_2**oxa** and to remove adsorbed water traces from H_2**oxa** crystallites. The equimolar mixture of **vin** and oven-dried H_2**oxa** were processed for 60 min using in a *Retsch MM400* mixer mill, at 30 Hz frequency, with the addition of of each of the following liquids (η=0.10 mg mL^{-1}): deionised water, hexane, ethylacetate, acetonitrile and acetone. In addition, a LAG reaction with deionised water at η=0.05 mg mL^{-1} was also performed. All liquids, except deionised water, were dried over 3 Å molecular sieves. The other experimental conditions were kept similar to those reported in section 2.1.1. Immediately after completion of the milling reaction, the products were characterised by PXRD, TGA and DSC.

3.1.2 PXRD analysis

The reaction products were analysed on a *Bruker* D8 powder diffractometer with CuK_α radiation at a wavelength of 1.5418 Å equipped with a *VANTEC2000* area detector. Three data frames, each covering a 20° 2ϑ range were collected, at 300 s per frame. The frames were integrated and merged using *Bruker GADDS* software.

3.1.3 Differential scanning calorimetry (DSC) and thermogravimetric analysis (TGA)

The TGA and DSC measurements were performed on a *Mettler Toledo TGA/DSC 2* instrument. Approximately 10 mg of each material were weighed in a 70 µL alumina pan. The samples were heated from 30 to 300 °C temperature, with a heating rate of 10 °C min^{-1}. The measurements were accomplished under the flow of dry nitrogen gas. The TGA and DSC curves were processed using the *Mettler STARe* 12.1 data evaluation software.

3.2 Results

3.2.1 LAG experiments with water

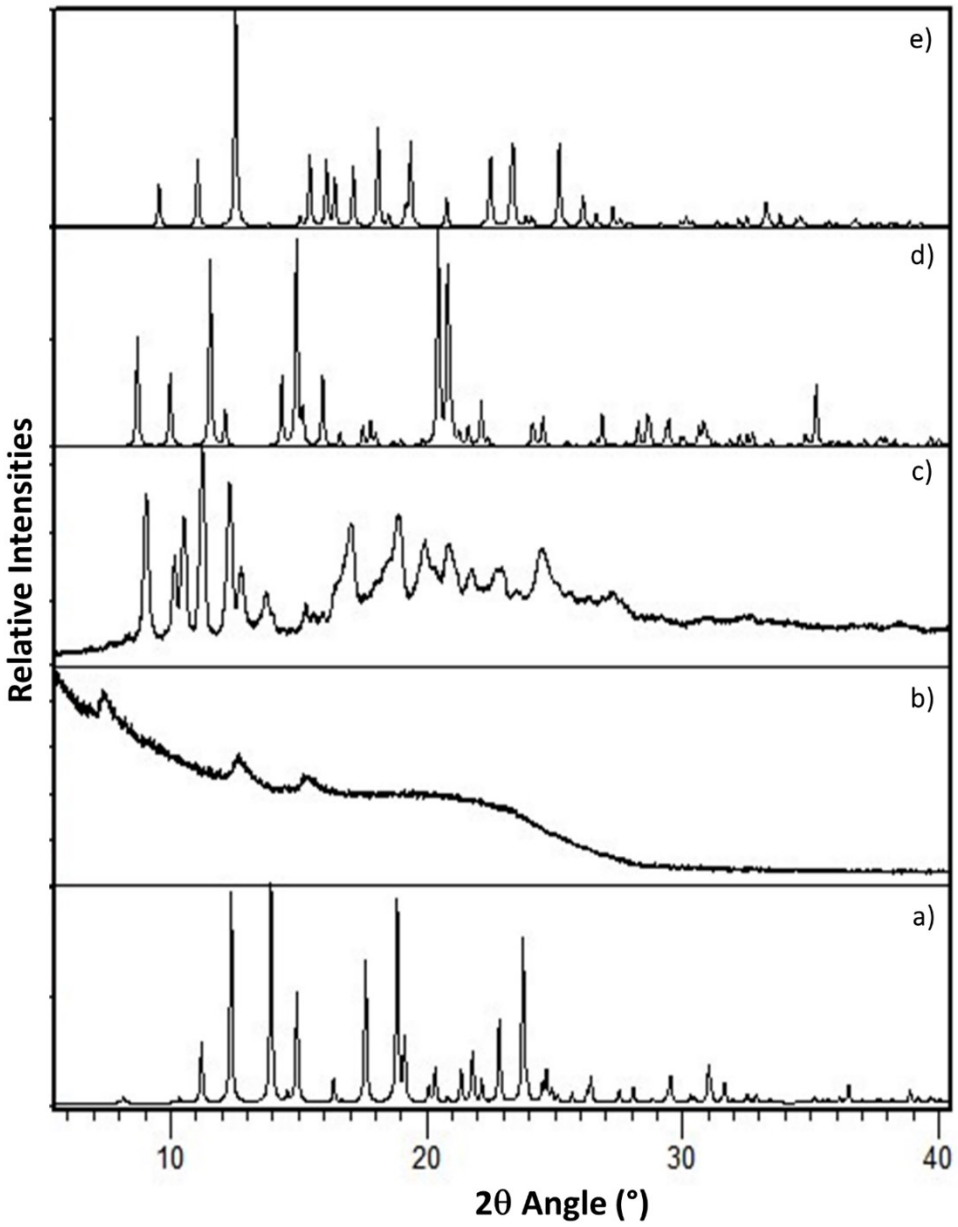

Figure S25. PXRD pattern of: (a) pure **vin**, (b), (c) solids obtained through LAG of **vin** and H_2**oxa** in the presence of water (η=0.05 µL mg^{-1} and 0.10 µL mg^{-1}, respectively) (d) and (e) calculated Form I and Form II, respectively.

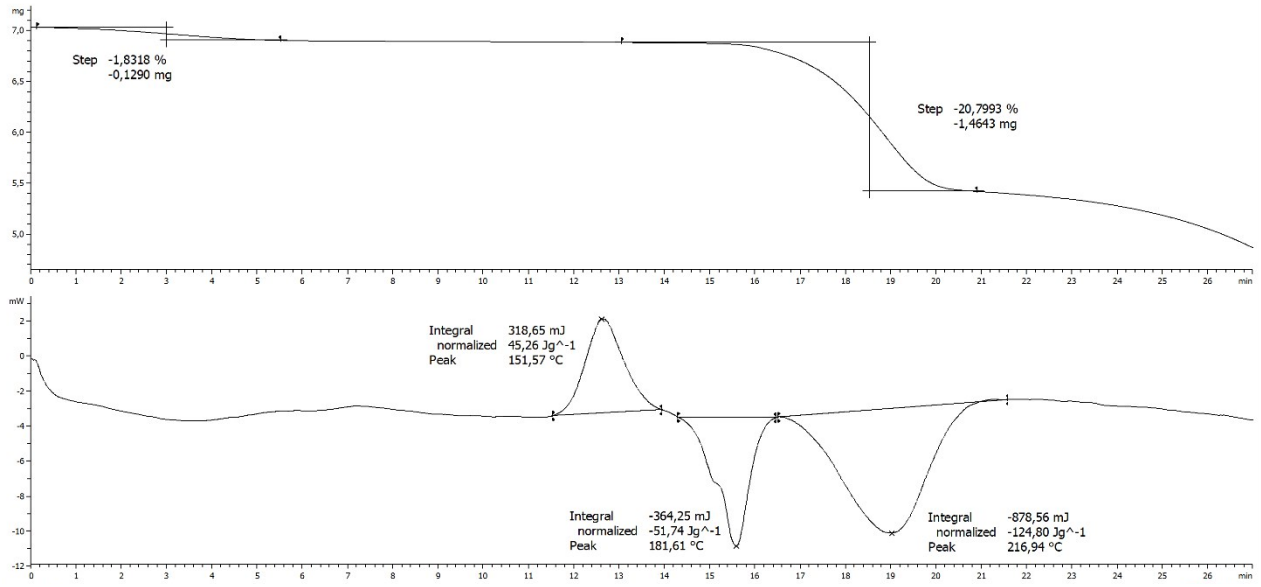

Figure S26. TGA (top) and DSC (bottom) thermograms of the solid obtained through LAG of **vin** and H_2**oxa** in the presence of water (η=0.05 µL mg^{-1}).

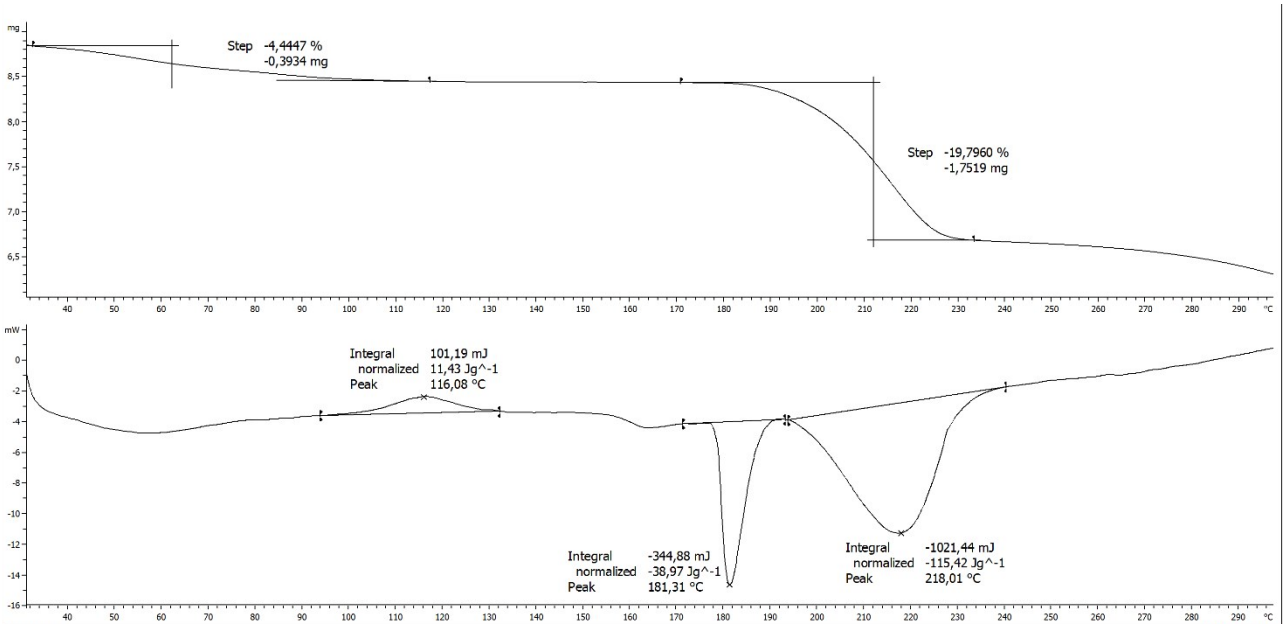

Figure S27. TGA (top) and DSC (bottom) thermograms of the solid obtained through LAG of **vin** and H_2**oxa** in the presence of water (η=0.10 µL mg^{-1}).

3.2.2 LAG experiments with dried liquid additives

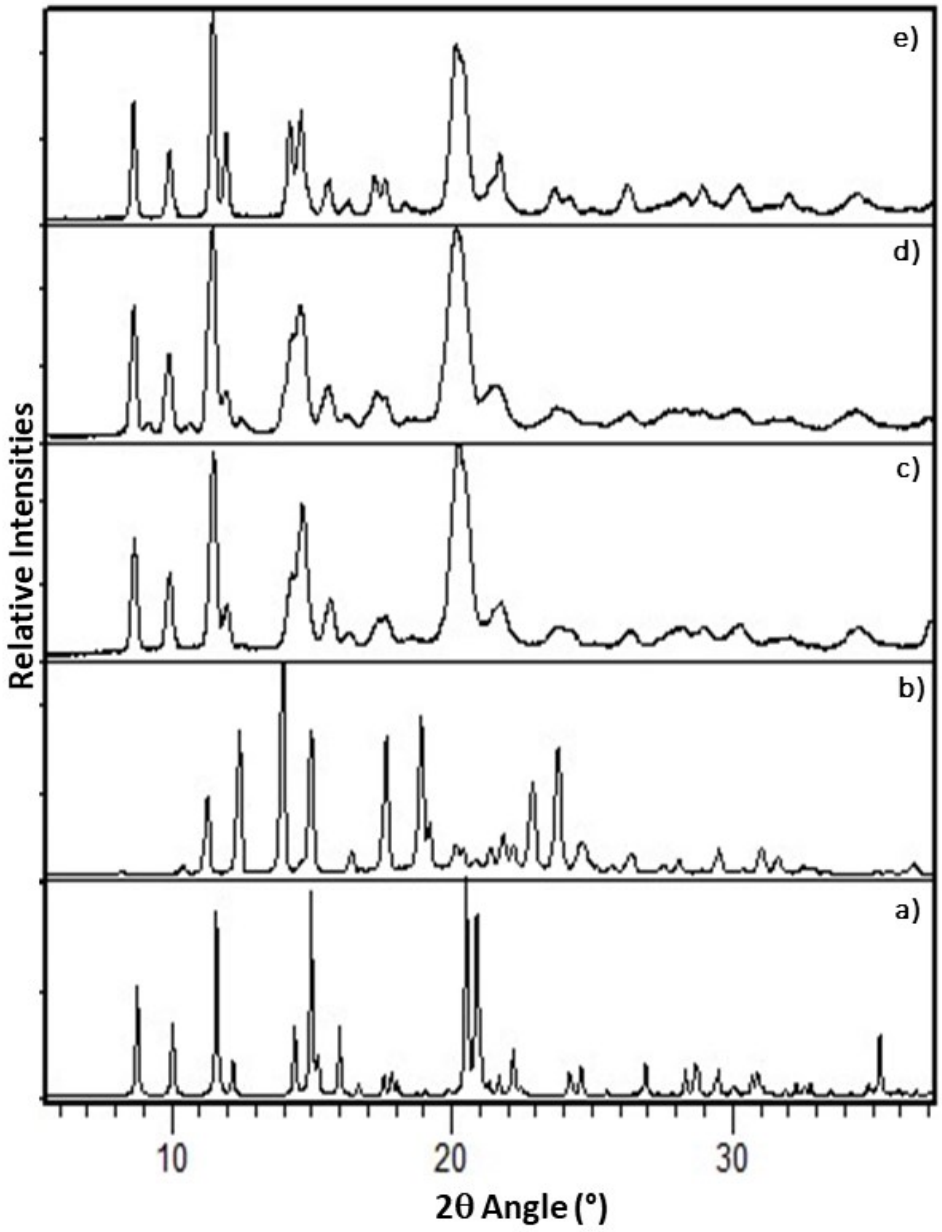

Figure S28. PXRD pattern of: (a) calculated Form II, (b) pure **vin**, (c), (d) and (e) solid products obtained after LAG of **vin** and H_2**oxa** with *dried* ethyl acetate, *dried* acetonitrile and *dried* acetone (η=0.10 µL mg^{-1}), respectively.

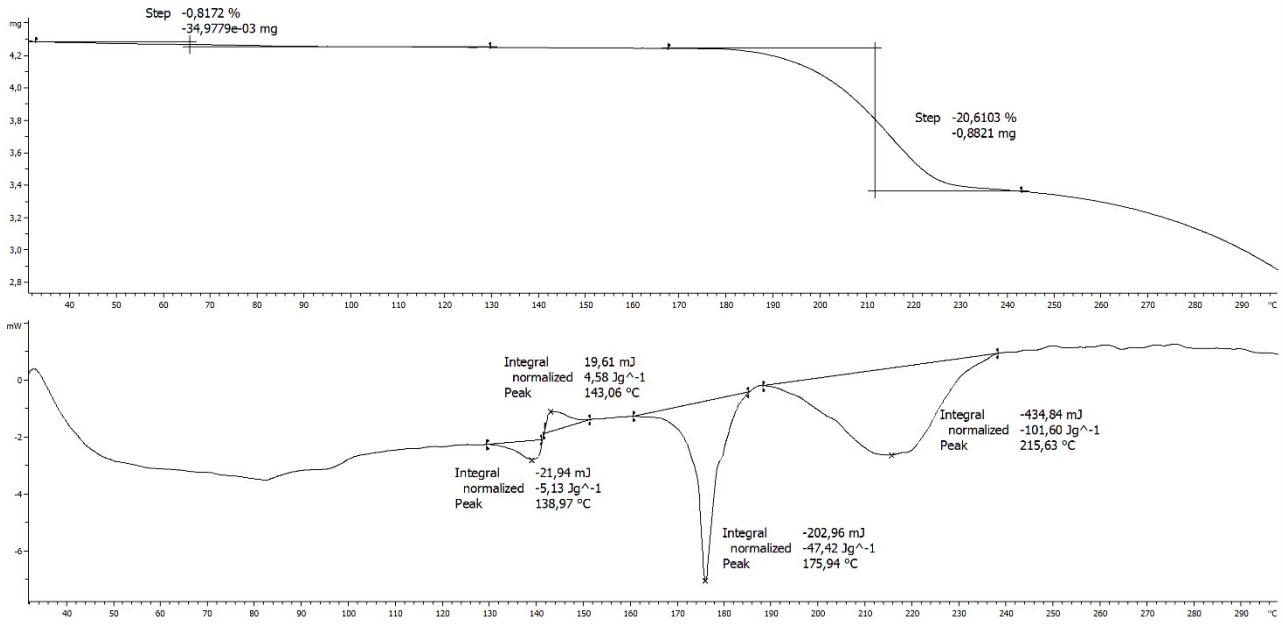

Figure S29. TGA (top) and DSC (bottom) thermograms of the solid product obtained after LAG of **vin** and H_2**oxa** with *dried* ethyl acetate (η=0.15 µL mg^{-1}).

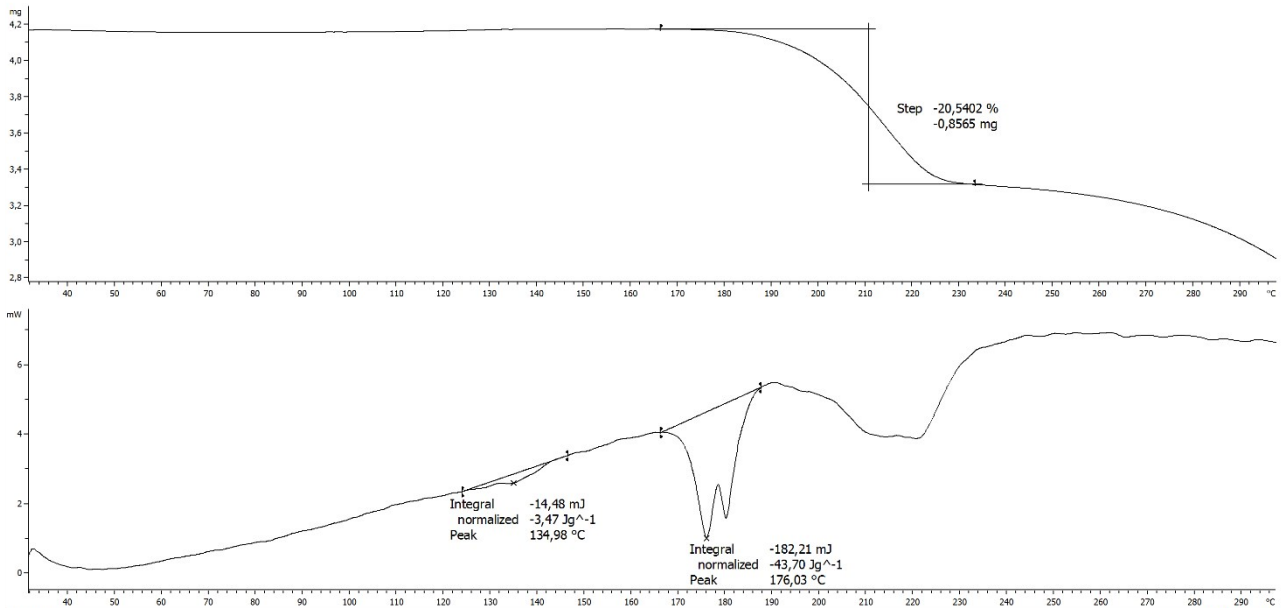

Figure S30. TGA (top) and DSC (bottom) thermograms of the solid product obtained after LAG of **vin** and H_2**oxa** with *dried* acetonitrile (η=0.15 µL mg^{-1}).

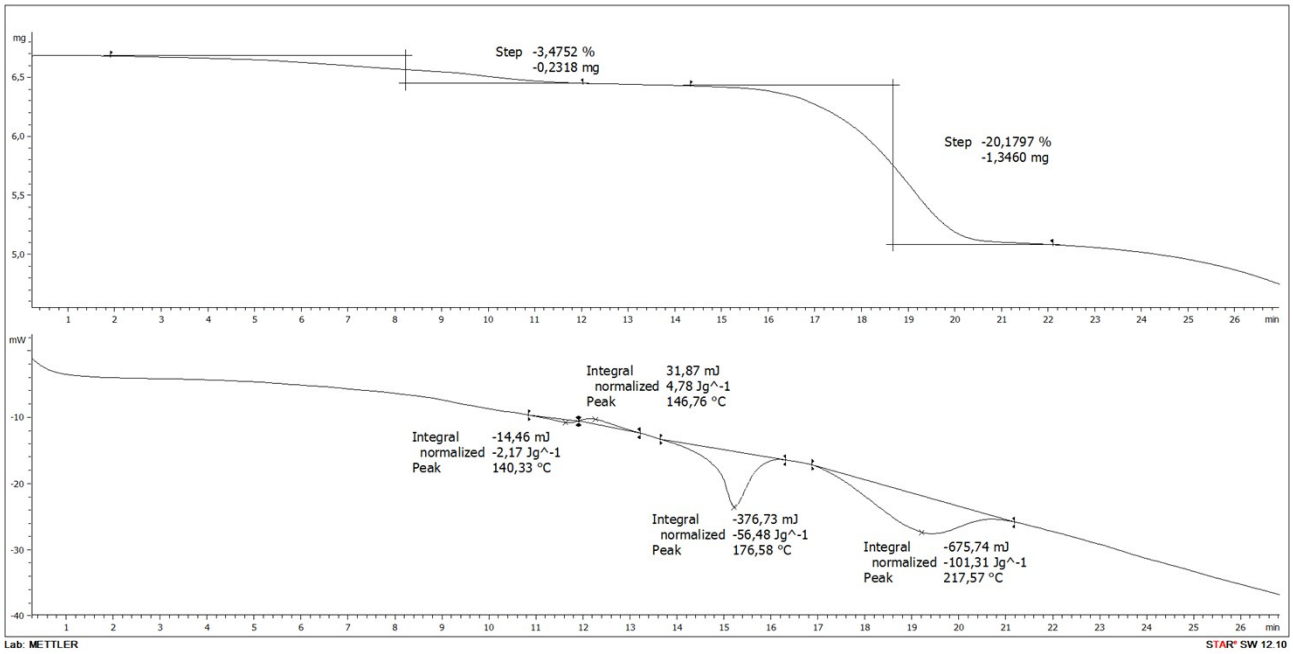

Figure S31. TGA (top) and DSC (bottom) thermograms of the solid product obtained after LAG of **vin** and H_2**oxa** with *dried* acetone (η=0.15 µL mg^{-1}).

4. Structure determination by X-ray crystallography

4.1 Structure determination of (Hvin$^+$)·(Hoxa$^-$), Form I

The crystal structure of Form I was solved from capillary PXRD data using a mecahnochemically prepared sample of (H**vin**$^+$)·(H**oxa**$^-$) (see section 2.1.1). The diffraction data was collected at room temperature and in transmission mode using a two-axis *Stoe StadiP* diffractometer equipped with a Cu anode, a Ge⟨111⟩ monochromator, a *Dectris Mythen 1K* detector and a small-aperture collimator. The Cu$K_{\alpha 1}$ X-rays (λ=1.54056 Å) were generated at 40 kV and 30 mA. The diffraction data was collected in the 2 to 60° 2ϑ range in steps of 0.015° 2ϑ with a count time of 1 s per step. The sample was placed in a flame-sealed a 0.7 mm diameter borosilicate glass capillary.

The pattern was indexed with *N-TREOR*[1] algorithm, via the interface of *EXPO2014*[2] software. The *EXPO2014* program was also used for space group determination and simulated annealing structure solution. Rietveld refinement was performed with *TOPAS Academic* v. 6.[3] Molecular framgments of **vin** cation and H_2**oxa** anion were defined via rigid bodies, with flexible torsion angles defined for the rotatable C–C bonds. Background was modelled with a Chebyshev polynomial function and the diffraction peak shapes were defined with a pseudo-Voigt function. Atomic vibrations were modelled with a single isotropic Debye-Waller factor. The Rietveld refinement results are shown in Table S1 and Figure S32.

Table S1. Crystallographic data the structure of **(**H**vin**$^+$**)·(**H**oxa**$^-$**)** *Form I* determined from powder X-ray diffraction data.

	Form I
chemical formula	$C_{24}H_{28}N_2O_6$
M_r / g mol^{-1}	440.48
crystal system	monoclinic
space group	*C*2
a / Å	18.560(1)
b /Å	7.5949(4)
c / Å	8.0212(5)
α / °	90
β / °	96.383(5)
γ / °	90
V / Å^3	1123.7(1)
Z	2
D_c / gcm^{-3}	1.3019(1)
F(000)	468
radiation type	CuK_α
T / K	296(2)
R_{wp}	0.072
R_p	0.055
R_{Bragg}	0.037
χ^2	3.078
CCDC deposition number	2024365

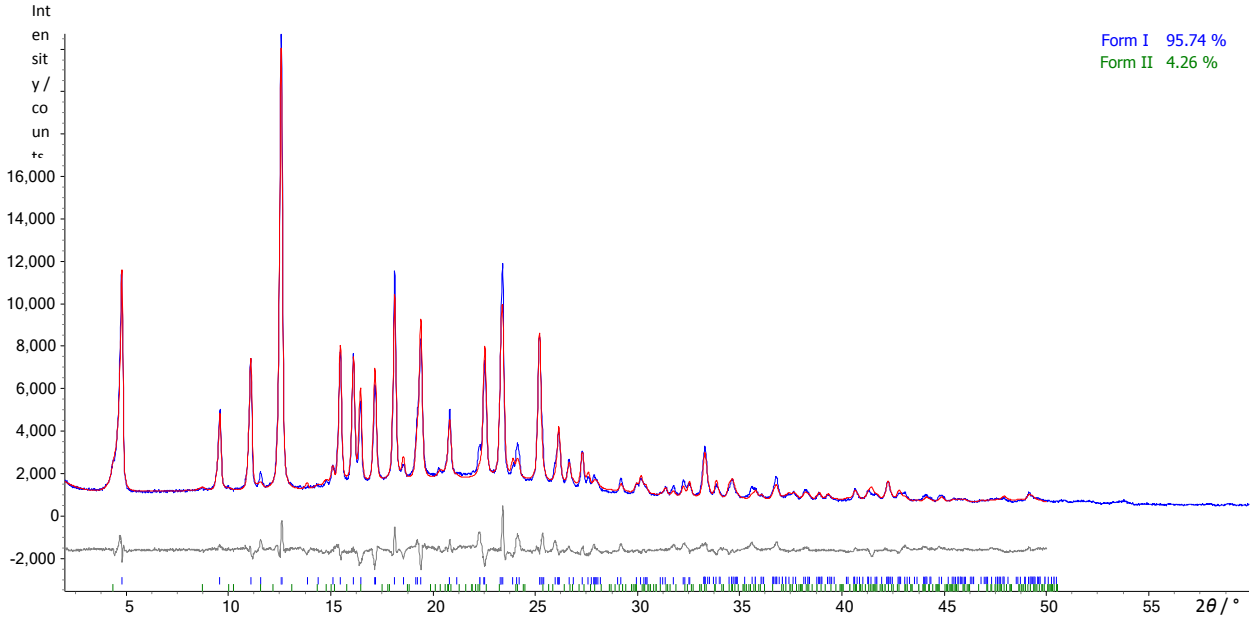

Figure S32. Rietveld refinement of (H**vin**$^+$)·(H**oxa**$^-$) Form I. The experimental diffraction profile is shown in blue, the calculated profile in red, and the difference curve is shown is grey.

4.2 Structure determination of (Hvin$^+$)·(Hoxa$^-$), Form II and (Hvin$^+$)·(Hoxa$^-$)·(EtOAc)$_{0.16}$

The crystal structures of (H**vin**$^+$)·(H**oxa**$^-$) Form II and the (H**vin**$^+$)·(H**oxa**$^-$)·(EtOAc)$_{0.16}$ solvate were determined using single crystal X-ray diffraction data. Single crystals of (H**vin**$^+$)·(H**oxa**$^-$) Form II were obtained by slow evaporation of a solution of mechanochemically prepared. Specifically, 0.115 mmoles of **vin** and H_2**oxa** were transfererred in a 10 mL glass vial. Subsequently, 4 mL of ethyl acetate were added and the components were dissolved through vigorous stirring using a magnetic stir bar. The obtained solution was left to evaporate slowly at room temperature. Single crystals of (H**vin**$^+$)·(H**oxa**$^-$) were obtained after 5 days and left to dry at ambient conditions for one week after they were isolated through filtration. Single crystals of (H**vin**$^+$)·(H**oxa**$^-$)·(EtOAc)$_{0.16}$ were obtained from a hot and concentrated EtOAc solution of (H**vin**$^+$)·(H**oxa**$^-$), Form I. Crystals suitable for diffraction studies were obtained once the solution reached room temperature.

Single X-ray diffraction data from a colourless and prism-shaped crystals of Form II (0.05×0.19×0.23 mm^3) and the solvate (0.05×0.11×0.39 mm^3) were collected on a dual-source *Agilent SuperNova* single crystal X-ray diffractometer using a micro-focus Cu X-ray beam (λ=1.54184 Å, generated at 50 kV and 0.8 mA) and a 135 mm *Atlas* CCD detector. The sample temperature was controlled with an *Oxford Instruments Cryojet5*. The data was acquired, processed and corrected using the *CrysAlisPro* program.[4] Structure solution and refinement were accomplished using the *Olex2* program suite (Form II)[5] and *SHELXLE*.[6] The structure was solved using *SHELXT*,[7] while structure refinement was accomplished using *SHELXL*.[8] All non-hydrogen atoms were refined anisotropically, while hydrogen atoms associated with the carbon, oxygen and nitrogen atoms were refined isotropically in geometrically constrained positions.

(H**vin**$^+$)·(H**oxa**$^-$)·$(EtOAc)_{0.16}$: The geometry of the disordered ethyl group of H**vin**$^+$ and the disordered EtOAc molecule were modelled using a range of *SHELX* restraints and constraints, namely DFIX, SADI, DELU, EADP and EXYZ.

(H**vin**$^+$)·(H**oxa**$^-$), *Form II*: The latter stages of the structure refinement suggested that the ethyl ester group is disordered over two positions. However, the crystal structure of Form II is presented without a disordered ethyl group owing to the insignificant improvement of its structural model and the resulting refinement parameters, which could only be achieved through the extensive use of SHELX restraints and constraints. Further structural analyses also revealed that the crystal structure exhibits sizeable voids. The solvent-mask procedure in *Olex2* was applied to determine that each void displays a size of 105 Å^3 and an electron count of 4 e$^-$. The final refinement of the reported crystal structure was accomplished *without* the use of the *Olex2 Solvent Mask* routine and a solvent-corrected hkl file, although the use of such corrected hkl file results in negligibly better refinement parameters. Such approach was justified by the insignificant electron count in each void.

The crystal structure of the ethyl acetate hemisolvate is shown in Figure S33. The crystallographic and refinement parameters for Form II and the ethyl acetate hemisolvate are shown in Table S2.

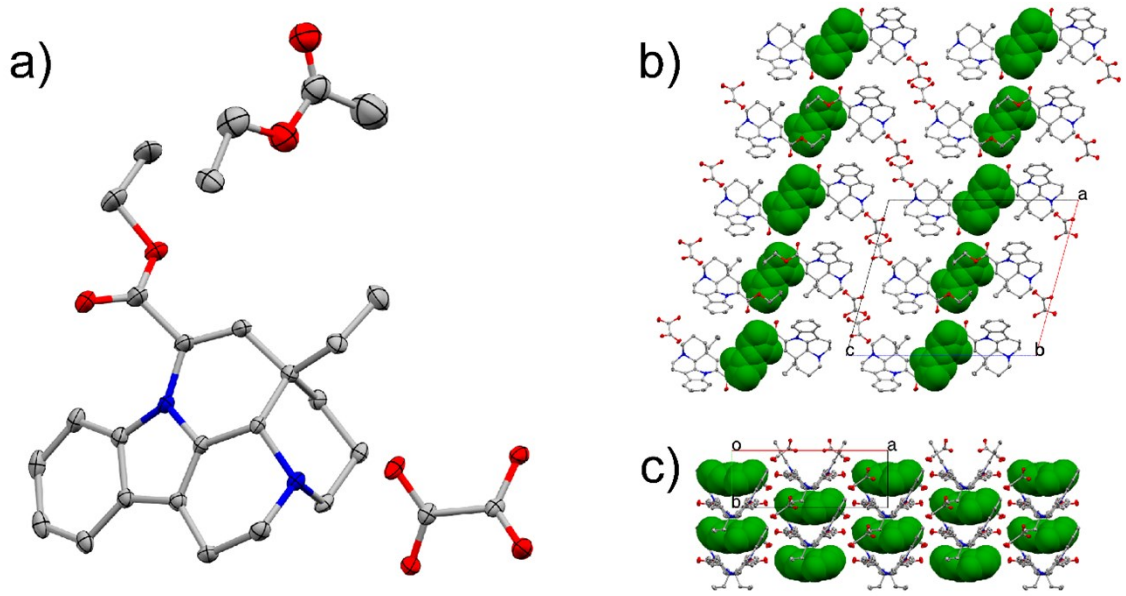

Figure S33. Perspective view of the asymmetric unit of the crystal structure of the ethylacetate hemisolvate (a). Crystal packing diagrams viewed along the crystallographic axes *b* and *c* are shown in b) and c), respectively. All disordered functional groups and hydrogen atoms are omitted for clarity. The thermal ellipsoids of all atoms are drawn at the 50% probability level. Atom colour scheme: carbon – grey, oxygen – red, nitrogen – blue. The disordered ethyl acetate molecules are shown in green using a space-fill model in b) and c).

Table S2: Crystallographic and refinement parameters for (H**vin**$^+$)·(H**oxa**$^-$) Form II and (H**vin**$^+$)·(H**oxa**$^-$)·(EtOAc)$_{0.16}$.

	Form II	**EtOAc solvate**
chemical formula	$C_{24}H_{28}N_2O_6$	$C_{24.63}H_{29.26}N_2O_{6.32}$
M_r / g mol^{-1}	440.48	454.41
crystal system	monoclinic	monoclinic
space group	*C*2	*C*2
a / Å	17.9007(2)	17.8855(2)
b /Å	6.30220(10)	6.32180(10)
c / Å	20.9554(2)	21.0313(3)
α / °	90	90
β / °	105.3560(10)	105.3460(10)
γ / °	90	90
V / Å^3	2279.66(5)	2293.19(6)
Z	4	4
D_c / gcm^{-3}	1.283	1.317
F(000)	936	967
μ(CuK_α) / mm^{-1}	0.763	0.783
T / K	150.0(1)	110.0(1)
crystal size / mm^3	0.05 × 0.19 × 0.23	0.05 × 0.11 × 0.39
index range	−22 → 22 −7 → 7 −25 → 25	−22 → 22 −7 → 7 −25 → 25
collected reflections	40113	37992
unique reflections	4465	4462
R_{int}	0.0379	0.0574
reflections with $I > 2\sigma(I)$	4385	4366
no. parameters	293	366
$R(F)$, $F > 2\sigma$(F)	0.0271	0.0336
$wR(F^2)$, $F > 2\sigma$(F)	0.0738	0.0879
$R(F)$, all data	0.0277	0.0344
$wR(F^2)$, all data	0.0745	0.0887
Δ_r (min., max.) e Å^{-3}	−0.185, 0.185	−0.228, 0.277
CCDC deposition number	2024366	2024367

5. Solid-state NMR analysis

Solid-state NMR spectra were acquired with a *Bruker Avance II 400 Ultra Shield* instrument, operating at 400.23, 100.63 and 40.56 MHz for ^{1}H, ^{13}C and ^{15}N nuclei, respectively. Powder samples were packed into cylindrical zirconia rotors with a 4 mm o.d. and a 80 μL volume and spun at 12 (^{13}C) or 9 (^{15}N) kHz. ^{13}C and ^{15}N CPMAS spectra were acquired using a ramp cross-polarisation pulse sequence with a 90° ^{1}H pulse of 3.60 μs, a contact time of 3 (^{13}C) or 4 (^{15}N) ms, optimised recycle delays between 1 and 2.5 s, and a number of scans in the range 850-2100 (^{13}C) or 65000-77500 (^{15}N), depending on the sample. For every spectrum, a two-pulse phase modulation (TPPM) decoupling scheme was used, with a radio frequency field of 69.4 kHz. The ^{13}C and ^{15}N chemical shift scales were calibrated through the external standard glycine (^{13}C methylenic signal at 43.7 ppm; ^{15}N peak at 33.4 ppm with respect to NH_3). Relevant NMR spectra are shown in Figure S34.

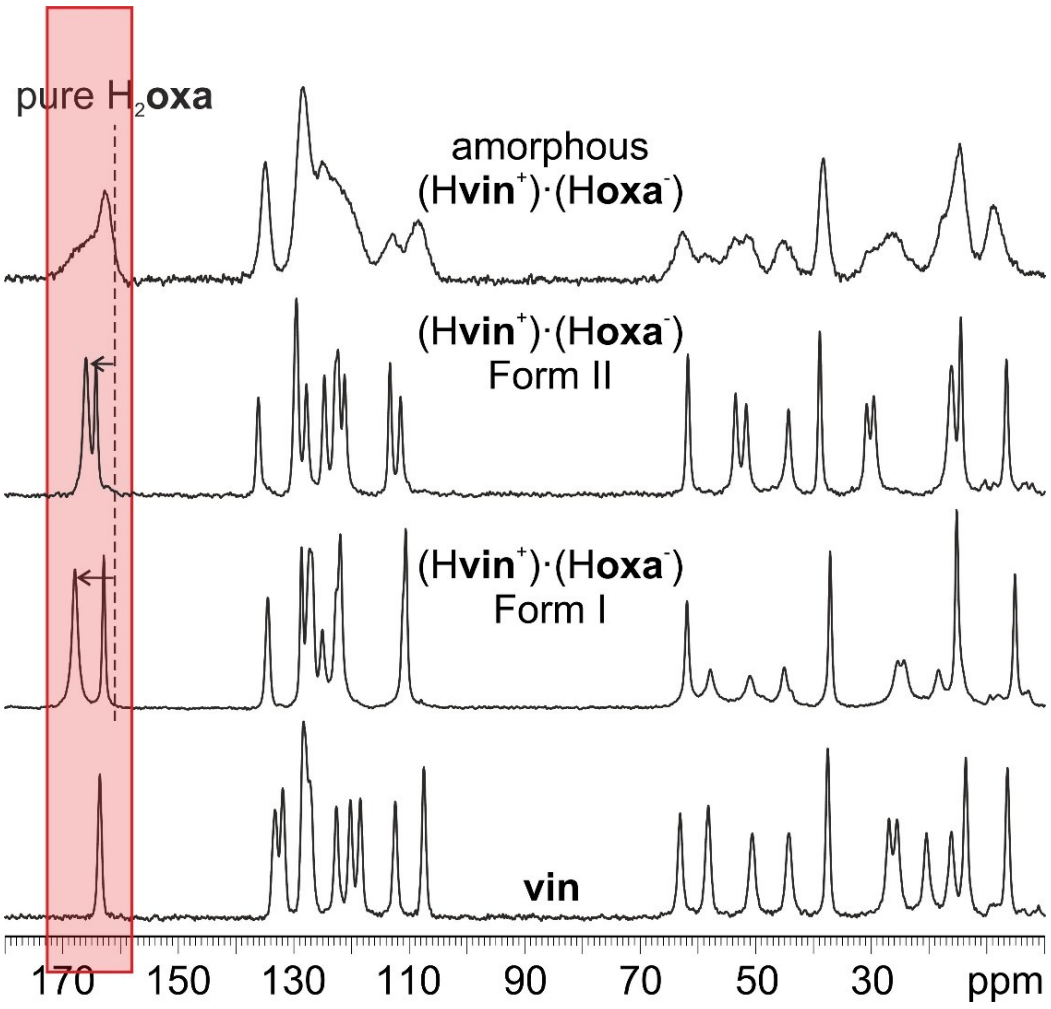

Figure S34. ^{13}C (100 MHz) CPMAS spectra of pure **vin**, Form I, Form II and amorphous (H**vin**$^{+}$)·(H**oxa**$^{-}$), acquired with a spinning speed of 12 kHz at room temperature. The dashed line represents the chemical shift of pure H_2**oxa**: the high-frequency shift of the signal is diagnostic of carboxylate formation.

6. DFT calculations

6.2 Experimental section

Periodic DFT calculations were performed using the plane-wave code *CASTEP 19*.[9] Input files were prepared using the program cif2cell.[10] Crystal structures were optimsed using PBE[11] functional supplemented by many-body dispersion (MBD*)[12–14] correction. The plane-wave basis set was truncated at 650 eV cutoff, and ultrasoft pseudopotentials were generated on the fly. Electronic Brillouin zone was sampled with a 0.03 $Å^{-1}$ Monkhorst-Pack k-point grid. Unit cell parameters and atomic coordinates were relaxed during the optimisation, subject to the space group symmetry constraints. The convergence criteria were set as follows: maximum energy change 10^{-5} eV $atom^{-1}$, maximum force on atom 0.03 eV $Å^{-1}$, maximum atom displacement 10^{-3} Å, maximum residual stress 0.05 GPa.

Molecular DFT calculations were performed in *Gaussian 16* version B01.[15] Geometries of the **vin** and H_2**oxa** molecules, the H**vin**$^+$ and H**oxa**$^-$ ions, as well as the hydrogen-bonded (H**vin**$^+$)·(H**oxa**$^-$) assemblies were geometry-optimised in the gas phase, as well as under SMD solvation model.[4] Calculations accomplished using the B3LYP[16,17] functional, combined with Grimme D2[18] semiemperical dispersion corrections, and the 6-311G(d,p) basis set. Default geometric convergence criteria were used. Interaction energies were corrected for basis set superposition error (BSSE) using the counterpoise method.

6.2 Results and discussion

The energies of proton transfer between **vin** and H_2**oxa** were calculated in order to rationalise the contrasting effects of different liquid additives, as well as the energy of formation of H**vin**$^+$:H**oxa**$^-$ hydrogen-bonded dimers in solution.

Table S3. Calculated energies for dimer formation and proton transfer in different solvents and gas phase.

Liquid additive	Energy of dimer formation / kJ mol^{-1}	Energy of proton transfer / kJ mol^{-1}	Type of liquid additive
methanol	−93.12	−35.72	**inhibitive**
ethanol	−88.81	−25.64	
DMSO	−84.27	−12.23	**prohibitive**
nitromethane	−83.66	−10.34	
acetone	−82.71	−0.86	**catalytic**
acetonitrile	−82.61	−10.20	
heptane*	−74.90	200.94	
gas phase	−70.49	400.44	

* Heptane was used as the closest analogue to hexane, since the hexane parameterisation is not available within the SMD model in *Gaussian 16*.

The solvent environment was modelled with a continuum SMD model. It was found that the energy of a proton transfer is most negative with inhibitive liquids and becomes less negative in the case of prohibitive liquids such as nitromethane and DMSO. In the case of catalytic liquids, the energy of proton transfer is either close to zero or positive. Conversely, the energy of dimer formation is negative for all solvents and even in the gas phase. Although such calculations lack of explicit treatment of intermolecular solute-solvent interactions, it is notable that liquids with identical modes of action (catalytic, inhibitive or prohibitive) can be also grouped together according to the calculated energies of proton transfer and dimer formation. Indeed, favourable energies of proton transfer in inhibitive solvents allow the H**vin**$^+$ and H**oxa**$^-$ ions to freely coexist without forming dimers, something that can occur in the amorphous (H**vin**$^+$)·(H**oxa**$^-$) salt. On the other hand, in the presence of catalytic solvents proton transfer is no longer favourable, unless the hydrogen-bonded H**vin**$^+$:H**oxa**$^-$ dimer, found in both polymorphs of crystalline (H**vin**$^+$)·(H**oxa**$^-$), is formed.

7. Dissolution Kinetic Tests

The dissolution kinetic tests (DKT) were performed under the same conditions as in a related and recent **vin** study.[19] Specifically, the determination of the concentration of **vin** in (H**vin**$^+$)·(H**oxa**$^-$) products was performed by using an *in situ* fiber-optic apparatus (Hellma, Italy), connected to a spectrophotometer (*Zeiss*, Germany) at UV wavelength of 313 nm (Figure S35). This technique allows an *in situ* determination of the concentration of a substance without perturbing the dissolution environment and often overcomes the problem connected to drug concentration measurements in the presence of generated solid particles. About 150 cm^3 of a 7.4 pH buffer (0.2 M KH_2PO_4/0.2 M NaOH) heated at 37 °C was used as dissolution medium. In these conditions, the solubility at equilibrium of pure **vin** is 1.6 mg/L.[19] In the present study, sink conditions were not maintained in order to build up the super-saturation, thus mimicking conditions in the gastro-intestinal tract and to allow possible events such as nucleation, crystallisation and precipitation.[20] Subsequently, an amount of solid product suitable to give 5 mg of **vin** was added to the dissolution medium (maximum concentration of 33.3 mg/L) and uniformity conditions were ensured by using an impeller at a rotational speed of 200 rpm. Each DKT lasted 60 min. Additionally, since monitoring drug concentrations by using an *in situ* fiber-optic probe without proper precautions may lead to an overestimation of drug concentration due to several causes, including the Tyndall effect,[21] the scattering effect due to the super-saturation phenomenon, occurring at every wavelength, was eliminated by a difference between the absorbance measured at 313 nm and that measured at 450 nm. The samples were tested in triplicate and the results were expressed as mean ± S.D. The **vin** calibration curve is shown in Figures S36. The solubilisation profiles of Form I, Form II and amorphous (H**vin**$^+$)·(H**oxa**$^-$) are shown in Figure S37.

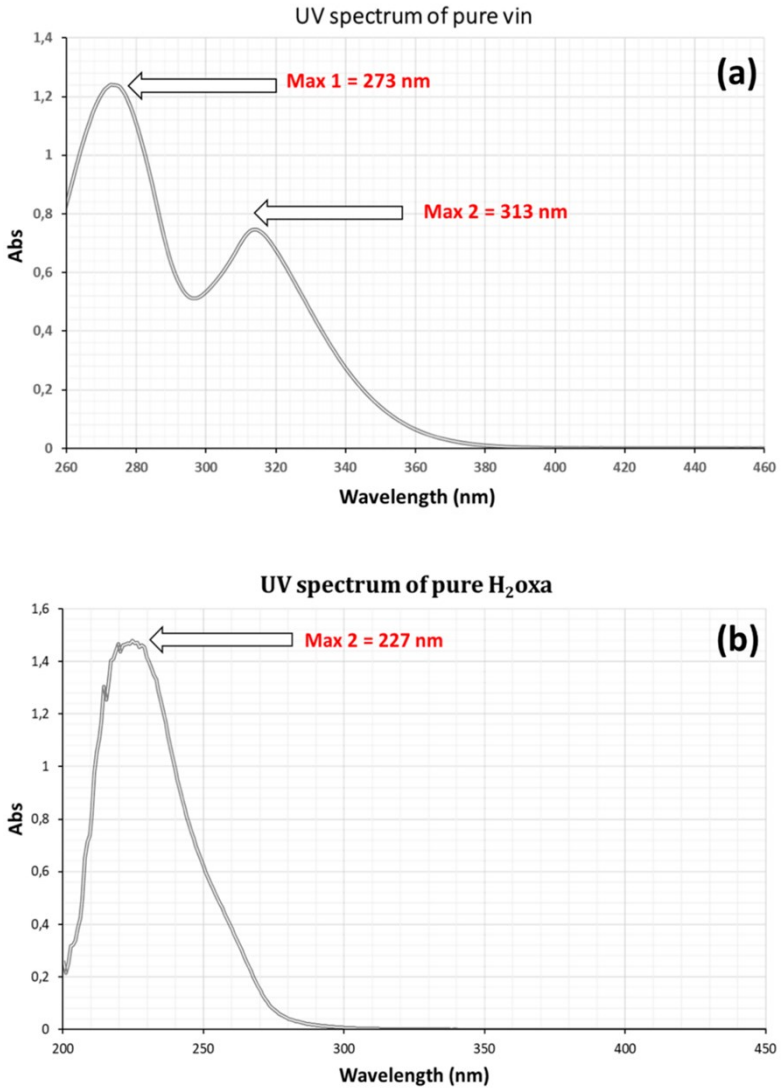

Figure S35. UV spectra of pure a) **vin** and b) pure H_2**oxa**.

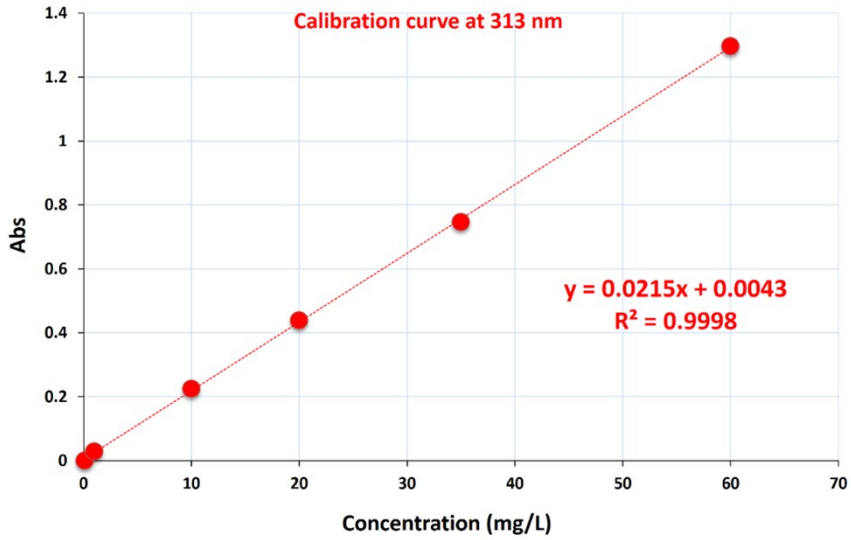

Figure S36. Calibration curve for **vin** at the UV wavelength of 313 nm.

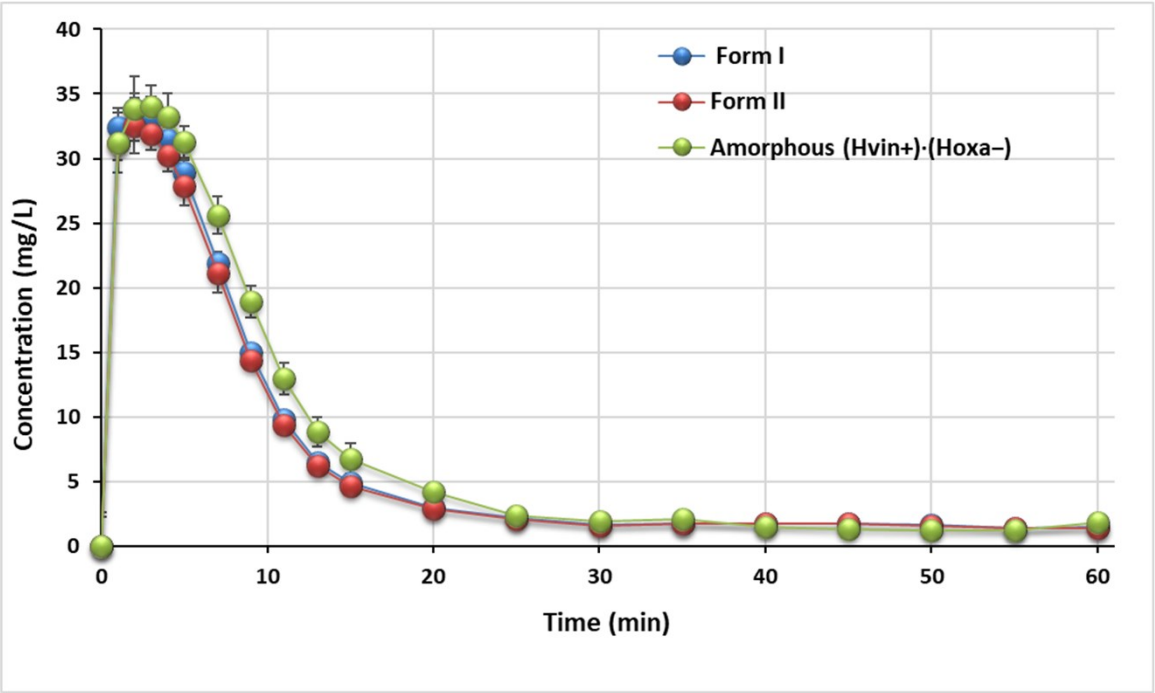

Figure S37. Dissolution profiles of the different solid forms of (H**vin**$^{+}$)·(H**oxa**$^{-}$). All solid forms show a dissolution profile typical of a protonated solid with a rapid and complete dissolution within 5 minutes of analysis, followed by precipitation of unprotonated **vin** due to supersaturation. The concentration reached a plateau at a value of 1.8 mg L^{-1}, close to the solubility at equilibrium of pure **vin** (1.6 mg L^{-1}). The dissolution profiles of Form I, Form II and amorphous (H**vin**$^{+}$)·(H**oxa**$^{-}$)are similar, suggesting that the solid form has not appreciably affected the solubilisation rate of **vin**.

8. Liquid-assisted grinding of selected cocrystals with prohibitive liquid additives

8.1 Theophylline:2,3-difluorobenzoic acid and theophylline:2,6-difluorobenzoic cocrystals

The mechanochemical syntheses of the (**thp**)·(**23diFBA**) and (**thp**)·(**26diFBA**) cocrystals was performed by LAG using a *Form-Tech Scientific FTS1000* shaker mill. Specifically, 200 mg of a physical mixture of equimolar amounts of **thp** and the fluorobenzoic acid were added to a 15 mL stainless steel grinding jar, along with 50 µL of ethanol and two 7 mm stainless steel milling balls. The mixer mill was operated at 30 Hz for 30 min. The obtained solids were subsequently analysed by powder X-ray diffraction using a *Stoe StadiP* diffractometer in transmission geometry and a monochromatic CuK_{α} X-ray source (λ = 1.54056 Å, generated at 40 kV and 30 mA). The data shown in Figures S38 and S39 was acquired in foil mode at room temperature (*ca.* 20 °C) in the 2–60° 2θ range (in continuous mode: 0.5° step, 10 s/step). The solids were characterised as cocrystals (rather than salts or solvates) using thermogravimetric analyses (TGA, DSC) and ATR-FT-IR spectroscopy. The results of these analyses will be reported elsewhere.

Each cocrystal (150 mg) was later subjected to LAG for 60 min (at 30 Hz) using nitromethane (η=0.30 µL mg^{-1}), 2-pyrrolidone (η=0.30 µL mg^{-1}) or DMSO (η=0.30 µL mg^{-1}) as liquid additives. Figure S38

show the PXRD patterns of the resulting solids in the case of (**thp**)·(**23diFBA**), which are all consistent with a partial or full decomposition of the cocrystals into a physical mixture of the cocrystal constituents. Figure S39, on the other hand, shows that the decomposition of the (**thp**)·(**26diFBA**) cocrystal occurred only two out of three cases; that is, in the presence of 2-pyrrolidone and dimethyl sulfoxide. The (**thp**)·(**26diFBA**) appears to be unaffected by LAG in the presence of nitromethane.

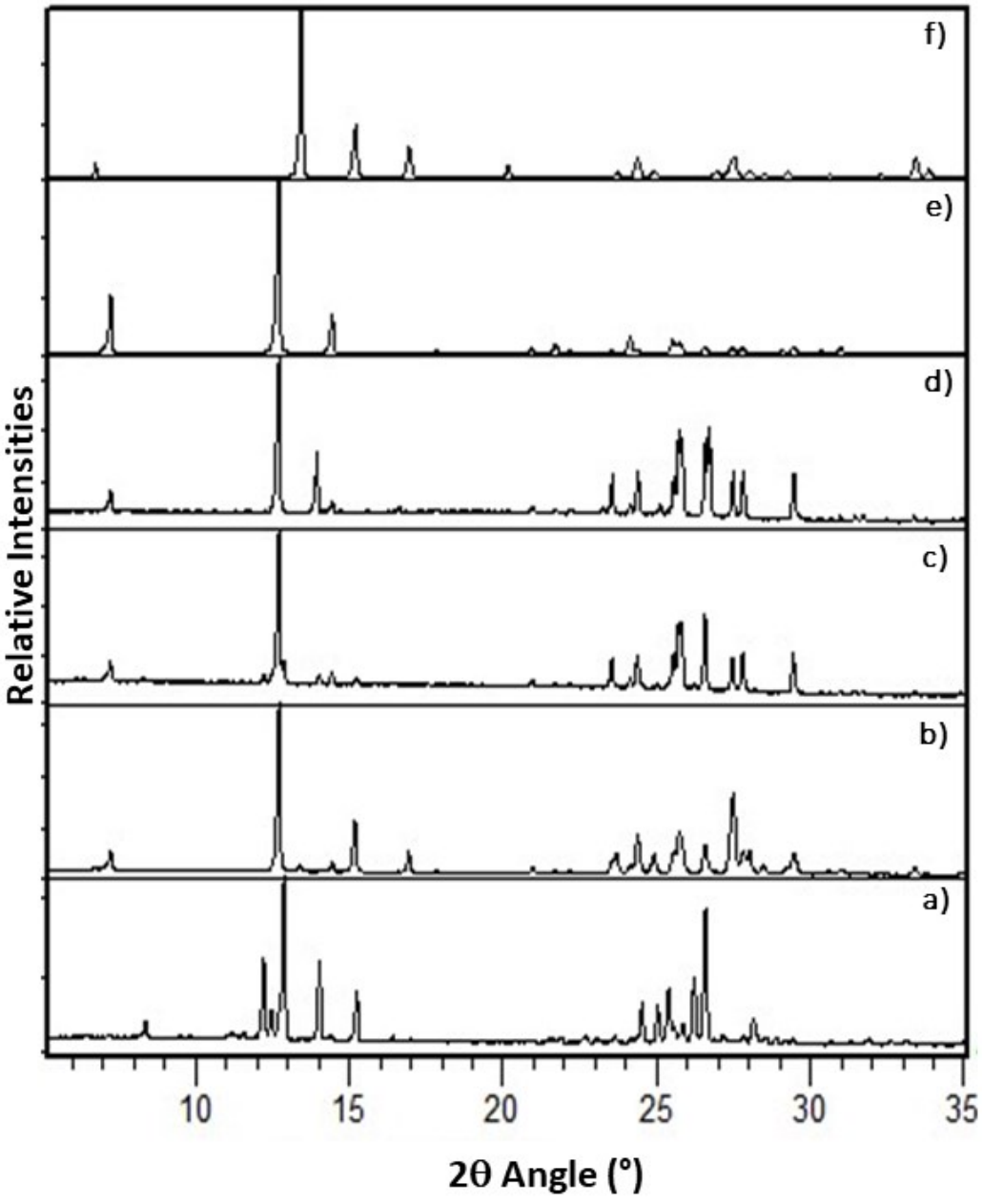

Figure S38. PXRD pattern of: (a) (**thp**)·(**23diFBA**) cocrystal as synthesised, (b), (c), (d) (**thp**)·(**23diFBA**) cocrystal subjected to LAG (η=0.30 µL mg^{-1}) in the presence of nitromethane, 2-pyrrolidone and dimethyl sulfoxide, respectively, (e) **thp** pure and (f) **23diFBA** pure.

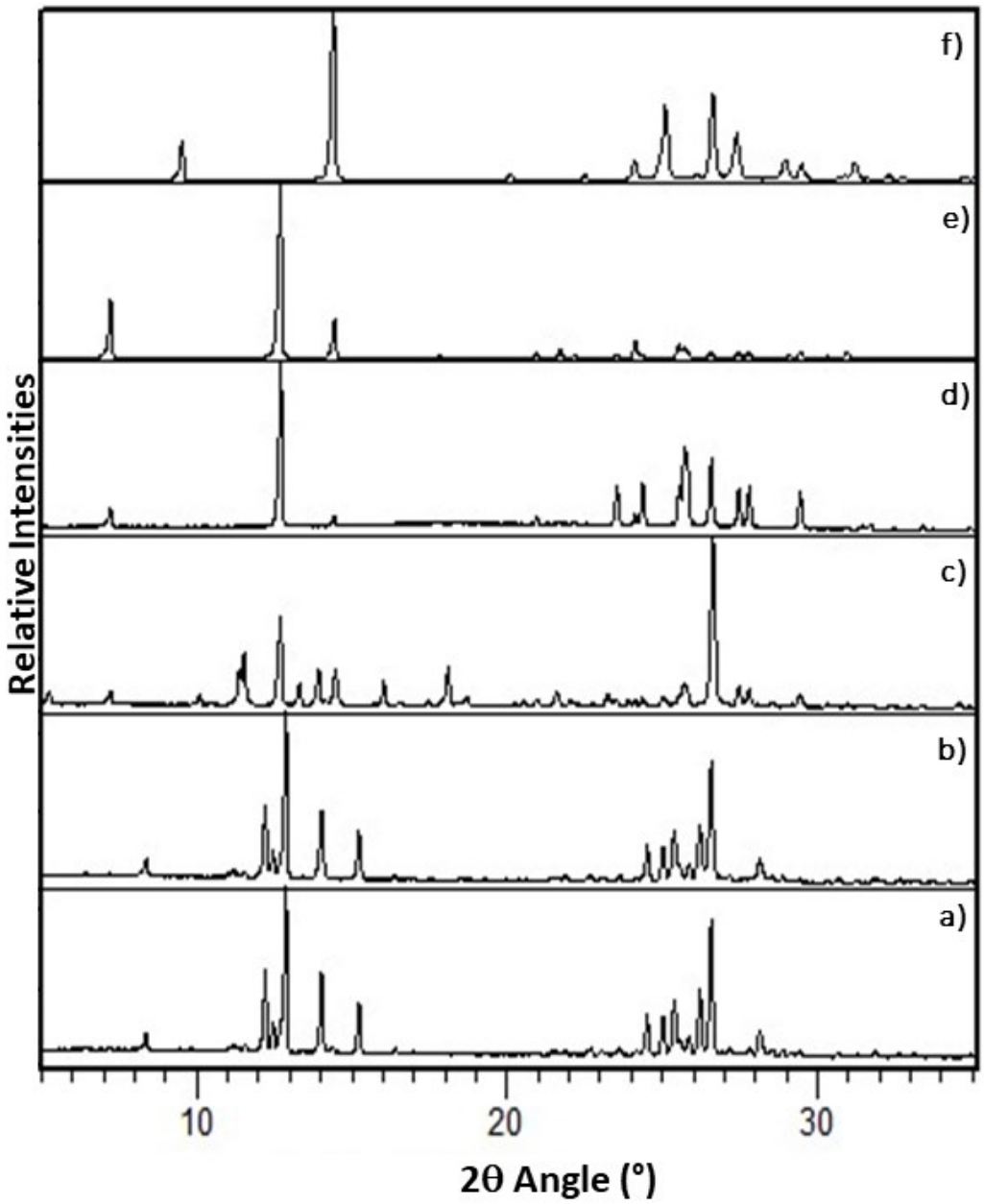

Figure S39. PXRD pattern of: (a) (**thp**)·(**26diFBA**) cocrystal, (b), (c), (d) (**thp**)·(**26diFBA**) cocrystal processed through LAG (η=0.30 µL mg^{-1}) using nitromethane, 2-pyrrolidone and dimethyl sulfoxide, respectively, (e) **thp** pure and (f) **26diFBA** pure.

8.2 Theophylline:anthranilic acid cocrystal

Fischer and co-authors reported that cocrystals of theophylline (**thp**) and anthranilic acid (**ana**) in 2:3 molar ratio (CSD code WUTHEA) can be obtained by LAG with ethanol using a *MM400 Retsch* ball mill.[22] In the present study, (**thp**)$_2$·(**ana**)$_3$ cocrystals were obtained mechanochemically through LAG with ethanol. Specifically, 93.4 mg of **thp** and 106.6 mg of **ana** were added to a 15 mL steel jar containing two milling balls of 7 mm diameter. The mixture was subsequently milled in the presence of ethanol (η=0.30 µL mg^{-1}) for 60 min at a frequency of 25 Hz. Snap-closed grinding jars (*FormTech*

Scientific) were used to minimise liquid evaporation. Such procedure was repeated four times. The purity of synthesised cocrystal was verified by Rietveld analysis (Figure S40).

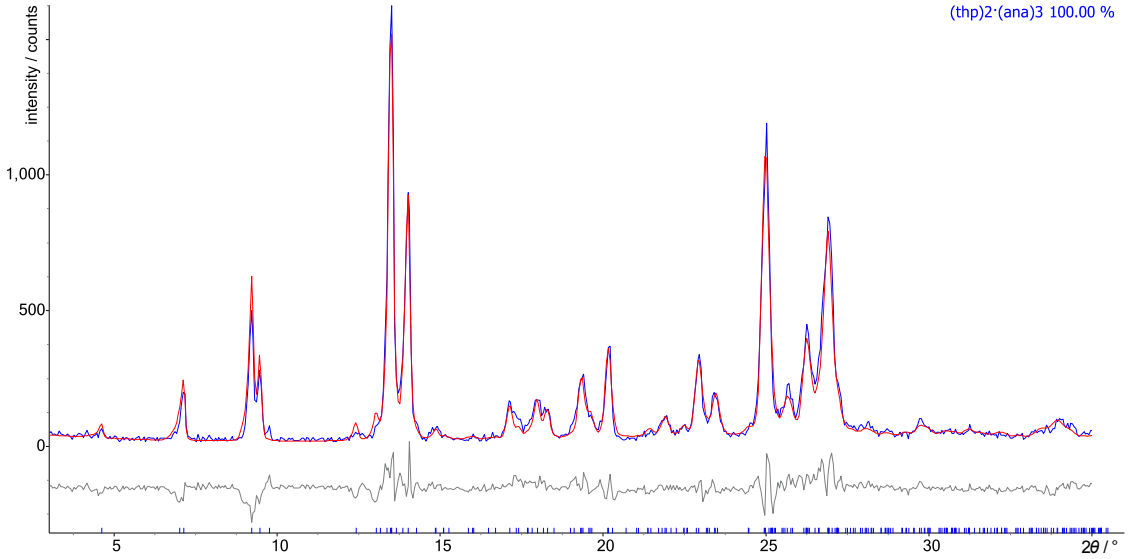

Figure S40. Rietveld refinement plot of (**thp**)$_2$·(**ana**)$_3$ prepared by LAG with ethanol (η=0.30 µL mg^{-1}). The calculated profile is shown in red, the experimental profile is shown in blue, and the difference curve is shown in grey.

Three samples of the synthesised (**thp**)$_2$·(**ana**)$_3$ cocrystal (~150 mg) were separately treated for 60 min at 25 Hz under LAG using nitromethane (η=0.30 µL mg^{-1}), 2-pyrrolidone (η=0.30 µL mg^{-1}) or DMSO (η=0.30 µL mg^{-1}) as liquid additives. The LAG products were characterised using PXRD (Figure S41) and each of the powder patterns was analyzed using the Rietveld refinement technique. The analyses revealed that LAG with nitromethane does not cause any significant changes to the (**thp**)$_2$·(**ana**)$_3$ cocrystal (Figures S42), while LAG with 2-pyrrolidone and DMSO caused partial dissociation of the cocrystal (Figure S43 and S44).

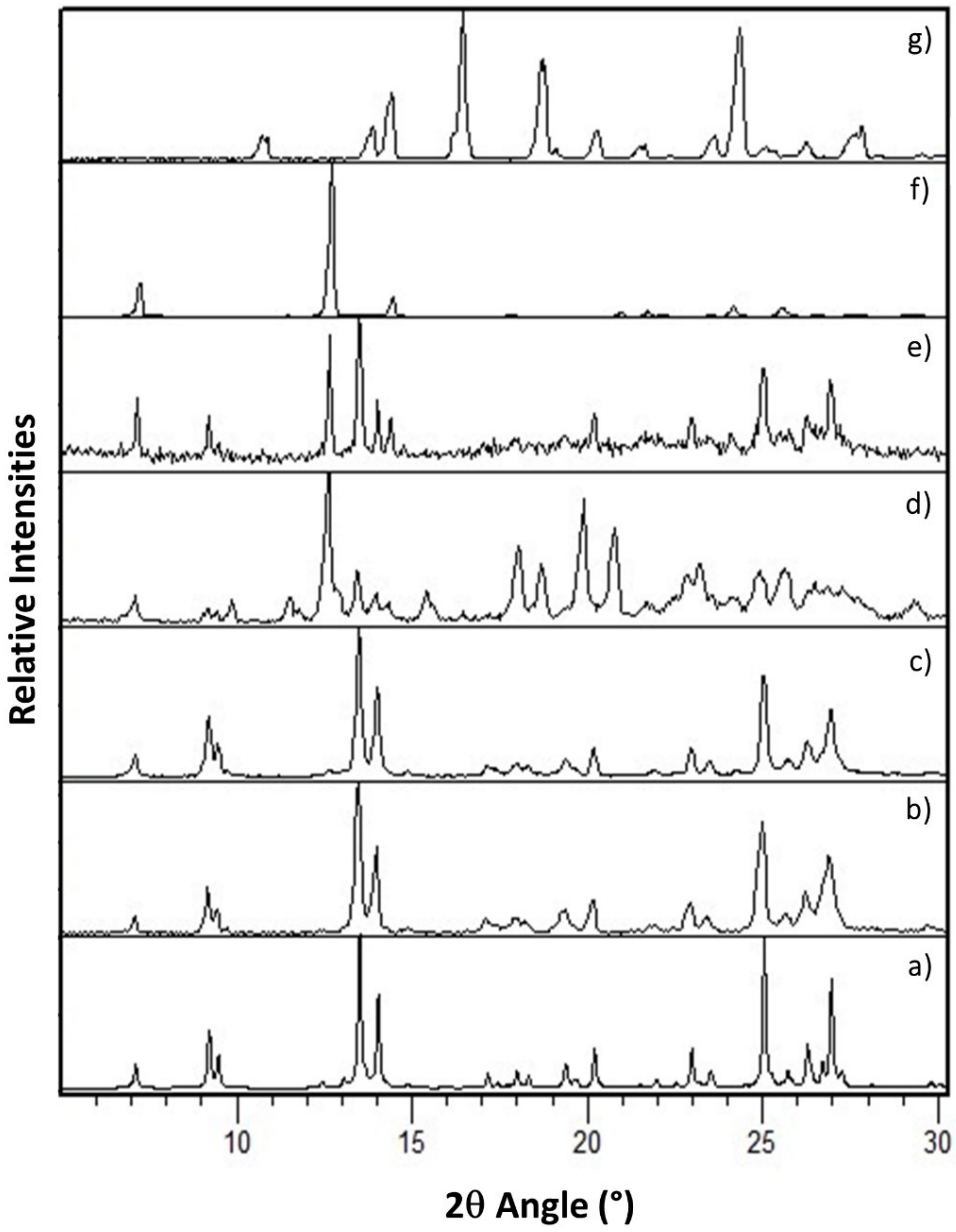

Figure S41. PXRD pattern of: (a) calculated (**thp**)$_2$·(**ana**)$_3$, (b) (**thp**)$_2$·(**ana**)$_3$ prepared by LAG with ethanol (η=0.30 µL mg^{-1}), (c), (d), (e) preformed (**thp**)$_2$·(**ana**)$_3$ processed by LAG (η=0.30 µL mg^{-1}) using nitromethane, 2-pyrrolidone and DMSO, respectively, (f) pure **theo** and (g) pure **ana**.

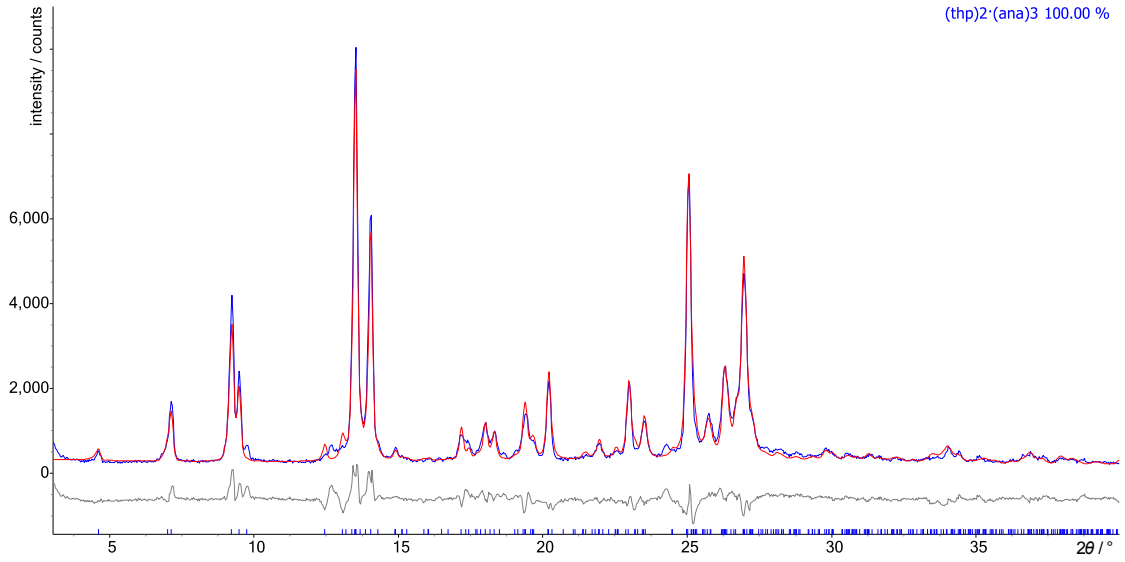

Figure S42. Rietveld refinement plot of (**thp**)$_2$·(**ana**)$_3$ processed by LAG (η=0.30 µL mg^{-1}) with nitromethane. The calculated profile is shown in red, the experimental profile is shown in blue, and the difference curve is shown in grey.

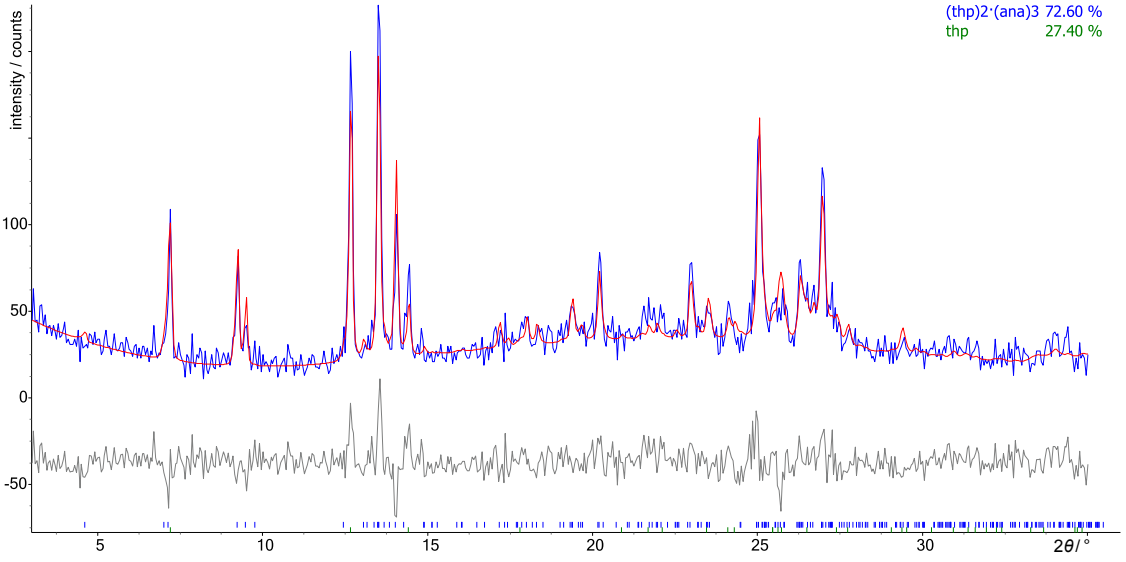

Figure S43. Rietveld refinement plot of (**thp**)$_2$·(**ana**)$_3$ processed by LAG (η=0.30 µL mg^{-1}) with DMSO. The calculated profile is shown in red, the experimental profile is shown in blue, and the difference curve is shown in grey.

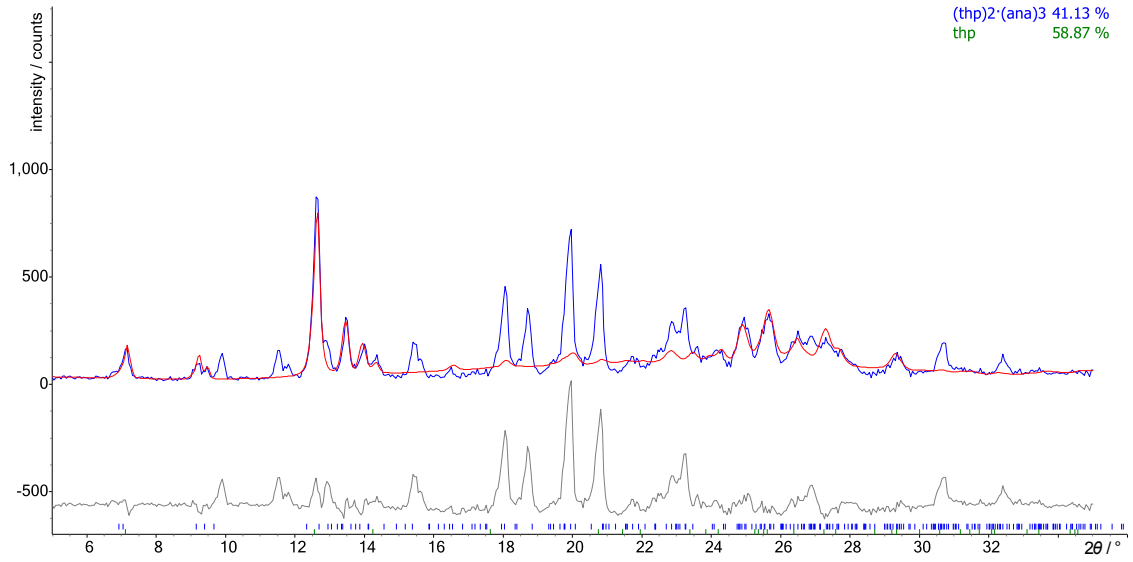

Figure S44. Rietveld refinement plot of (**thp**)$_2$·(**ana**)$_3$ processed by LAG (η=0.30 µL mg^{-1}) with 2-pyrrolidone. The calculated profile is shown in red, the experimental profile is shown in blue, and the difference curve is shown in grey. This experiment has resulted in the formation of a new phase with an unknown crystal structure. Due to the lack of a suitable crystal structure, the peaks corresponding to the new phase could not be modelled during Rietveld refinement.

8.3 Ibuprofen:nicotinamide cocrystal

Berry *et al.* reported the formation of a 1:1 cocrystal of racemic ibuprofen (**ibu**) and nicotinamide (**nic**) (CSD code SODDIZ) can be obtained from solutions via slow solvent evaporation.[23] In this study, racemic (**ibu**)·(**nic**) cocrystals were obtained mechanochemically by LAG with ethanol. Specifically, 125.7 mg of **ibu** and 74.3 mg of **nic** were added to a 15 mL steel jar containing two milling balls of 7 mm diameter. The mixture was subsequently milled in the presence of ethanol (η=0.30 µL mg^{-1}) for 60 min (at 25 Hz). The purity of the product was confirmed by Rietveld refinements (Figure S45).

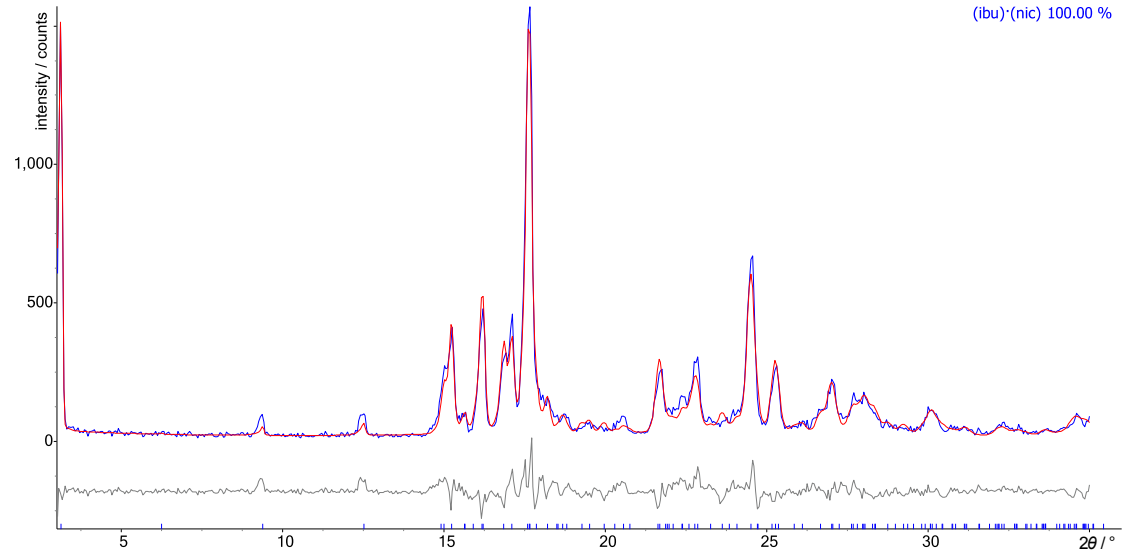

Figure S45. Rietveld refinement plot of (**ibu**)·(**nic**) prepared by LAG with ethanol (η=0.30 µL mg^{-1}). The calculated profile is shown in red, the experimental profile is shown in blue, and the difference curve is shown in grey.

Three samples of the (**ibu**)·(**nic**) cocrystal (~150 mg) were separately treated for 60 min at 25 Hz under LAG using nitromethane (η=0.30 µL mg^{-1}), 2-pyrrolidone (η=0.30 µL mg^{-1}) or DMSO (η=0.30 µL mg^{-1}) as liquid additives (Figure S46).

Approximately 150 mg of the synthesised (**ibu**)·(**nic**) cocrystal were then separately treated for 60 min at 25 Hz using LAG with nitromethane (η=0.30 µL mg^{-1}), 2-pyrrolidone (η=0.30 µL mg^{-1}) or DMSO (η=0.30 µL mg^{-1}) as liquid additives. The products were characterised using PXRD and the obtained powder patterns were analyzed using the Rietveld refinement technique. These analyses that the use of the three liquid additives did not cause any meaningful changes to the structure of the solids (Figures S47-S49).

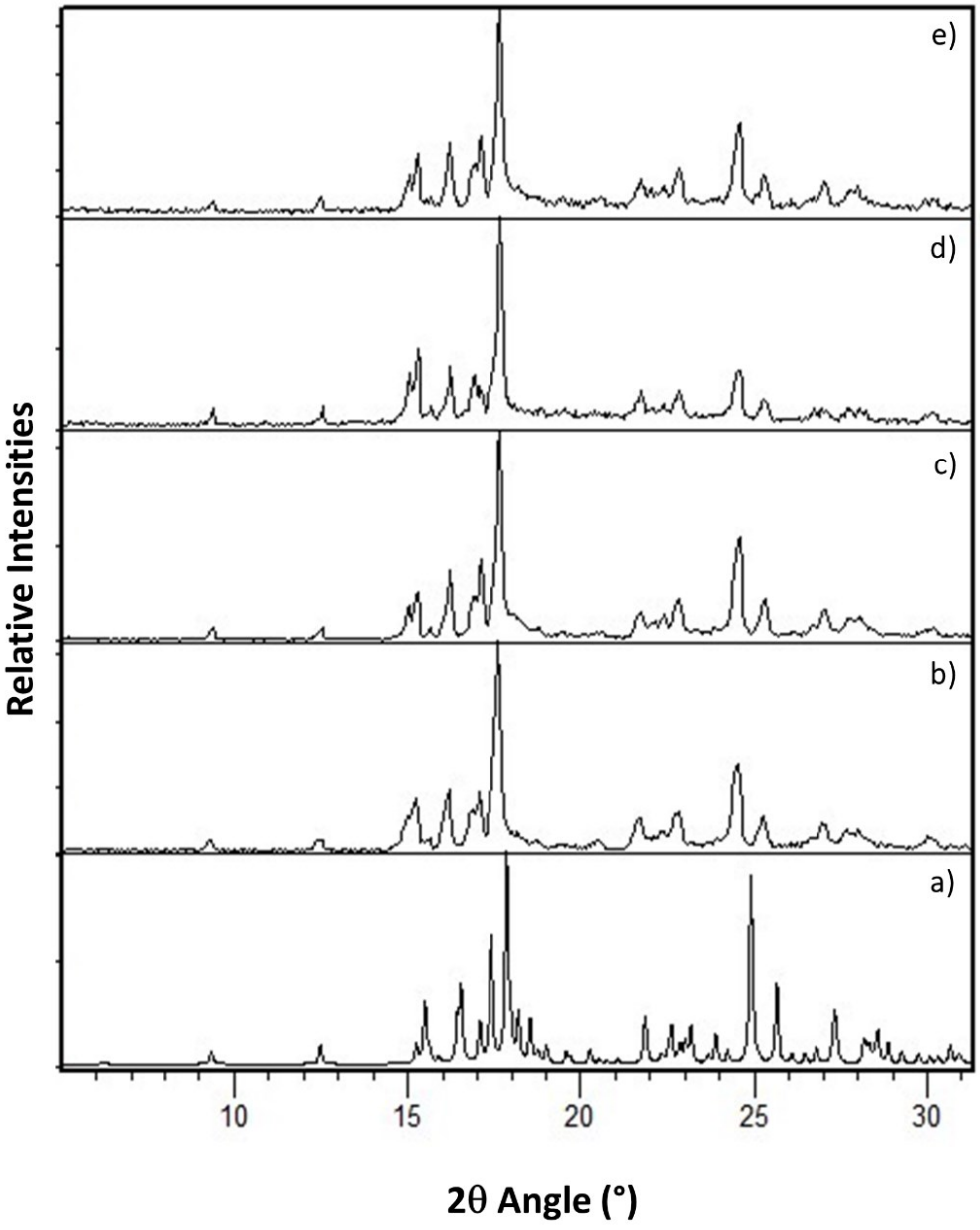

Figure S46. PXRD pattern of: (a) calculated (**ibu**)·(**nic**),[23] (b) (**ibu**)·(**nic**) prepared by LAG with ethanol (η=0.30 µL mg^{-1}), (c), (d), (e) preformed (**ibu**)·(**nic**) processed by LAG (η=0.30 µL mg^{-1}) using nitromethane, 2-pyrrolidone and DMSO, respectively.

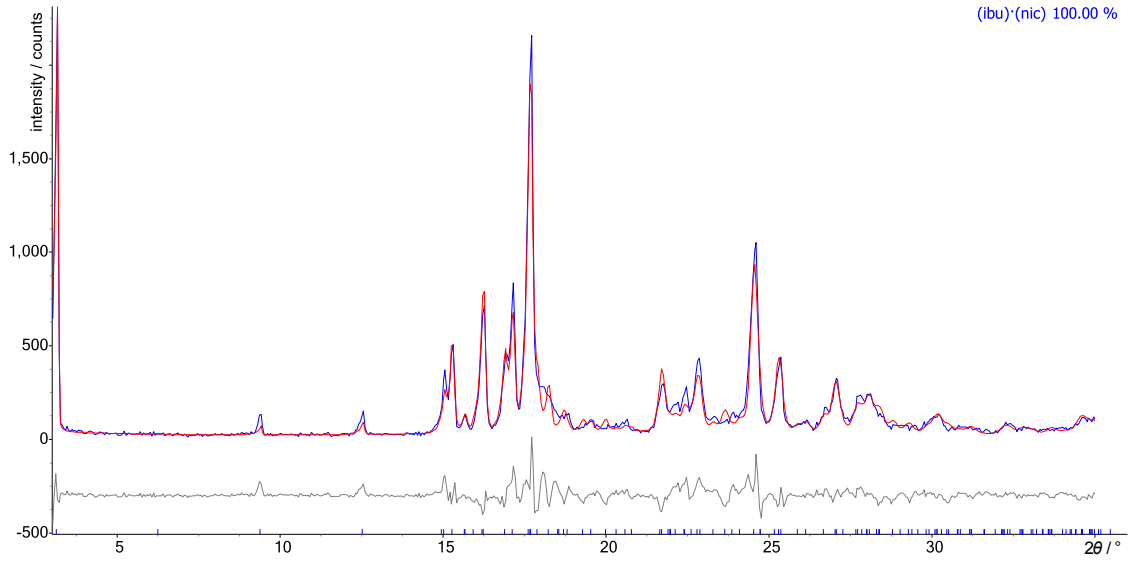

Figure S47. Rietveld refinement plot of (**ibu**)·(**nic**) processed by LAG (η=0.30 µL mg^{-1}) with nitromethane. The calculated profile is shown in red, the experimental profile is shown in blue, and the difference curve is shown in grey.

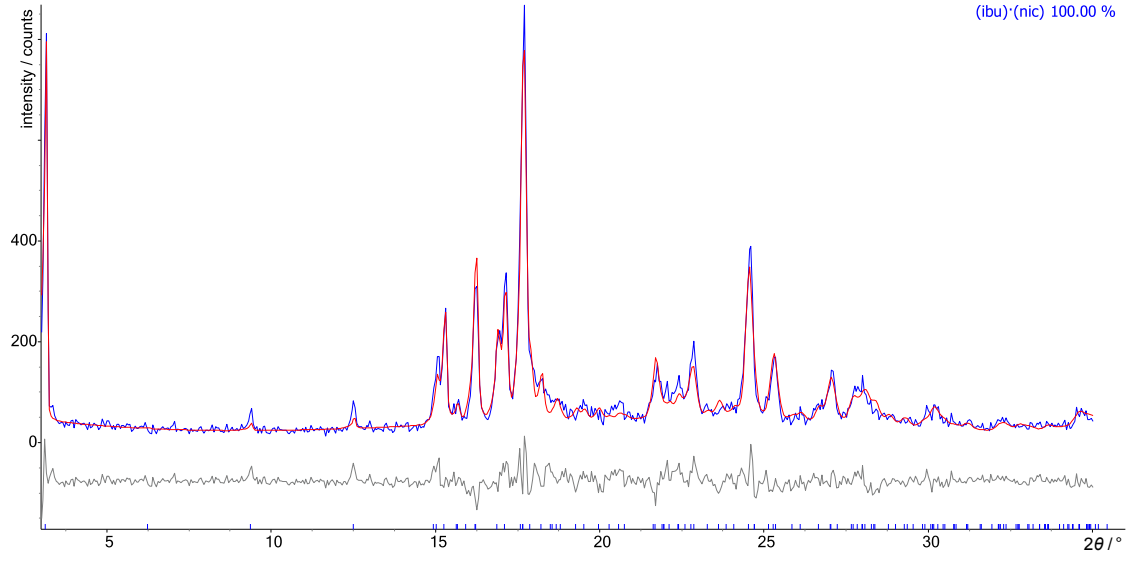

Figure S48. Rietveld refinement plot of (**ibu**)·(**nic**) processed by LAG (η=0.30 µL mg^{-1}) with DMSO. The calculated profile is shown in red, the experimental profile is shown in blue, and the difference curve is shown in grey.

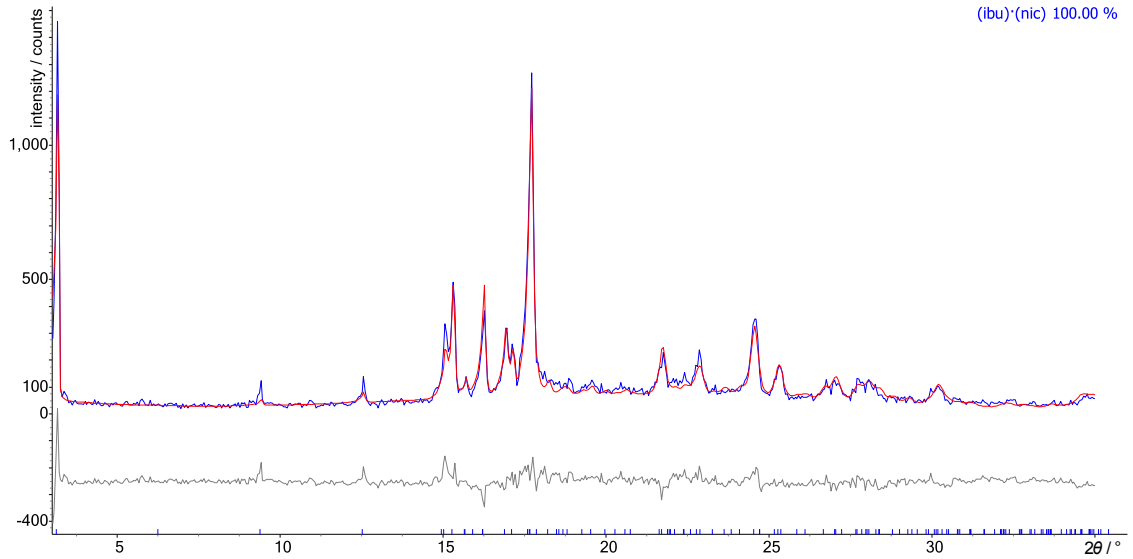

Figure S49. Rietveld refinement plot of (**ibu**)·(**nic**) processed by LAG (η=0.30 µL mg^{-1}) with 2-pyrrolidone. The calculated profile is shown in red, the experimental profile is shown in blue, and the difference curve is shown in grey.

8.4 Paracetamol:oxalic acid cocrystal

The 1:1 (**par**)·(**oxa**) cocrystal (CSD code LUJTAM) was prepared mechanochemically using a method reported by Karki *et al.*.[24] Specifically, 125.4 mg of **par** and 74.6 mg of H_2**oxa** were added to a 15 mL steel jar containing two milling balls of 7 mm diameter. The mixture was subsequently milled under in the presence of methanol (η=0.30 µL mg^{-1}) for 60 min (at 25 Hz). The purity of synthesized was evaluated by PXRD and Rietveld refinements (Figure S50).

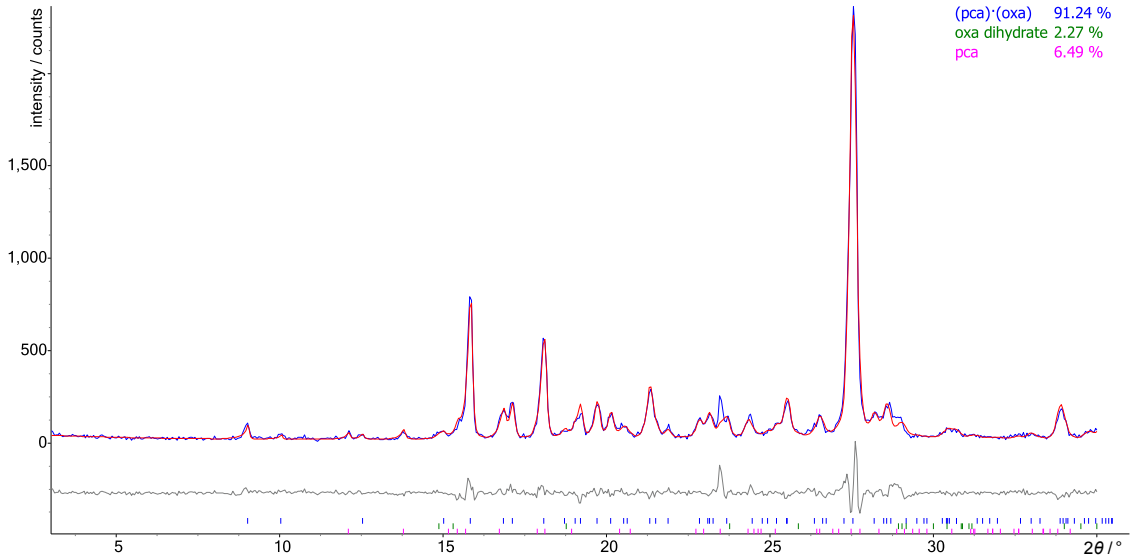

Figure S50. Rietveld refinement plot of (**par**)·(**oxa**) prepared by LAG with methanol (η=0.30 µL mg^{-1}). The calculated profile is shown in red, the experimental profile is shown in blue, and the difference curve is shown in grey.

Approximately 150 mg of the synthesised (**par**)·(**oxa**) cocrystal were then separately ground for 60 min at 25 Hz using nitromethane (η=0.30 µL mg^{-1}), 2-pyrrolidone (η=0.30 µL mg^{-1}) or DMSO (η=0.30 µL mg^{-1}) as liquid additives. The products were characterised by PXRD (Figure S51) and the obtained powder patterns were analyzed using the Rietveld refinement technique. The analyses revealed that LAG with nitromethane did not cause any changes to (**par**)·(**oxa** (Figures S52), while LAG with 2-pyrrolidone and DMSO caused partial dissociation of the cocrystal (Figure S53 and S54).

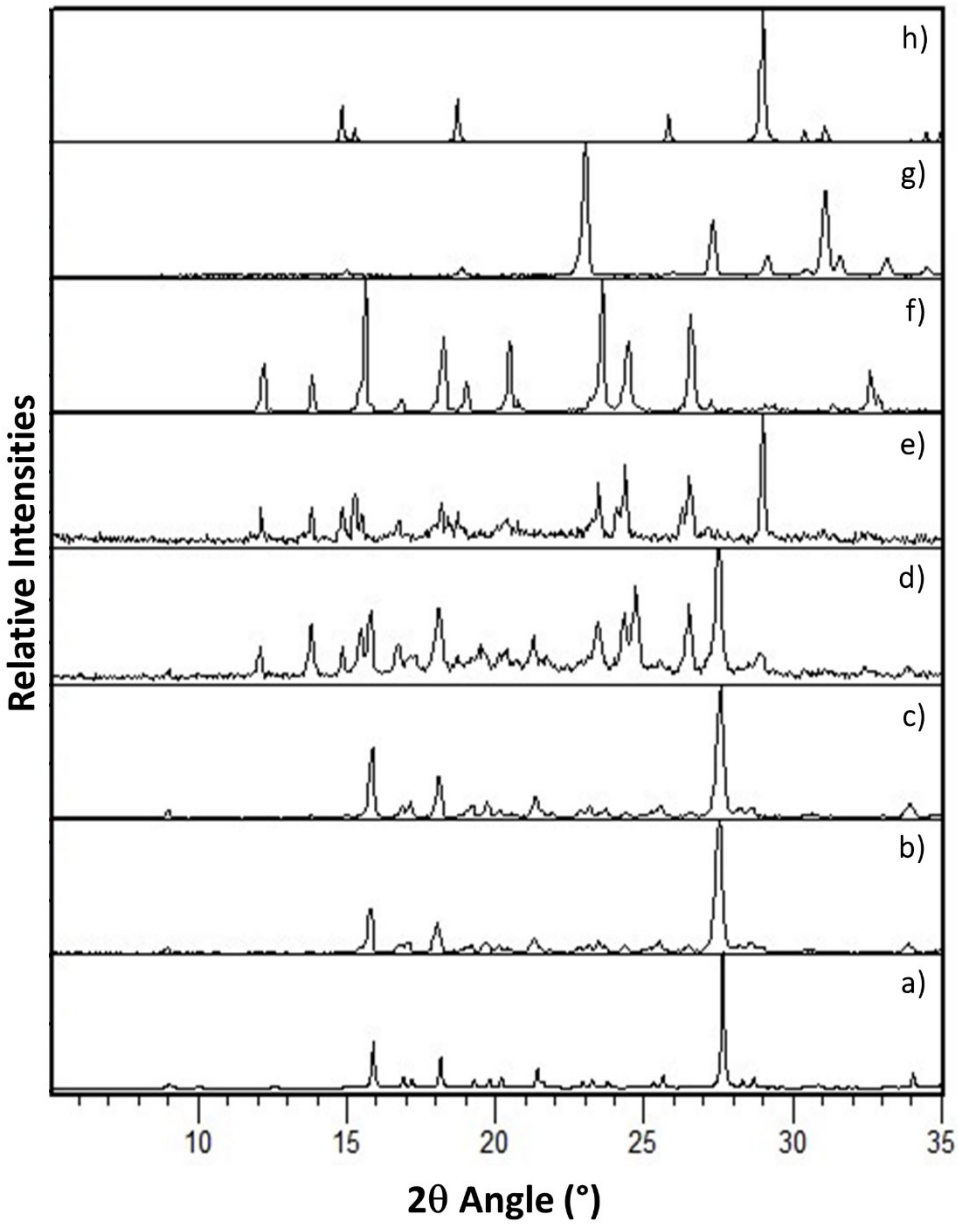

Figure S51. PXRD pattern of: (a) calculated (**par**)·(**oxa**),[24] (b) (**par**)·(**oxa**) prepared by LAG with methanol (η=0.30 µL mg^{-1}), (c), (d), (e) preformed (**par**)·(**oxa**) processed by LAG (η=0.30 µL mg^{-1}) using nitromethane, 2-pyrrolidone and DMSO, respectively, (f) pure **par,** (g) pure H_2**oxa** and (h) calculated H_2**oxa** dehydrate (CSD code: OXACDH04[26]).

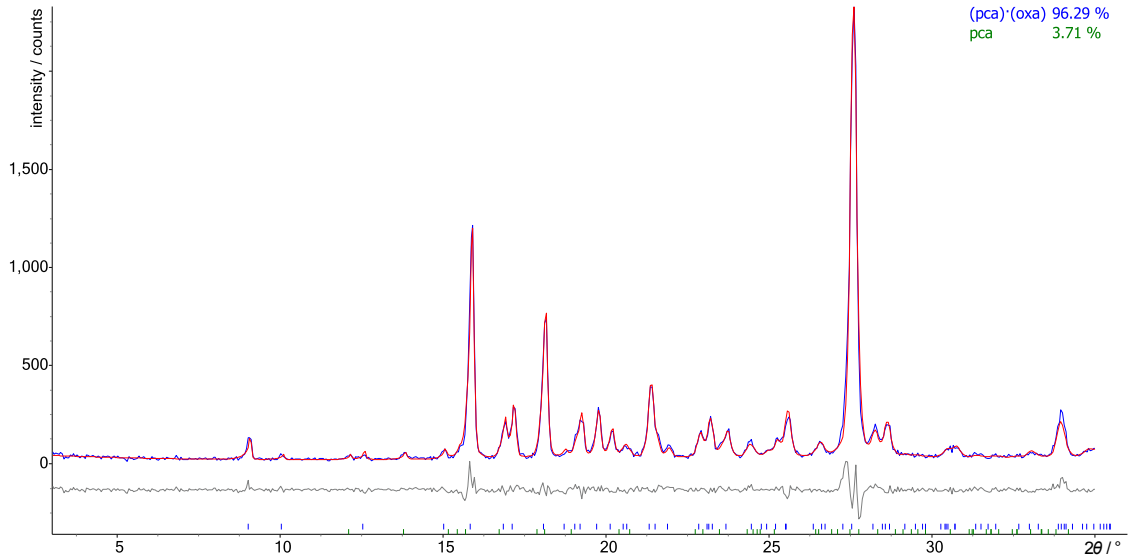

Figure S52. Rietveld refinement plot of (**par**)·(**oxa**) processed by LAG (η=0.30 µL mg^{-1}) with nitromethane. The calculated profile is shown in red, the experimental profile is shown in blue, and the difference curve is shown in grey.

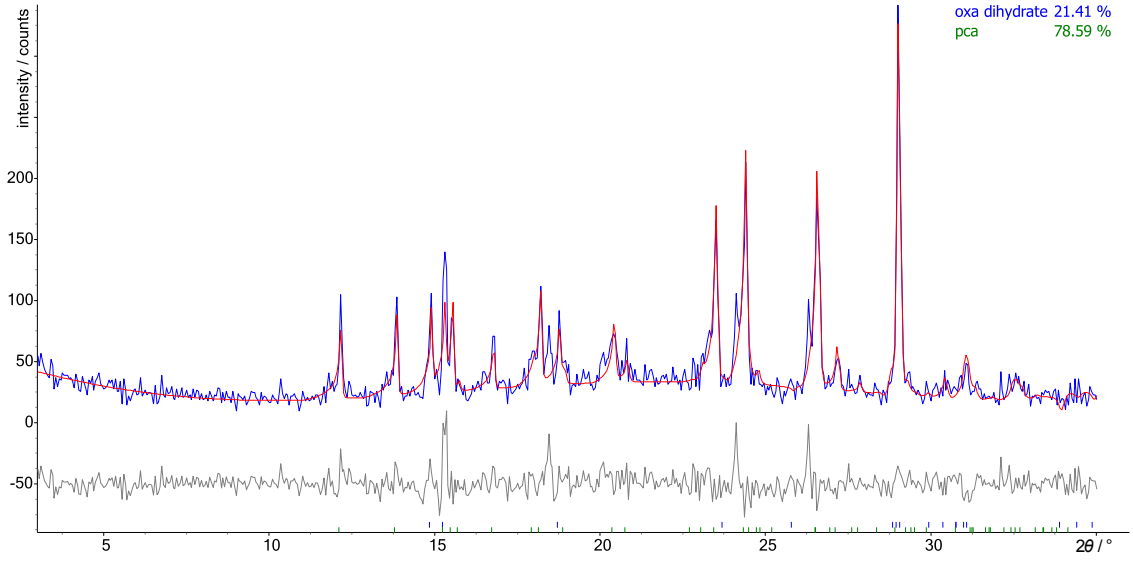

Figure S53. Rietveld refinement plot of (**par**)·(**oxa**) processed by LAG (η=0.30 µL mg^{-1}) with DMSO. The calculated profile is shown in red, the experimental profile is shown in blue, and the difference curve is shown in grey.

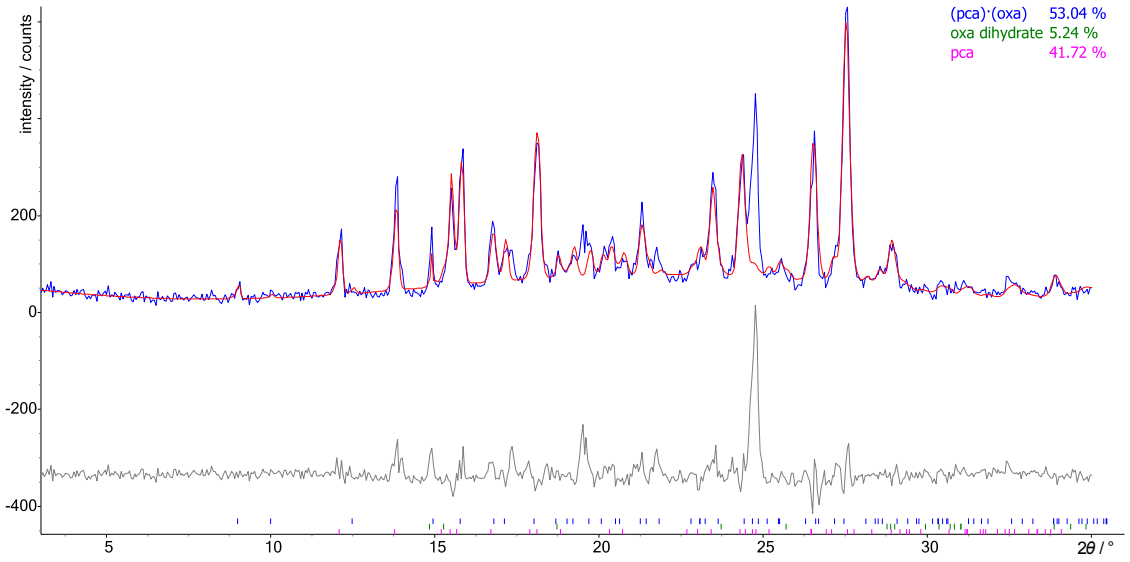

Figure S54. Rietveld refinement plot of (**par**)·(**oxa**) processed by LAG (η=0.30 µL mg^{-1}) with 2-pyrrolidone. The calculated profile is shown in red, the experimental profile is shown in blue, and the difference curve is shown in grey. LAG resulted in the formation of a new phase with an unknown crystal structure and its corresponding peaks could not be modelled during Rietveld refinement.

8.5 Caffeine:p-coumaric acid cocrystal

The 1:1 (**caf**)·(**cou**) cocrystal, initially reported by Schultheiss *et al.* (CSD code IJEZUT),[25] was prepared mechanochemically. Specifically, 108.4 mg of **caf** and 91.6 mg of **cou** were added to a 15 mL snap-closed grinding jar (*FormTech Scientific*) containing two milling balls of 7 mm diameter. The mixture was milled in the presence of acetonitrile (η=0.30 µL mg^{-1}) for 60 min at (at 25 Hz). Such procedure was repeated four times. Their purity of the was verified by PXRD (Figure S56).

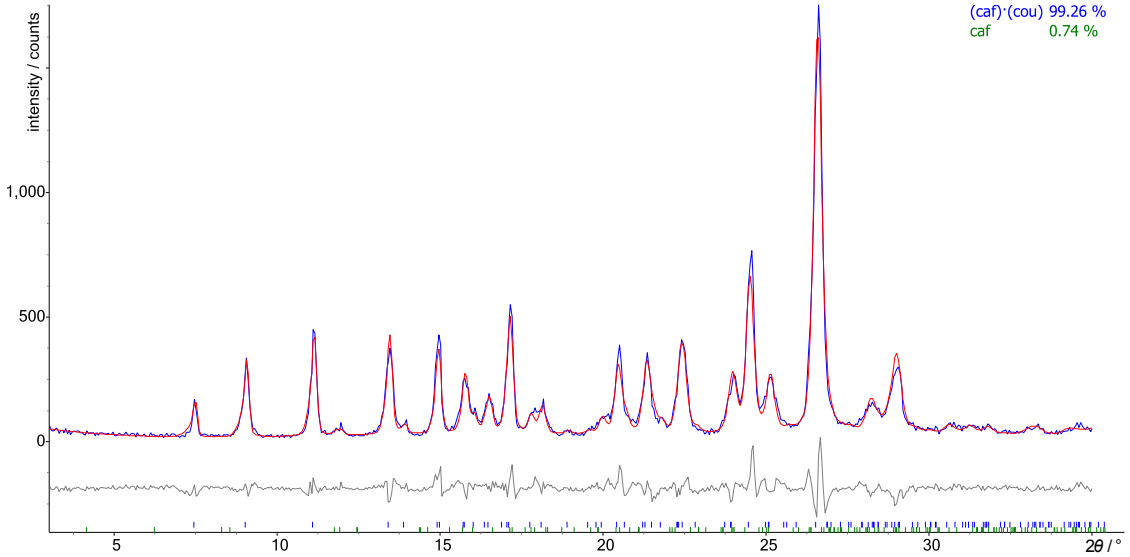

Figure S55. Rietveld refinement plot of (**caf**)·(**cou**) prepared by LAG with methanol (η=0.30 µL mg^{-1}). The calculated profile is shown in red, the experimental profile is shown in blue, and the difference curve is shown in grey.

Three batches of (**caf**)·(**cou**) (~150 mg each) were separately treated for 60 min at 25 Hz under LAG conditions using nitromethane (η=0.30 µL mg^{-1}), DMSO (η=0.30 µL mg^{-1}) and 2-pyrrolidone (η=0.30 µL mg^{-1}) as liquid additives. The products were characterised using PXRD (Figure S57) and the resulting powder patterns were analyzed using the Rietveld refinement method to show that the use of all three liquid additives has not resulted in any meaningful structural changes (Figures S58-S60).

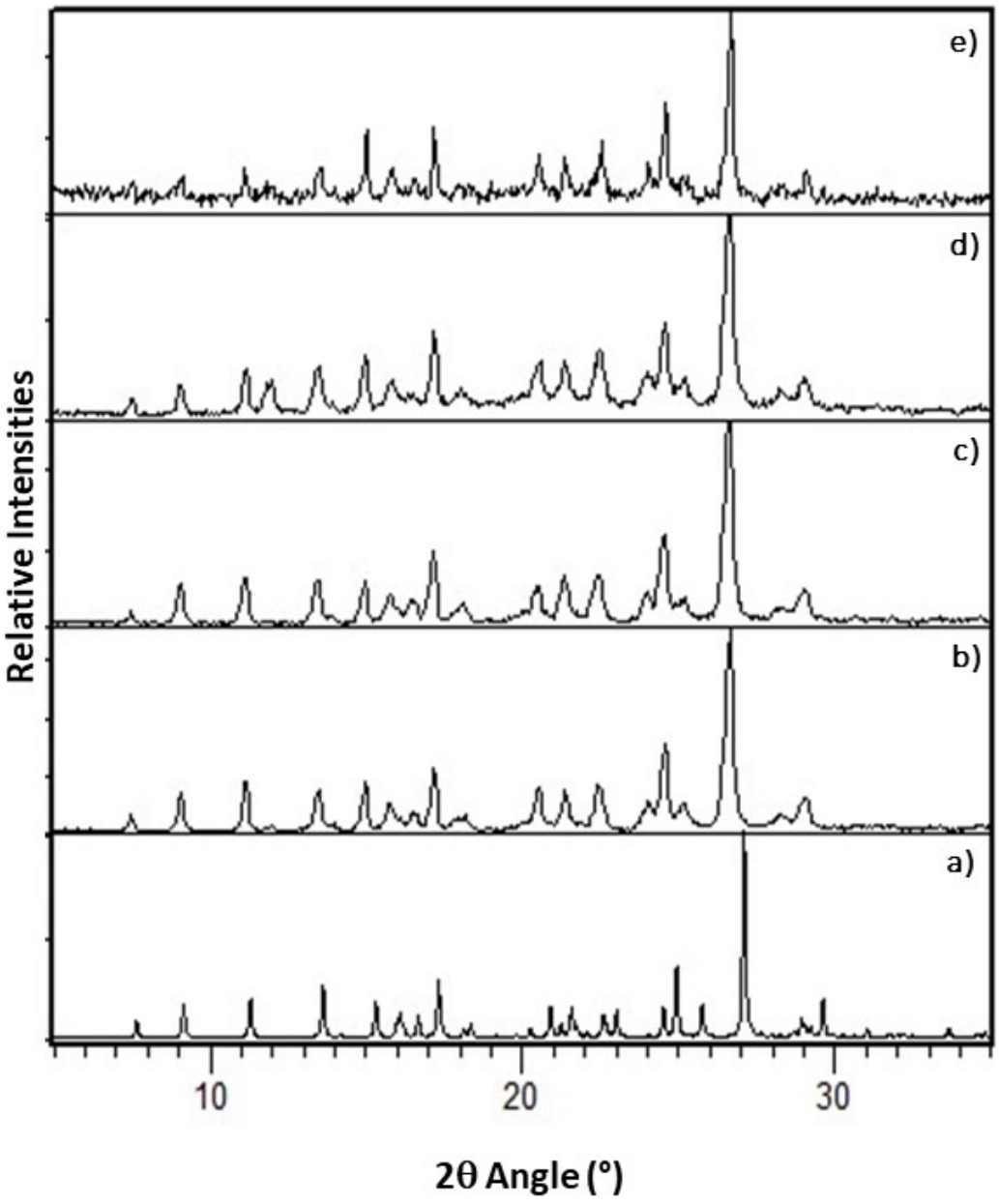

Figure S56. PXRD pattern of: (a) calculated (**caf**)·(**cou**),[25] (b) (**caf**)·(**cou**) prepared by LAG with methanol (η=0.30 µL mg^{-1}), (c), (d) and (e) preformed (**caf**)·(**cou**) processed by LAG (η=0.30 µL mg^{-1}) using nitromethane, 2-pyrrolidone and DMSO, respectively.

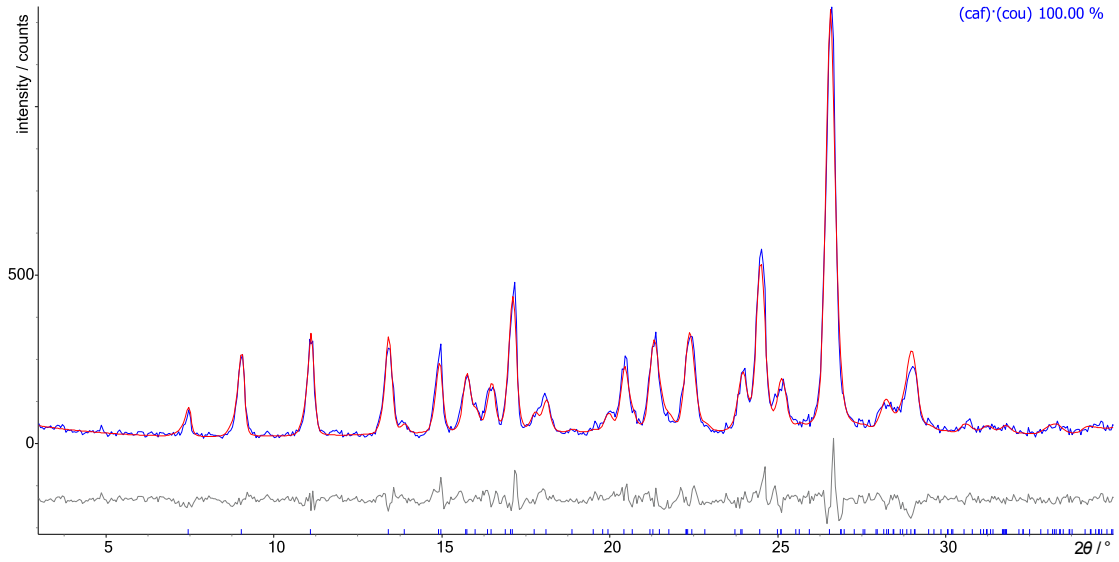

Figure S57. Rietveld refinement plot of (**caf**)·(**cou**) processed by LAG (η=0.30 µL mg^{-1}) with nitromethane. The calculated profile is shown in red, the experimental profile is shown in blue, and the difference curve is shown in grey.

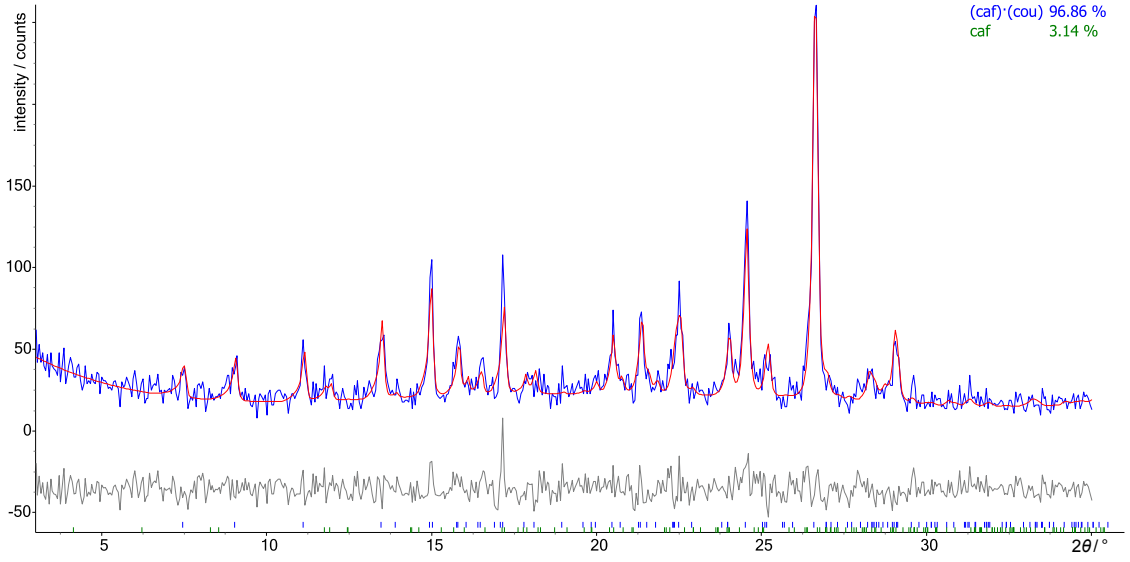

Figure S58. Rietveld refinement plot of (**caf**)·(**cou**) processed by LAG (η=0.30 µL mg^{-1}) with DMSO. The calculated profile is shown in red, the experimental profile is shown in blue, and the difference curve is shown in grey.

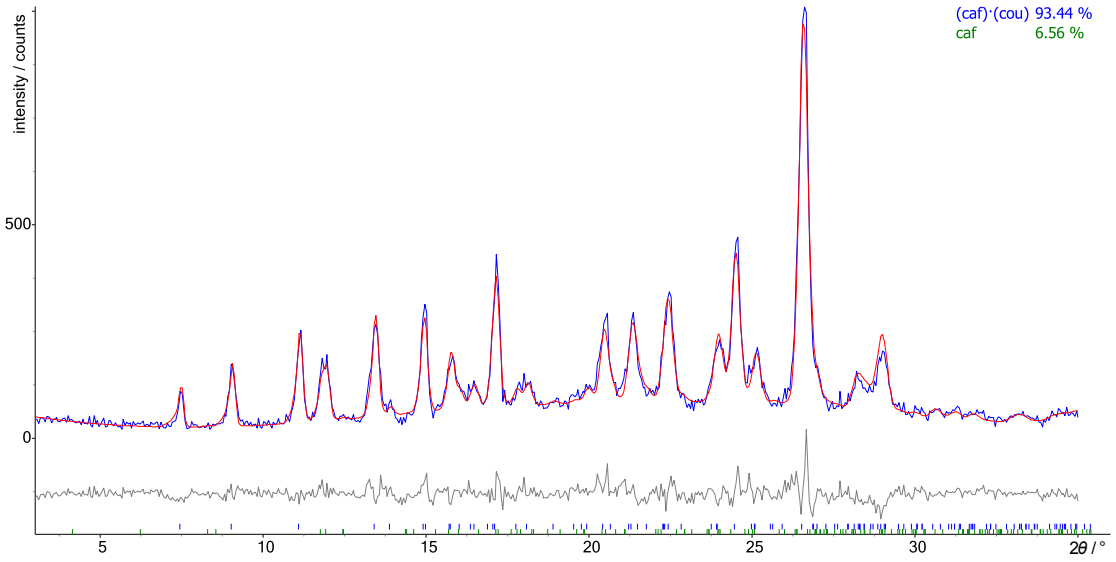

Figure S59. Rietveld refinement plot of (**caf**)·(**cou**) processed by LAG (η=0.30 µL mg^{-1}) with 2-pyrrolidone. The calculated profile is shown in red, the experimental profile is shown in blue, and the difference curve is shown in grey.

9. References

(1) A. Altomare, C. Giacovazzo, A. Guagliardi, A. G. G. Moliterni, R. Rizzi, P.-E. Werner, New Techniques for Indexing: N-TREOR in EXPO. *J. Appl. Crystallogr.,* 2000, **33**, 1180–1186.

(2) A. Altomare, C. Cuocci, C. Giacovazzo, A. Moliterni, R. Rizzi, N. Corriero, A. Falcicchio, EXPO2013 : A Kit of Tools for Phasing Crystal Structures from Powder Data. *J. Appl. Crystallogr.,* 2013, **46**, 1231–1235.

(3) A. A. Coelho, TOPAS and TOPAS-Academic : An Optimization Program Integrating Computer Algebra and Crystallographic Objects Written in C++. *J. Appl. Crystallogr.,* 2018, **51**, 210–218.

(4) CrysAlisPro, Agilent Technologies, Version 1.171.37.34 (release 22-05-2014 CrysAlis171 .NET).

(5) O. V. Dolomanov, L. J. Bourhis, R. J. Gildea, J. A. K. Howard, H. Puschmann, OLEX2 : A Complete Structure Solution, Refinement and Analysis Program. *J. Appl. Crystallogr.,* 2009, **42**, 339–341.

(6) C. B. Hübschle, G. M. Sheldrick, B. Dittrich, ShelXle : A Qt Graphical User Interface for SHELXL. *J. Appl. Crystallogr.,* 2011, **44**, 1281–1284.

(7) G. M. Sheldrick, SHELXT – Integrated Space-Group and Crystal-Structure Determination. *Acta Crystallogr. A*, 2015, **71**, 3–8.

(8) G. M. Sheldrick, Crystal Structure Refinement with SHELXL. *Acta Crystallogr.,* 2015, **71**, 3–8.

(9) S. J. Clark, M. D. Segall, C. J. Pickard, P. J. Hasnip, M. I. J. Probert, K. Refson, M. C. Payne, First Principles Methods Using CASTEP. *Z. Kristallogr. Cryst. Mater.,* 2005, **220**, 5–6.

(10) T. Björkman, CIF2Cell: Generating Geometries for Electronic Structure Programs. *Comput. Phys. Commun.,* 2011, **182**, 1183–1186.

(11) J. P. Perdew, K. Burke, M. Ernzerhof, Generalized Gradient Approximation Made Simple. *Phys.*

Rev. Lett., 1996, **77** , 3865–3868.

(12) N. V. Tkachenko, H. Lemmetyinen, J. Sonoda, K. Ohkubo, T. Sato, H. Imahori, S. Fukuzumi, Ultrafast Photodynamics of Exciplex Formation and Photoinduced Electron Transfer in Porphyrin−Fullerene Dyads Linked at Close Proximity. *J. Phys. Chem. A,* 2003, **107** , 8834–8844.

(13) A. Ambrosetti, A. M. Reilly, R. A. DiStasio, A. Tkatchenko, Long-Range Correlation Energy Calculated from Coupled Atomic Response Functions. *J. Chem. Phys.,* 2014, **140**, 18A508.

(14) A. M. Reilly, A. Tkatchenko, Van Der Waals Dispersion Interactions in Molecular Materials: Beyond Pairwise Additivity. *Chem. Sci.,* 2015, **6**, 3289–3301.

(15) *Gaussian 16*, Revision B.01, M. J. Frisch, G. W. Trucks, H. B. Schlegel, G. E. Scuseria, M. A. Robb, J. R. Cheeseman, G. Scalmani, V. Barone, G. A. Petersson, H. Nakatsuji, X. Li, M. Caricato, A. V. Marenich, J. Bloino, B. G. Janesko, R. Gomperts, B. Mennucci, H. P. Hratchian, J. V. Ortiz, A. F. Izmaylov, J. L. Sonnenberg, D. Williams-Young, F. Ding, F. Lipparini, F. Egidi, J. Goings, B. Peng, A. Petrone, T. Henderson, D. Ranasinghe, V. G. Zakrzewski, J. Gao, N. Rega, G. Zheng, W. Liang, M. Hada, M. Ehara, K. Toyota, R. Fukuda, J. Hasegawa, M. Ishida, T. Nakajima, Y. Honda, O. Kitao, H. Nakai, T. Vreven, K. Throssell, J. A. Montgomery, Jr., J. E. Peralta, F. Ogliaro, M. J. Bearpark, J. J. Heyd, E. N. Brothers, K. N. Kudin, V. N. Staroverov, T. A. Keith, R. Kobayashi, J. Normand, K. Raghavachari, A. P. Rendell, J. C. Burant, S. S. Iyengar, J. Tomasi, M. Cossi, J. M. Millam, M. Klene, C. Adamo, R. Cammi, J. W. Ochterski, R. L. Martin, K. Morokuma, O. Farkas, J. B. Foresman, and D. J. Fox, Gaussian, Inc., Wallingford CT, 2016.

(16) A. D. Becke, Density-functional Thermochemistry. III. The Role of Exact Exchange. *J. Chem. Phys.,* 1993, **9**, 5648–5652.

(17) P. J. Stephens, F. J. Devlin, C. F. Chabalowski, M. J. Frisch, Ab Initio Calculation of Vibrational Absorption and Circular Dichroism Spectra Using Density Functional Force Fields. *J. Phys. Chem.,* 1994, **98**, 11623–11627.

(18) S. Grimme, Semiempirical GGA-Type Density Functional Constructed with a Long-Range Dispersion Correction. *J. Comput. Chem.,* 2006, **27**, 1787–1799.

(19) D. Hasa, D. Voinovich, B. Perissutti, M. Grassi, A. Bonifacio, V. Sergo, C. Cepek, M. R. Chierotti, R. Gobetto, S. Dall'Acqua, S. Invernizzi, Enhanced Oral Bioavailability of Vinpocetine through Mechanochemical Salt Formation: Physico-Chemical Characterization and in Vivo Studies. *Pharm. Res.,* 2011, **28**, 1870–1883.

(20) D. D. Sun, T. R. Ju, P. I. Lee, Enhanced Kinetic Solubility Profiles of Indomethacin Amorphous Solid Dispersions in Poly(2-Hydroxyethyl Methacrylate) Hydrogels. *Eur. J. Pharm. Biopharm.,* 2012, **81**, 149–158.

(21) B. van Eerdenbrugh, D. E. Alonzo, L. S. Taylor, Influence of Particle Size on the Ultraviolet Spectrum of Particulate-Containing Solutions: Implications for In-Situ Concentration Monitoring Using UV/Vis Fiber-Optic Probes. *Pharm. Res.,* 2011, **28**, 1643–1652.

(22) F. Fischer, M. Joester, K. Rademann and F. Emmerling, *Chem. Eur. J.*, 2015, **21**, 14969–14974.

(23) D. J. Berry, C. C. Seaton, W. Clegg, R. W. Harrington, S. J. Coles, P. N. Horton, M. B. Hursthouse, R. Storey, W. Jones, T. Friščić and N. Blagden, *Cryst. Growth Des.*, 2008, **8**, 1697–1712.

(24) S. Karki, L. Fabian, T. Friščić, P. R. Laity, G. M. Day, W. Jones, L. Fabian, P. R. Laity, G. M. Day and W. Jones, *Adv. Mater.*, 2009, **21**, 3905–3909.

(25) N. Schultheiss, M. Roe and S. X. M. Boerrigter, *CrystEngComm*, 2011, **13**, 611–619.

(26) T.M. Sabine, G.W.Cox, B.M. Craven, *Acta Crystallogr. B,* 1969, **25**, 2437.